Czech Technical University in Prague

Faculty of Electrical Engineering
Department of Electromagnetic Field

SCATTERER ARRAYS FOR CHIPLESS RFID

Doctoral Thesis

Ing. Jaroslav Havlíček

Prague, January 2020

Ph.D. Programme: P 2612 - Electrical Engineering and Information Technology
Branch of study: 2601V010 - Radioelectronics

Supervisor: doc. Ing. Milan Polívka, Ph.D.
Supervisor-Specialist: prof. Ing. Jan Macháč, DrSc

STATUTORY DECLARATION

I declare that I am the sole author of my thesis and have consistently cited the used literature. The parts of journal articles and selected conference papers (see the list of publications), which were created by a team of which I was a member, are used in the thesis. All co-authors contributed equally to the creation of all these published papers.

Prague, 31 January 2020

....
Author's signature

Content

ANNOTATION

Thesis is devoted to the chipless radio-frequency identification (RFID). The goal of this branch is to help RFID with finding new applications by decreasing manufacturing cost of RFID transponders (tags), which is achieved by avoiding the usage of a semiconductor chip.

The aim of the thesis is to investigate various electromagnetics planar structures, which can be employed for chipless RFID tags with improved performance parameters. Desired qualities are high spatial bit capacity of transponders operating both in frequency and time domain (number of coding bits of the transponder per its square size), high spectral bit capacity (in case of transponders working in frequency domain) and high radar cross section (*RCS*) response allowing high reading range of a transponder. Other important qualities of a transponder are reliability of tag reading and a platform tolerance (an independence of its electromagnetic properties from a material of a tagged object).

The first approach towards research of chipless RFID transponders working in frequency domain with enhanced properties was to investigate performance parameters of various planar scatterers, which are basic building parts of majority of these chipless RFID transponders. The S-loaded dipole was recognized as the most suitable scatterer for subsequent research because of its efficient trade-off between strength of its *RCS* response and both spectral and spatial bit capacity.

When a new transponder consisting of a suitable type of scatterer is examined, a need for an improvement of reading reliability via reducing mutual coupling between scatterers in a transponder usually emerges. This was achieved by rearranging the scatterers in the transponder and via slight changes in their topology. Both methods can be used together in one design.

The thesis is also focused on one type of time domain transponder. Already published near field chipless RFID system with sequential bit reading was enhanced by substituting split ring resonators for half wavelength dipoles and an open shunt $\lambda/4$ stub as a reader. Per-unit-length data density was significantly increased.

The last goal of the thesis was to investigate feasibility of structures consisting of a scatterer array closely coupled to a metallic plate for a chipless RFID transponder with electrically invariable parameters when it is attached to dielectric or metallic objects. Two different concepts of 20-bit transponders with high *RCS* responses are presented.

Key words: Chipless radiofrequency identification, coding capacity, platform tolerant transponder, quality factor, radar cross section, scatterer array.

ANOTACE

Disertační práce se zabývá bezčipovou rádiovou identifikací (RFID), oborem jehož cílem je umožnit technologii RFID nalézt nová uplatnění prostřednictvím snížení výrobních nákladů RFID štítků (tagů), které fungují bez polovodičových čipů.

Cílem práce je prozkoumat různé inovativní elektromagnetické planární struktury, které lze použít pro návrh bezčipových RFID štítků dosahujících lepších parametrů, než stávající návrhy. Požadovanými kvalitami jsou vysoká kapacita uložené informace na plochu štítku a to jak u štítků pracujících ve frekvenční tak i časové oblasti, vysoká spektrální kapacita uložené informace (pouze u štítků pro frekvenční oblast) a velká efektivní odrazná plocha (*RCS*), která je úměrná čtecímu dosahu. Dále je důležité, aby byla bitová informace spolehlivě čitelná, a aby byly elektromagnetické vlastnosti štítku nezávislé na materiálu předmětu, na kterém je umístěn.

Prvním krokem ve výzkumu zaměřeném na zlepšení vlastností bezčipových RFID štítků pracujících ve frekvenční oblasti bylo vyšetření různých planárních odražečů, které jsou zpravidla jejich základními stavebními prvky. Jako nejvhodnější odražeč pro další výzkum byl zvolen dipól se zakončením ve tvaru spirály díky jeho velké *RCS* odezvě, které dosahuje při zachování vysoké bitové kapacity, a to jak spektrální, tak plošné.

Při zkoumání vlastností nového štítku složeného z vhodných odražečů se často ukazuje, že je nutné zlepšit spolehlivost jeho čtení prostřednictvím minimalizace vzájemných vazeb mezi jednotlivými odražeči. Toho lze docílit např. přeuspořádáním jednotlivých odražečů ve štítku, úpravou geometrie odražeče popř. mohou být obě metody použity najednou.

Práce je rovněž zaměřena na jeden typ štítku pracujícího v časové oblasti. Stávající bezčipový RFID systém založený na principu sekvenčního čtení bitů v blízké zóně čtečky byl navržen s využitím rezonátorů typu přerušený prstenec. Výrazného navýšení datové hustoty na jednotku délky štítku tohoto systému bylo dosaženo uplatněním půlvlnných dipólů v návrhu štítku a mikropáskovým vedením s $\lambda/4$ pahýlem tvořícím čtečku.

Posledním cílem práce bylo zkoumání využitelnosti struktur zahrnujících odražeče v kombinaci s kovovou deskou pro návrh bezčipového štítku s elektricky neměnnými parametry při umístění na dielektrické či kovové objekty. Jsou představeny dvě různé koncepce dvacetibitových štítků s velkou *RCS* odezvou.

Klíčová slova: Bezčipová rádiová identifikace, činitel jakosti, kódovací kapacita, radarový průřez, řada odražečů, transpondér pro libovolné materiály.

INTRODUCTION

The radiofrequency identification (RFID) is a technology, which is used in general for automatic contactless identification of arbitrary objects, animals and people [1]. It is applied mainly in the industry (production process monitoring), logistics (acceleration of storing procedures), commerce (antitheft protection), health care (protection against confusion between patients), inventorying (e.g. books in libraries) and public sport events with mass attendance (e.g. half marathon) for competitor identification. Despite the fact that RFID is already widespread its novel applications are still emerging. RFID is expected to play an important role in the Internet of Things (IoT) concept [2]. Some RFID transponders can be also designed as simple and low cost sensors of physical parameters such as temperature, humidity, deformation, concentration of various gases and others [3, 4]. Another opportunity for its further spreading is in partial replacement of the optical barcode by the RFID transponders (tags) [5, 6]. The significant advantage of the tags compared to optical barcodes consists in the possibility to be read without the necessity of a clear line of sight, which is essential for reaching a higher level of automation.

The major obstacle to further RFID proliferation is the price of conventional tags comprising semiconductor chips, which are not cheap enough for applications that require a high number of these tags. In fact, conventional tags are approximately hundred times more expensive than optical barcodes [7].

Promising solutions for the tag cost reduction are represented by the chipless RFID concept [8], which includes different methods of storing identification information without any semiconductor chip being used. The most auspicious methods are those, whose layouts allow the tag production by printing, using a suitable conductive ink (Fig. 1.1). These printable tags can be potentially comparable to optical barcodes from the tag price point of view. Some cheap printing technologies have been already presented [9]. Another important advantage of chipless tags over the conventional ones is represented by a significantly lower minimum required input power [10]. For example, an interrogating signal of a SAW chipless tag can be ca. 100 times smaller than in the case of integrated circuit-based tags [11]. This feature provides a longer reading range of the chipless tags in general.

At first, the thesis presents state-of-the-art of chipless RFID tag design and summarizes unsolved challenges and visions in the field and then aims, used methods and results are described and presented.

The aim of the thesis is to investigate various electromagnetics planar structures, which can be employed for chipless RFID tags with better performance parameters. Desired parameters are high spatial bit capacity of transponders working both in

frequency and time domain (number of coding bits of the transponder per its square size), high spectral bit capacity (in case of transponders working in frequency domain) and high radar cross section (*RCS*) response allowing large reading range of a transponder. Another important parameter of a transponder is the independence of its electromagnetic properties on the material of a tagged object.

The first step in the research of chipless RFID transponders operating in the frequency domain with enhanced properties was to investigate performance parameters of various planar scatterers. Each of them can be used for storing one bit of identification information via its resonance which can be detected in spectrum of interrogational signal reflected from the transponder and received by the reader. Spiral loaded (S-loaded) dipole was recognized as the most suitable scatterer for subsequent research because of its efficient trade-off between strength of its *RCS* response and both spectral and spatial bit capacity.

The next step was to examine robustness and recognisability of tag RCS response when zero bits are encoded by removing appropriate scatterers. Scatterers, which are of the same type differing only in their length, placed too close to each other are distinguished by a strong mutual coupling between them. This property can result in both resonant frequency and *RCS* level shifts of neighboring scatterers especially when some of them are removed to encode zero bits. The mutual coupling therefore needs to be reduced in order to ensure reliable reading of stored identity information. This can be achieved by two techniques. Scatterer topology can be slightly changed and in this case, there is a trade-off between mutual coupling reduction and deteriorated scatterers parameters. The second option is to find an arrangement of scatterers in the transponder, which minimizes its overall mutual coupling. Both methods were investigated and their combination was used to introduce a 20-bit transponder composed of spiral loaded (S-loaded) dipole.

The thesis is also focused on a special type of time domain transponder. Already published near field chipless RFID system with sequential bit reading was enhanced by substituting split ring resonators for half wavelength dipoles and an open shunt stub. This amelioration enabled a design of 100-bit tag with per-unit-length data density increased froM3 bit/cm to 16.7 bit/cm.

The last goal of the thesis was to investigate properties of structures consisting of scatterers and a metallic plate from chipless RFID point of view. Two different concepts of 20-bit transponders with high *RCS* response are presented. The first concept is based on substitution of traditional planar scatterers for U-shaped slots, which are directly placed in the reflective plate. This solution has a potential of cheap manufacturing process because of its single layer layout but suffers a low dynamic range between *RCS* of logical zero and one. The second concept employs half wavelength dipoles as

scatterers, which are placed closely over the metallic plate. This solution is characterized by both high *RCS* response and encoding bit capacity, platform tolerance of electrical parameters when attached to various dielectric objects and stability of *RCS* response for reliable reading when individual scatterers are removed to encode logical zeros.

1 STATE OF THE ART IN CHIPLESS RFID TECHNOLOGY

The methods for chipless RFID tags can be divided into two main groups (Fig. 1.1), i.e. the tags based on the time domain detection on one hand and tags based on frequency domain detection on the other. These two main groups are briefly described in subsections 1.1 and 1.2. respectively and examples of chipless solutions are presented. Special attention is paid to the LC resonator group because it provides a large number of promising designs.
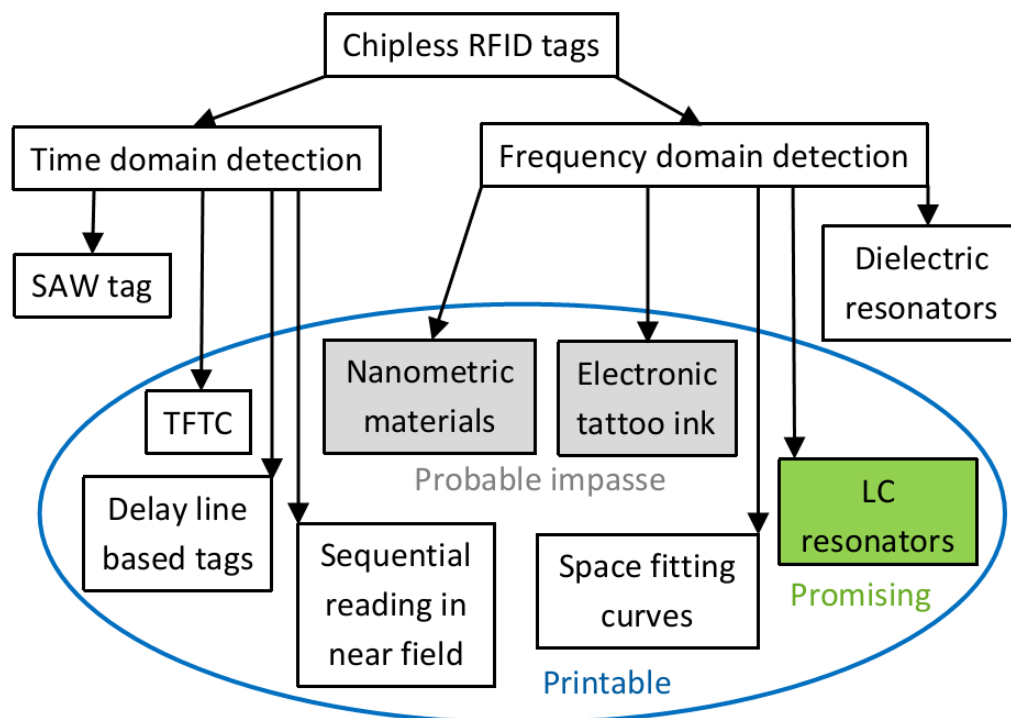

Fig. 1.1: Overview of the methods for chipless RFID.

1.1 TAGS WITH TIME DOMAIN DETECTION

The operational principle of the tags based on the time domain detection is similar to the conventional chip tag principle. The tag reader transmits a short pulse to the interrogated tag which responds back to the reader. The identification information of the tag is received as a set of pulses with different time spacing between them. Representatives of such kind of tag are SAW (Surface Acoustic Wave) [11], TFTC (Thin Film Transistor Circuit) [12], tags which incorporate delay lines and tags with sequential bit reading in near field of the reader [13].

A SAW tag consists of an antenna and a piezoelectric substrate with an interdigital transducer (IDT) and few reflectors; see Fig. 1.2 [14]. The incident electromagnetic wave is received by the antenna and then it is converted into an acoustic wave, which spreads along the substrate. Each reflector produces a response pulse when acoustic wave reaches it. Series of pulses is converted by IDT and antenna back to an electromagnetic wave which is received by the reader. Identification information is determined by a number of pulses (reflectors) and by spacing between them. SAW tags are commercially available by RFSAW Inc. company [7]. Their most important advantages are along reading distance (10 m), small size, high bit capacity (up to 256 bits) and very high operating temperature range. Disadvantage is a high price of the SAW tag which isn't comparable with an optical barcode although it is cheaper than a conventional chip tag. The SAW tags can't be manufactured by printing.
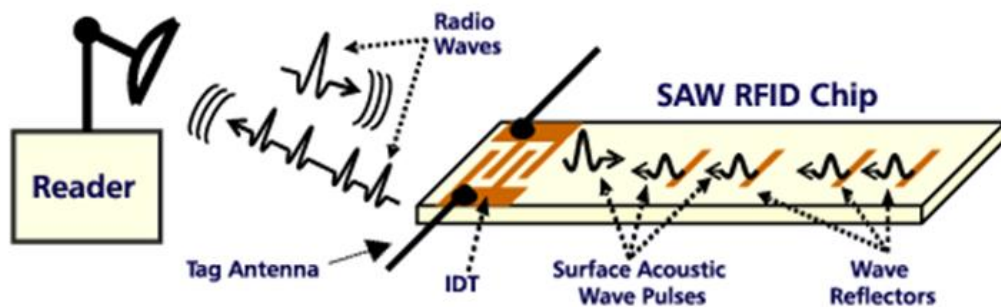

Fig. 1.2: Structure of SAW tag [14].

The TFTC (Thin Film Transistor Circuit) technology represents a novel concept of electronics manufacturing. Instead of expensive conventional semiconductor production processes (such as deposition, lithography, etching etc.), TFTC device is manufactured only by printing which is cheaper, faster and more environmental. All required materials such as silver nanoparticles, organic semiconductors and insulating polymers must be converted into inks [12]. TFTC layout can be printed on a flexible plastic film which is suitable solution especially for displays and wearable electronics (sensors etc.). TFTC's potential advantages from RFID point of view consist in a possibility to change stored identification information of a tag due to rewritable memory and compatibility with conventional RFID readers, which are already in usage. Design of a TFTC chip suitable for RFID purposes has been already published [15]. A Norwegian company called Thin Film Electronics ASA offers NFC compatible devices, dual-threshold temperature sensors and EAS tags for clothes [16]. Their most important know how consists in a printed rewritable nonvolatile memory design and production.

The last category of the tags which are based on time domain detection are tags using delay line. Basic principle is the same as principle of the SAW tags. But response

11

pulses are generated by impedance discontinuities in microstrip delay waveguide instead of reflectors in piezoelectric substrate. These tags can be fully printed which provides them low cost but also suffer from an insufficient bit capacity (less than 10 bits [6]). This bit capacity limitation cannot be overcome because of nature of the tag design. However, tags with delay line can be used as simple sensors [17].

There is also a tag design using delay line which function is different from SAW tag [18]. The tag consists of C-sections with different lengths, which are connected together (see Fig. 1.3) and two antennas. This dispersive structure causes that delay of each pulse depends on its frequency. This feature is employed for identification information storing using pulse-position modulation. The tag is interrogated by a series of short equidistant pulses (few ns) each has a different frequency and represents one bit. Some of these pulses are delayed while passing through the tag and others not depending on their frequency and the C-sections length. Binary values 0 and 1 correspond to logical levels 'delayed' and 'non-delayed' respectively. Maximal bit capacity of the tag is limited by maximal allowed duration of interrogating process and by maximal allowed bandwidth of used spectrum. C-sections can be used as a sensor [19]. There is a size reduction method for C-sections [20].

Fig. 1.3: Connected C-sections with different lengths [18].

Another group of chipless RFID systems operating in time domain are the systems based on sequential bit reading in near field of the reader; see Fig. 1.4. The reader consists of a transmission line with a coupled resonator, which works either as band-stop or band-pass filter, which depends on particular system. The tag consists of a linear chain of identical equidistant resonators, which are the same as the resonator coupled to the line of the reader. The reader line is fed by a harmonic signal at f_c and the transmission coefficient of the line at f_c is significantly changing in dependence on a tag resonator position above the reader. A zero bit is coded by detuning corresponding resonator. Amplitude-modulated (AM) signal generated by tag motion is decoded by the envelope detector in order to obtain an ID code of the tag. The main advantage of this

type of chipless RFID system is high data storage capability, which require negligible amount of spectrum. Detailed description of such system can be found in chapter 5, where a new version of the system with significantly higher bit capacity is proposed.

Several variants of this system were published, first of them employed a broadside-coupled split ring resonator coupled to CPW line [21]. This variant can also operate as velocity and an angular displacement sensor [22]. Another variant employed S-shaped split ring resonator likewise coupled to CPW line [23], which can be also used as a velocity sensor [24]. Bit capacity of the tag was increased by double chain arrangement [25]. The last version employed split ring resonator coupled to microstrip line [13] and it is suitable for secure paper applications. The system is able to operate on low-cost materials such as plastic (PEN) [26] and paper [27]. A method, which enables erasing and rewriting bit information of the tag, was proposed in [28]. Similar time domain near field system utilities a dielectric tag without any metal layer [29]. Changes of transmission coefficient are caused by changes in effective dielectric constant of the tag while it moves above the active part of the reader.
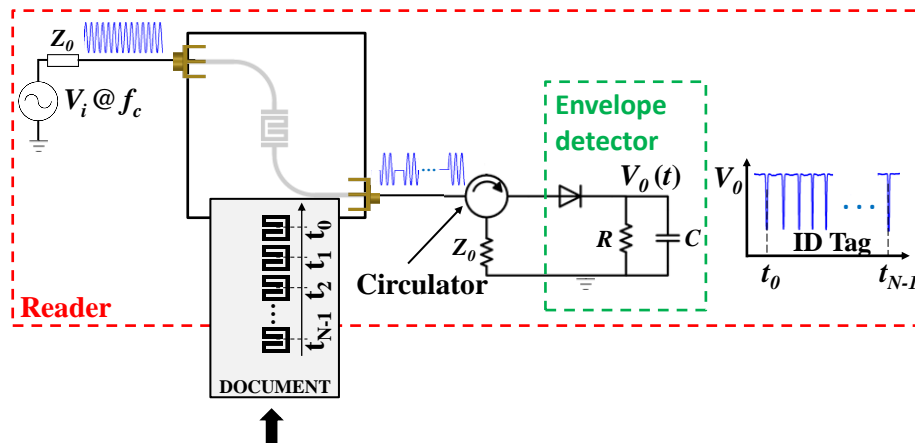

Fig. 1.4: Time domain chipless system with sequential bit reading in near field of the reader [13].

1.2 TAGS WITH FREQUENCY DOMAIN DETECTION

Chipless tags based on the frequency domain detection, involving a number of planar resonators in most cases, represent promising examples of chipless RFID technology. The basic idea of frequency domain information coding consists in the fact that every metal object has different frequency dependent radar cross-section *RCS* (called spectral signature) which is determined by its structure. The tag's spectral signature typically consists of series of resonance peaks. Modifications of the tag e.g. adding or removing a resonator result in presence or absence of the resonator's peak

which can be used to encode logical one or zero, respectively; see Fig. 1.5a (e.g. [30, 31]). Bit information can be also encoded by a frequency shift; see Fig. 1.5b [32-34]. There are also designs, which employ amplitude level of a resonant peak for information encoding in addition to simple presence/absence encoding in order to increase bit capacity of the tag [35-37]. Both amplitude and frequency shift coding can be utilized together [38]. The low bit capacity of the tags represents the key issue to be resolved. Representatives of this group are approaches using nanometric materials [39], electric tattoo ink [40], space fitting curves [41] and various types of dielectric resonators [42] or planar LC resonators.
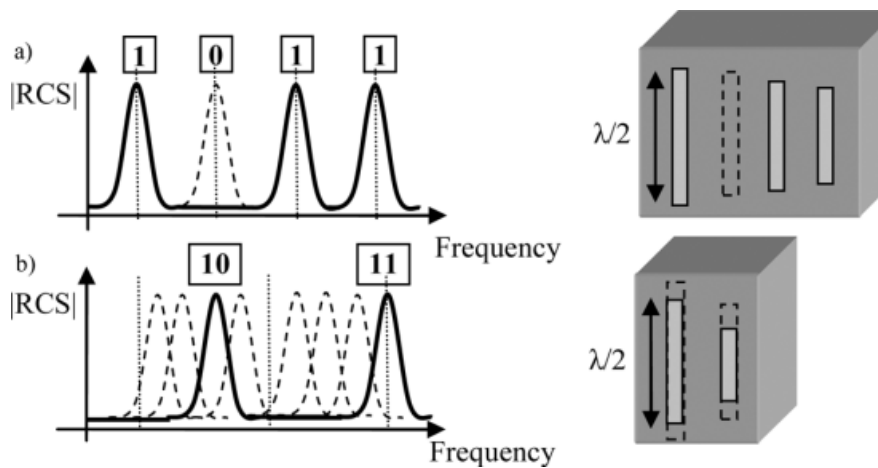

Fig. 1.5: Absence/presence coding technique. (b) Frequency shift coding technique [34].

The idea of ink with different magnetic properties caused by adding nanometric particles for shaping spectral signature was proposed in 2004 by CrossID company. The electronic tattoo ink (applied mainly for animal tagging) was about to be developed in 2009 by Somark company. The development of both of these approaches seems to be suspended since CrossID ceased to exist and Somark specializes merely in the field of marking laboratory mice (only visual tattoo). Their product Digital Mouse® offers RFID tagging via conventional chip technology utilization [43].

Planar space fitting curves such as Peano (Fig. 1.6) [41] or Hilbert curve can be used for chipless RFID too. Their advantage is embodied in a high level of electric length reduction, which is beneficial for miniaturization. The disadvantage, however, lies in the necessity of complicated tag layout changes for coding different binary numbers. Dielectric resonators can be used to design a frequency domain chipless RFID tag as well. These tags are non-printable but they can operate even in terahertz wave spectrum [42] and they can be utilized as chipless sensors [44].
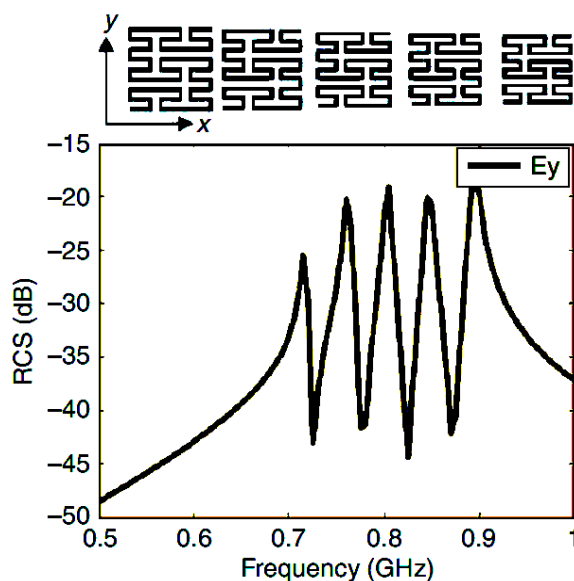
Fig. 1.6: Tag using Peano curve and its RCS characteristics [41].

The latter subgroup can be generally labeled as 'LC resonators' and it is considered to be the most promising, given the enormous variety of possible chipless RFID solutions. We can specify three principal performance parameters, which must be investigated for each LC resonator. The maximum *RCS* of the resonant peak that determines the reading range of the tag is the first of them. It can be seen that a higher *RCS* results in a longer reading range. The bandwidth (*BW*) of resonance peak depending on the quality factor *Q* of the resonance represents the second quantity. Its evaluation can be performed from frequency characteristics of the resonator as a frequency range of three-decibel resonance peak drop. This characteristic is very important from the spectral bit capacity point of view. The product *ka* is the last one from the above-mentioned quantities. The variable *k* is the wave number, while the variable *a* stands for the radius of circle that circumscribes the resonator. This product represents the rate of electric reduction of the resonator. Resonators with *ka* below one are more suitable candidates because small size is essential for application in chipless RFID. The tags based on LC resonators can be also used as simple low-cost sensors [45-47].
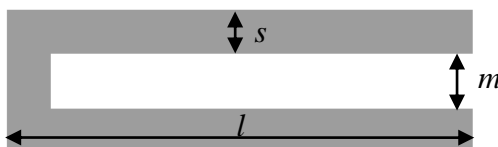

Fig. 1.7: U-folded dipole [31].

The simplest structure, which can be described as an LC resonator is half wavelength dipole. Two designs called RFID barcodes are based on them [30, 48].

15

These are simple solutions, which are easy to propose but they are not efficient from bit spectral capacity point of view. Latin alphabet letters can be also described as LC resonators and their properties from RFID point of view was investigated [49] although their practical usage possibilities are limited.

Significantly better results are achieved with different resonators. The U-folded dipole (Fig. 1.7) [31], which consists of two parallel arms connected together at the one end, is one of them. Width of all its lines is $s = 1$ mm and the distance between the arms is $m = 0.5$ mm. The required resonance frequency of the scatterer is given by the length of its arms, which is similar to a quarter of a resonant wavelength. The quality factor is given by length to distance between the arms ratio ($Q = l/m$). The distance between arms is in direct proportion to resonance bandwidth [34]. The tag [31] is composed of twenty U-folded dipoles, which are arranged parallelly in the arm length ascending order (the arm length increases by 0.5 mm from $l = 16$ mm to $l = 25.5$ mm). There is 1 mm spacing between the dipoles in the tag. Frequency domain information encoding can be realized either by changes in *RCS* resonant peaks of frequency characteristic (caused by shorting particular U-folded dipoles) or by changes in the group velocity (first derivation of the phase with respect to frequency).
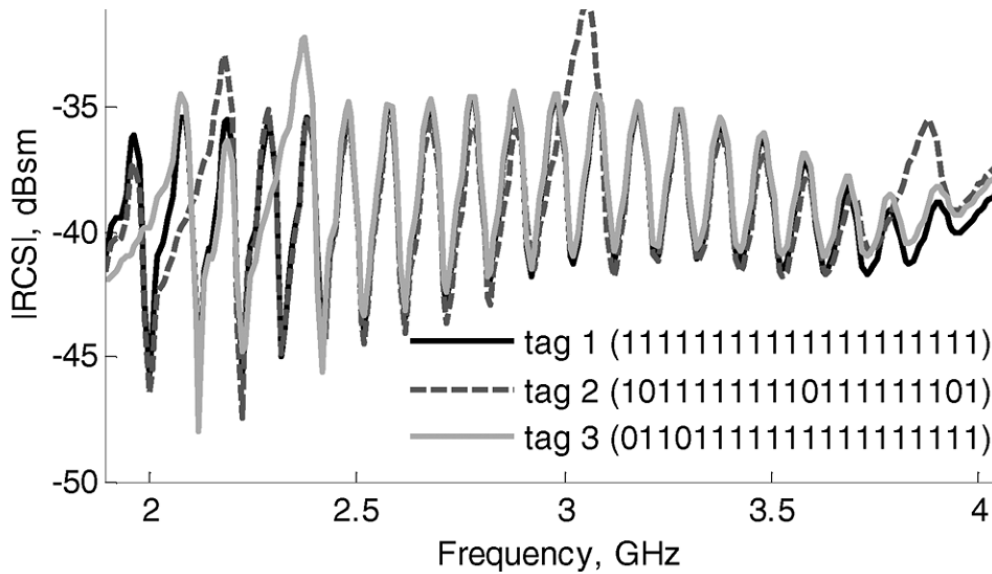

Fig. 1.8: Simulated *RCS* responses of 20-bit tag using U-folded dipoles [31].

Relatively high area bit capacity (20 bits on an area of 7×2.5 cm^2) and the fact that the tag is fully printable are its most important advantages. A method for compensation of frequency shifts caused by permittivity differences of tagged items was also published [31]. Disadvantage of the tag consists in disproportion of resonant peaks caused by mutual coupling between the neighboring U-folded dipoles (Fig. 1.8). This disproportion can cause information decoding impossible. The mutual coupling can be

reduced either by rearranging U-folded dipoles of the tag or by slightly changed layout of the U-folded dipole. Both these methods are described in detail in subsection 4.1 and 4.2 respectively. The topology of the U-folded dipole was also used as a basic element for the three-bit compact multi-resonant tag [50].

The U-folded dipole's electrical size can be lowered in order to improve its rate of electric reduction by adding a load, which is either a meander line inductor or an interdigital capacitor [51]. Capacitive load achieved 31 % reduction while inductive load 21 % of the length of the original U-folded dipole but there is a trade-off between scatterer *RCS* of the resonance peak and the level of reduction. *RCS* decrease is greater in the capacitive load case because the interdigital capacitor at the ends of the arms shorts the U-folded dipole.

For a significant increase of *RCS* response complementary structures can be employed [52]. A tag consists of 20 U-folded dipole slots in metallic plate has circa 20 dBsm higher *RCS* response than the original transponder [31]. Disadvantage of the slot tag is a strong detuning effect of the missing or shorted slots representing logical zero on the resonances of neighboring slots signifying logical one. Modification of the inter-element arrangement reduces this problem. Differences between *RCS* resonant maximums and minimums are low (circa 1 dBsm in the worst cases) which can be a difficulty for a tag reader. However, the concept of employing a metal plate design is generally quite promising in chipless RFID.
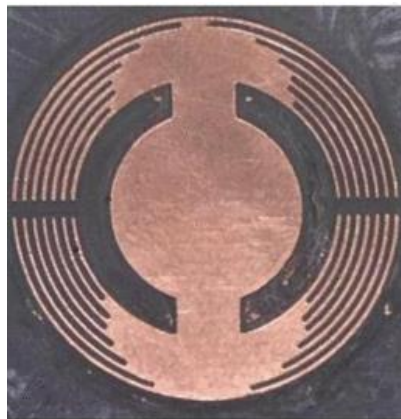

Fig. 1.9: Tag based on complex natural resonances [53].

Different type of a slot (λ/4 resonators) is used in the tag based on complex natural resonances [53] (Fig. 1.9) which allows information encoding in more advanced manner than simple resonant frequencies. The complex natural resonances which depend only on geometry of the scatterer can be recognized by short-time matrix pencil method (fully described in [54, 55]) from late-time response of the tag. Reader of this type of tag receives tag's response in frequency domain. Then the response is transformed into time domain using inverse fast Fourier transform. Finally short-time matrix pencil

method is applied on a late-time part of the response. The advantage of this tag is very high areal density of stored information (24 bits on 24 x 24 mm^2 area). Weak points of the tag are low spectral bit capacity (only 24 bits in 7 GHz bandwidth) and higher demands on reader due to additional signal processing. The characteristic mode theory can be employed to describe this type of tag [56].

Another chipless RFID design focused on high areal data density is presented in Fig. 1.10a [57]. The tag consists of concentric rectangles however at least four sets of them are needed because the tag is based on frequency selective surface (FSS) concept [58]. The advantage of this solution besides high spatial bit density is resistance to unwanted signal reflections from environment due to cross-polarization, which means that linear polarizations of received and transmitted waves of the tag are orthogonal to each other. There are other cross-polarized or polarization independent tags [59-65]. Rectangular loop can be tuned to required resonance frequency by stubs displayed in Fig. 1.10b [66, 67]. This tag can be also used for sensor design [68]. The concentric arrangement of specific resonators is an effective way to achieve a high spatial bit density [69, 70].

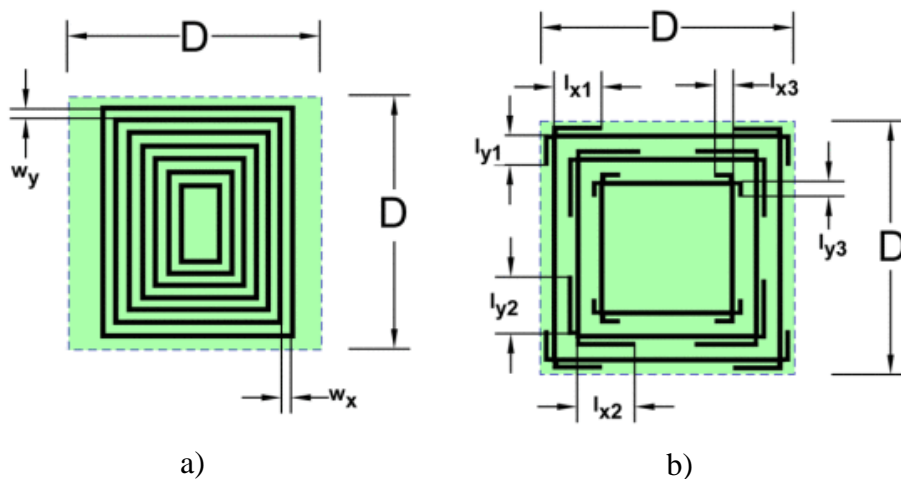a)   b)

Fig. 1.10: Tags consist of concentric rectangular loops used as FSS [57].

A planar spiral is another LC resonant structure, which can be used in chipless RFID [71]. The tag, which uses them, consists of two ultrawideband (UWB) disc-loaded monopole antennas, microstrip waveguide connected between them and set of spiral resonators, which are coupled by a gap to the microstrip waveguide (Fig. 1.11). Interrogating wideband signal is received by the vertically polarized monopole antenna and spreads along the microstrip waveguide. Coupled spiral resonators can be described as a cascade of filters, which significantly attenuates the signal at particular resonant frequencies of the spirals. Then the filtered signal with notches is transmitted by horizontally polarized monopole antenna back to an RFID reader. The receiving and transmitting antenna are cross-polarized in order to minimize interference between the

interrogation signal and the re-transmitted encoded signal containing the spectral signature of the tag. Zero bits are encoded either by removing a particular spiral or by shorting it. The requirement of a ground plane (represented by lighter gray in Fig. 1.11) makes this tag more difficult (and expensive) to manufacture, however such a tag can be at least semi-platform tolerant, similarly to designs proposed in [33, 69]. Utilization of a coplanar waveguide (CPW) instead of a microstrip line provides an advantage of single layer layout; see Fig. 1.12 where a spiral slot resonator is coupled to CPW [7]. Designs of both microstrip line and CPW variants of the tag were published together in [72]. There are more designs based on the idea of resonators coupled to a transmission line [32, 36, 65, 73, 74].
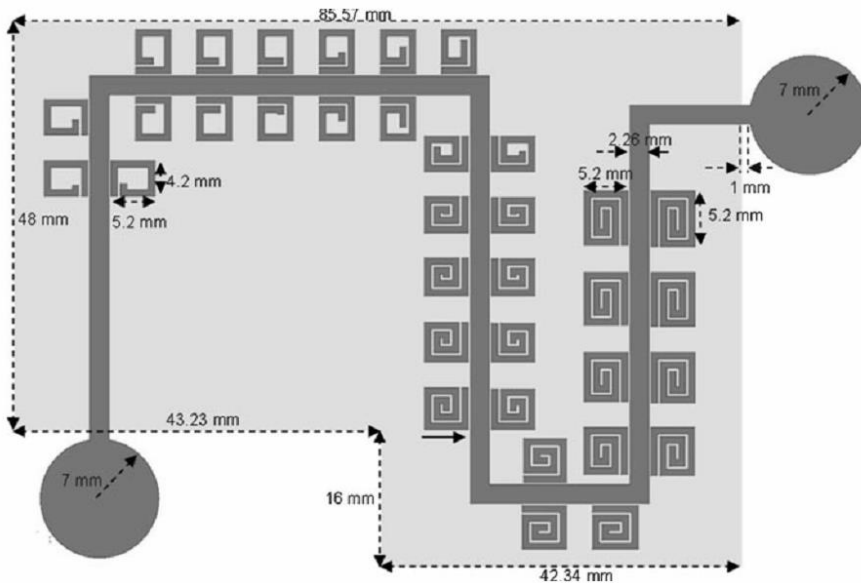

Fig. 1.11: Layout of tag with spirals coupled to microstrip waveguide [72].

Fig. 1.12: Spiral resonators coupled to coplanar waveguide [72].

1.3 SUMMARY

Based on the overview above, it is possible to specify challenges in the field of chipless RFID that are still not satisfactorily resolved. In the field of frequency domain tags, it is desirable to increase the spatial bit density of tags by using electrically smaller scatterers and also to increase their spectral efficiency. Another challenge is to improve frequency stability and amplitude uniformity of the resonant peaks in tag's *RCS*

response by reduction of mutual coupling between scatterers. The tags operating in time domain are spectrally undemanding but also need a spatial bit capacity enhancement and their tags also affected by resonators mutual coupling. Both time and frequency domain chipless tag designs should also provide further improved performance such as polarization independence, platform tolerance, smart detection techniques for reliable reading and anti-collision techniques. A new category of so-called spatial-based chipless RFID systems employing electromagnetic imaging can emerge in the future [75].

Some of the above features of a chipless tag are contradictory such as a high spatial bit density (electrically small size causing high quality factor of single scatterers) and large *RCS* response (large effective area) thus chipless RFID tag design will be a trade-off between them. The chipless tag can also be implemented with sensing capabilities and thus employed as wireless sensors.

2 AIMS OF THE DOCTORAL THESIS

There are many challenges in the chipless RFID field, which are mentioned in the summary of state-of-the-art; see chapter 1. The most important among them are spatial bit capacity of a transponder (in frequency domain also spectral bit capacity) and its high reading distance but these performance parameters are contradictory. Spatial bit capacity is usually achieved by employing an electrically small scatterer with high Q factor. Reading distance is corresponding to RCS response of a transponder. Five aims are specified to be addressed:

1) Enhancement of spectral and spatial capacity of tags using electrically small scatterers.

2) Strengthening reliability of reading by applying individual scatterer rearrangement techniques.

3) Predicting the influence of mutual coupling in a scatterer array on its parameter performance by equivalent circuit modeling.

4) Improving spatial bit capacity of the time domain tag applying a sequential bit reading technique.

5) Theoretical and numerical investigation of platform tolerance of tags with high overall RCS response using a dipole-array coupled to a metallic plate concept to better understanding the limitations of encoding bit density of the chosen structure.

3 PARAMETER COMPARISON OF SCATTERERS SUITABLE FOR THE DESIGN OF CHIPLESS RFID TRANSPONDERS

This chapter deals with the performance parameter comparison of investigated planar scatterers which are suitable for chipless RFID design and which can be described as LC resonators. Comparison is based on the three essential characteristics electrical size, bandwidth (actually proportional to electrical size, however not directly due to the different space filling), and reflection properties more deeply described in section 1.2 and presented in [76, 77].

3.1 TOPOLOGY OF INVESTIGATED SCATTERERS

Investigated strip-type scatterers etched on thin dielectric substrate RO4003 can be divided into two groups. The first group includes simple structures (e.g. dipole, loop) and more sophisticated scatterers presented by other authors (e.g. thick U-folded dipole); see Table 3.1. The second group of scatterers is represented by several capacitively loaded dipoles and one inductively loaded dipole (ILD) which are elaborated by the author and specified in more detail in the following text; see Table 3.2 and [76]. Topologies of all investigated scatterers are shown in Fig. 2.1 and 2.2.

Scatterer	Geometric dimensions
Dipole	length 37 mm, width 1 mm
Circular ring	diameter 10 mm, line width 1 mm, gap width 2.3 mm
Rectangular ring	side 10 mm, line width 1 mm, split length 2.5 mm
Meander dipole	total length 56 mm, meander length 6 mm, line width 1 mm, distance between meanders 1 mm
Thick U-dipole [31]	arm length 20.5 mm, line width 1 mm, distance between arms 0.5 mm
Thin U-dipole [77]	arm length 20.5 mm, line width 0.25 mm, distance between arms 2 mm
Tapered U-folded dipole [78]	arm length 20.5 mm, line width 0.25 mm, distance between skew arms at their open ends 0.5 mm
Meander U-dipole [51]	arm length 20.5 mm, line width 0.25 mm, meander length 5 mm, distance between meander arms 0.2 mm, distance between dipole arms 2 mm

Table 3.1: Topology and dimensions of investigated scatterers.

Each of capacitively or inductively loaded dipoles occupies a rectangle area ranging from 20.5 mm to 2.5 mm. ILD consists of 18 skew parts. The spacing between them and the arms is 0.23 mm in length, line width equals 0.25 mm and length of the straight part in the middle of the scatterer is equal to 2 mm. The basic capacitively loaded dipole (CLD 1) consists only of a dipole part and four loading arms of 9.25 mm in length each. The spacing between the dipole part and the arms equals 0.88 mm and the width of all lines accounts for 0.25 mm. The version labeled as CLD 2 is based on CLD 1, yet four inner arms were added (length of 8.75 mm, the spacing between dipole part and inner arms is 0.38 mm, the spacing between outer and inner arms is 0.26 mm).

The capacitively loaded dipoles can be divided into two groups. The difference lies in the mutual linking of ending arms, which can be either meander-shaped or spiral-shaped. We proposed three-arm versions labeled as 'M3 arm' (M, meander) and 'S3 arm' (S, spiral). The latter represents an extension of CLD 2 (arms width as well as spacing between them was reduced to 0.18 mm). Thin versions (M5 arm and S3 arm v2) have five and three arms respectively and their line width as well as spacing between arms equals 0.1 mm. Detailed topology of the 'S3 arm v2' scatterer is depicted in Fig. 3.1. This scatterer was used as a basic resonant element of tags described in subsections 4.1.1 and 4.1.2, where it is called dual-spiral loaded dipole scatterer (DSLD) [79]. The scatterer 'S3 arm v3' has only two spiral endings, thus its outer size is 20.5×1.3 mm^2 and it is called the spiral loaded (S-loaded) dipole in section 4.3 [80]. All scatterers were designed on Rogers RO4003 substrate ($\varepsilon_r = 3.38$, $\tan \delta = 0.002$, 0.2 mm in thickness).
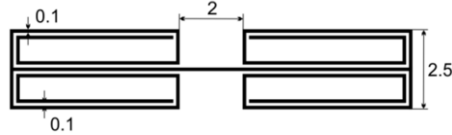

Fig. 3.1: Detailed topology of 'S3 arm v2' (DSLD) scatterer. All dimensions are in mm.

3.2 COMPARISON OF THE INDIVIDUAL SCATTERER PERFORMANCE PARAMETERS

In conformity with the theory of electrically small antennas, it can be stated that the resonance structures with small ka show high values of quality factor Q. This phenomenon results in a low frequency bandwidth on one hand (this is beneficial for high spectral bit capacity), yet in low RCS on the other, which is inappropriate for reading range. Therefore, the chipless RFID tag design consists always in searching for the balanced trade-off between the spectral bit capacity and the reading distance. The simulated performance parameters comparison of scatterers properties applying method of moment software Zeland IE3D is shown in Table 3.2. and Fig. 3.2 and Fig. 3.3 confirm these findings.

Scatterer	ka (-)	f_r (GHz)	RCS_{max} (dBsm)	BW_{3dB} (MHz)	BW (%)
Dipole	1.32	3.400	-22.2	636.0	18.7
Circular ring	0.51	4.893	-28.8	205.7	4.2
Rectangular ring	0.61	4.085	-27.0	158.8	3.9
Meander dipole	0.99	3.555	-23.0	375.6	10.6
Thick U-dipole	0.65	3.012	-36.8	17.2	0.6
Thin U-dipole	0.62	2.855	-35.0	18.2	0.6
Tapered U-folded dip.	0.55	2.565	-43.8	16.0	0.6
Meander U-dipole	0.57	2.623	-40.4	29.2	1.1
CLD 1	0.71	3.263	-23.4	120.2	3.7
CLD 2	0.59	2.723	-24.4	54.7	2.0
M3 arm	0.56	2.570	-26.8	48.1	1.9
ILD	0.61	2.830	-23.9	78.3	2.8
S3 arm	0.48	2.212	-28.0	28.1	1.3
M5 arm (thin)	0.47	2.152	-30.9	41.5	1.9
S3 arm v2 (thin)	0.35	1.609	-33.5	17.2	1.1
S3 arm v3 (thin)	0.36	1.683	-37.0	17.8	1.1

Table 3.2: Comparison of scatterer properties operating at their resonant frequency.

U-dipoles achieved the lowest frequency bandwidth, above all. The best of them is tapered U-dipole with bandwidth 16 MHz (0.6 %). However, their *RCS* response is below or equal to -35 dBsm, which leads to a shorter reading range. Their electrical sizes *ka* attain average levels within the range achieved by all investigated scatterers.

The capacitively loaded dipoles show, in general, higher *RCS* (up to -23.4 dBsm), however most of them are insufficient from the frequency bandwidth point of view. When comparing CLD 1, CLD 2 and M/S3 arm scatterers, it is noticeable that adding more arms to the scatterer endings results in the lower *ka* and lower *BW*, yet at the expense of *RCS* magnitude.
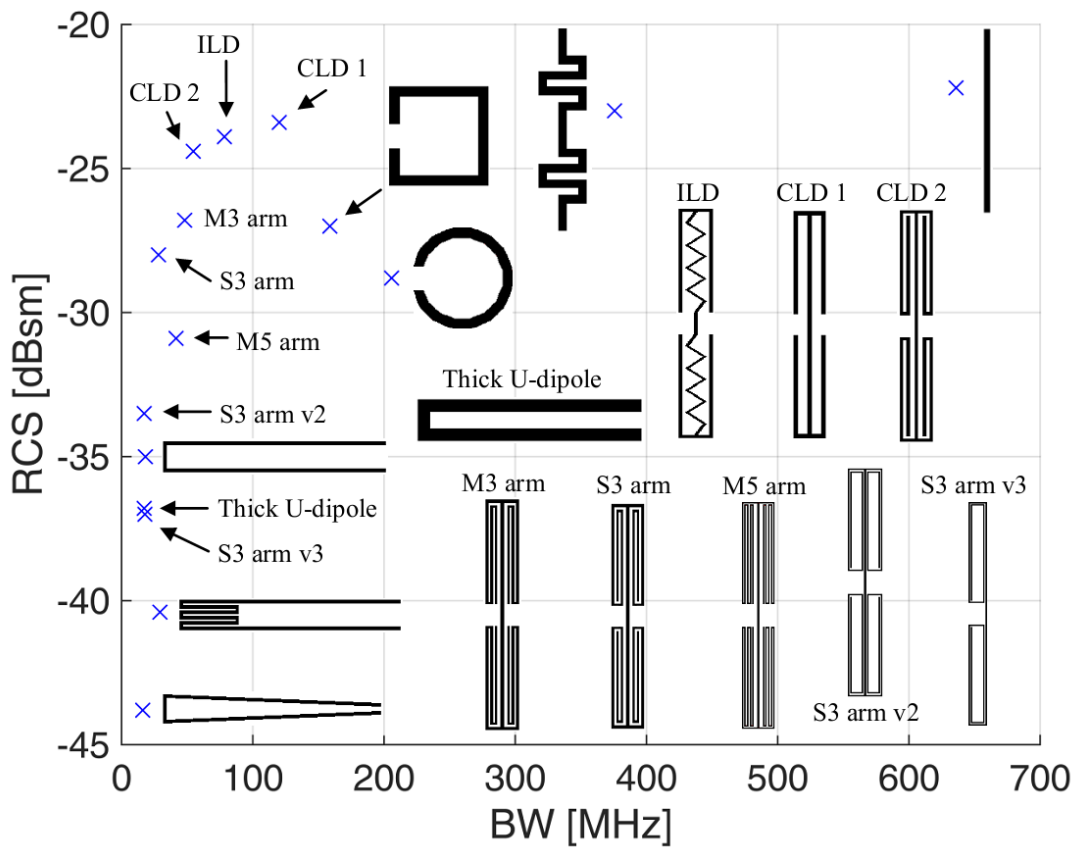
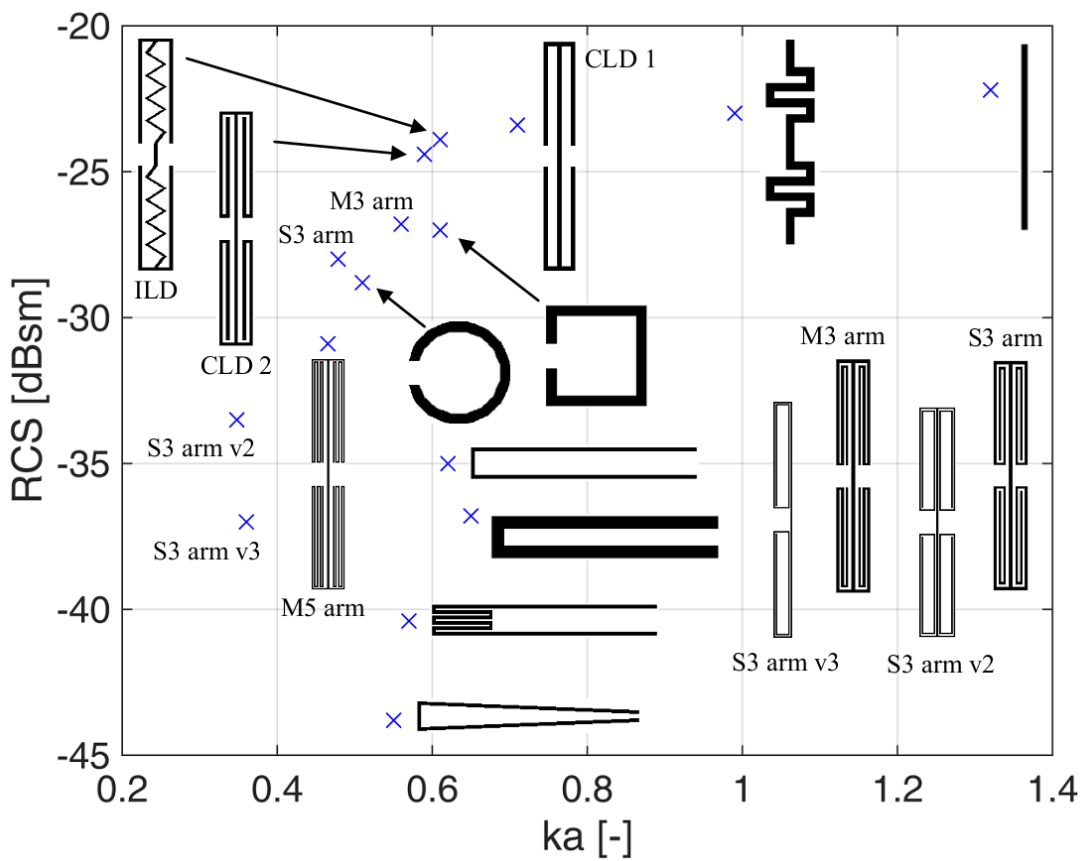Fig. 3.2: Comparison of scatterers according to *RCS* and resonance bandwidth.

Fig. 3.3: Comparison of scatterers according to *RCS* and electrical size *ka*.

The comparison of meander/spiral load arm approaches shows that the spiral scatterer has more suitable performance parameters from chipless RFID point of view. This phenomenon is attributable to the orientation of coincident currents in neighboring arms of the spiral, compared to the opposite currents in meander arms [81]. Thin variants of meander/spiral scatterers were designed in more than two versions proposed above, however their *RCS* was too low or the frequency bandwidth was too high hence, they turned out to be unsuitable for multi-bits chipless structures.

The S3 arm v2 dipole has the best trade-off between *RCS* and *ka* as well as between *RCS* and *BW.* Comparison between its resonant peak frequency characteristic and peaks of its development versions is in Fig. 3.4 This resonator is called dual-spiral loaded dipole scatterer (DSLD). The 20-bit tag, which is presented at the end of subsection 4.1.1 [79], suffered overly strong mutual coupling between neighboring scatterers which significantly impaired recognisability of the resonance peaks; see Fig. 4.9a. Mutual coupling can be reduced either by suitable rearrangement of the scatterers in the tag; see section 4.1, or by topology modification, which is represented by scatterer 'S3 arm v3'. This modification has slightly worse performance parameters (especially *RCS*) than the original scatterer but it can be utilized in a tag with suitable reading reliability; section 4.3 [80], where the 'S3 arm v3' is called the spiral loaded (S-loaded) dipole.
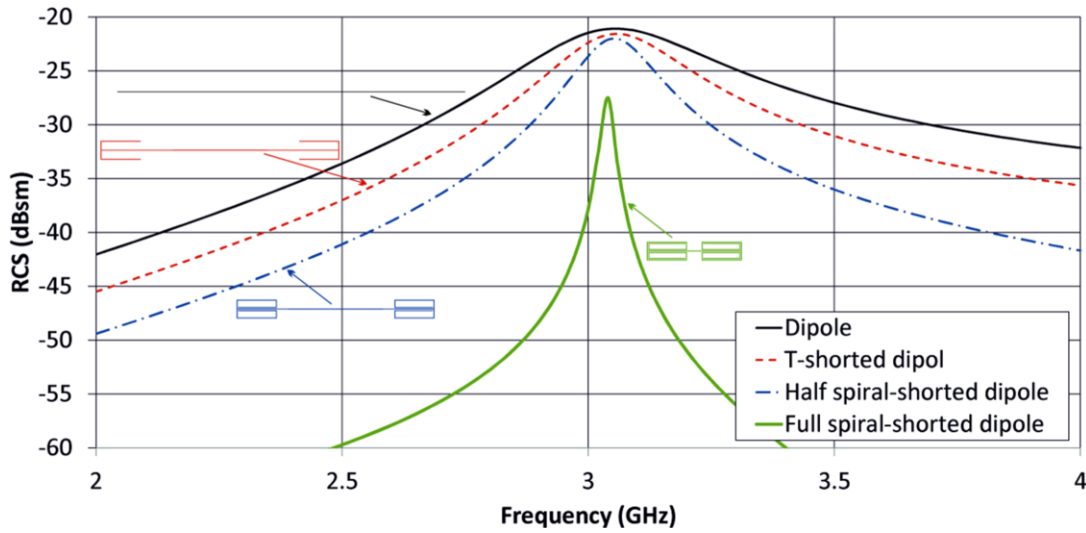

Fig. 3.4: Frequency dependence of RCS of DSLD compared to its development versions and simple straight dipole (in scale).

3.3 SUMMARY

The performance comparison of various types of planar scatterers for chipless RFID building elements [76, 77] shows that there is an expected trade-off between the electrical size and bandwidth on one side and the *RCS* level, representing reflection

properties, on the other. Furthermore, it was found that the arm loaded dipoles exhibit by up to 5-10 dB larger *RCS* level than U-folded dipoles of the same electrical size. Yet they provide typically a 2-3 times larger bandwidth. It implies a smaller spectral bit capacity. However, the best performance of the proposed loaded dipole S3 arm v2 (DSLD) (RCS = -33.5 dBsm, BW = 17.2 MHz, ka = 0.35) overcomes the reference U-folded dipole (RCS = -35.0 dBsm, BW = 18.2 MHz, ka = 0.62) of the same outer dimensions.

4 HIGH SPECTRAL AND SPATIAL CAPACITY TAGS WITH IMPROVED RELIABILITY OF READING

The strong mutual coupling between scatterers which has a negative effect on uniformity of the resonance peaks (which can be seen e.g. in Fig. 1.8) is a major obstacle to achieve a high spatial bit capacity tag. Two methods for reduction of this negative effect are presented in this chapter. The first one is based on the rearrangement of the resonant elements, which reduces the mutual coupling by maximizing the distance between those elements that are neighboring in terms of frequency. Two different rearrangements are proposed in this chapter, rearrangement based on sub-arrays and circular rearrangement; see subsection 4.1.1 [82, 83] and 4.1.2 [79] respectively. The other method applies the scatterer topology modification [78, 84, 85]. In fact, there is a trade-off between the reduction in mutual coupling and *RCS* response maximum. The mutual coupling reduction effect of both methods is demonstrated on the 20-bit tag which consists of U-folded dipoles (UD) proposed by [31] (see section 1.2). Both methods can be combined in order to maximize mutual coupling reduction which is presented in section 4.3 [80] on the example of the tag which is using a spiral loaded dipole as a basic resonant element.

4.1 THE TAGS EMPLOYING INDIVIDUAL SCATTERERS REARRANGEMENT FOCUSED ON MUTUAL COUPLING REDUCTION

4.1.1 TAGS BASED ON SUB-ARRAYS REARRANGEMENT OF THEIR SCATTERERS

This subsection proposes an approach to reduce the mutual coupling between particular resonators by rearrangement of the order of individual scatterers in the array, so that the resonators with neighboring resonant frequencies are placed further apart in a new array. The new tag response considerably increases the frequency and amplitude robustness of *RCS* response without the mean-value of *RCS* level being decreased. Thereby the reliability of reading the coded information is enhanced.

Fig. 4.1a depicts the layout of original and the proposed and further referenced 20-bit chipless tag, composed of an array of U-shaped strip scatterers representing a bit word '11111111111111111111'. The topology of basic array element is inspired by the one used in [31]. The outer size of the largest element is 25.5×2.5 mm^2, while the dimensions of the smallest one equal 16×2.5 mm^2, with the strip width of 1 mm and the gap size equal to 0.5 mm. Consequently, all *RCS* resonance peaks match the frequency range from 2 to 4 GHz. The distance between each two neighboring

elements, which are arranged according to the element length from the largest one to the shortest one in descending order, is 1 mm. The tag motif was etched on the low-loss dielectric substrate Rogers RO4003 ($\varepsilon_r = 3.38$, $\tan \delta = 0.002$) with the thickness of 0.2 mm. The incident excitation field is oriented parallel to the shortening strip stub placed at one end of each scatterer, i.e. horizontally to the tag presented in Fig. 4.1.
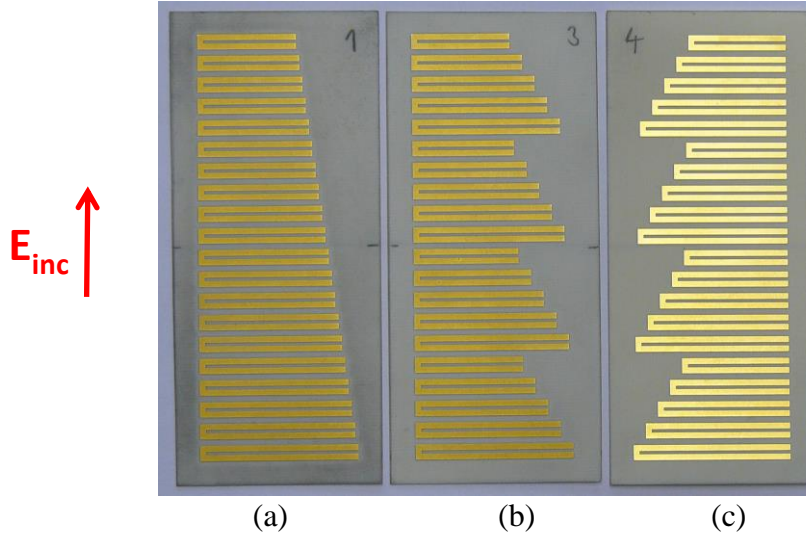

(a)   (b)   (c)

Fig. 4.1: Configurations of original and two modified layouts of 20-bit chipless tag, composed of array of the U-shaped strip scatterers representing a bit word '11111111111111111111'. a) Original alignment to short ends, and element rearranged configurations with alignment b) novel alignment to short end, and c) to the open end.

To reduce the mutual coupling between directly adjoining scatterers with neighboring resonance frequencies, we have proposed a modification of element arrangement. The scatterers are divided into four sub-arrays, where each element is next to the one that was originally in fourth position from it. Consequently, the original ascending order according to the element length '1 2 3 4 5 6 7 ... 20' is modified to '1 5 9 13 17, 2 6 10 14 18, 3 7 11 15 19, 4 8 12 16 20'; see Fig. 4.1b. In this layout, the resonators with neighboring resonance frequencies are then located further apart and their coupling is substantially reduced. The third array configuration varies from the second configuration by the alignment of scatterers to the open end (see Fig. 4.1c, which further increases the distance of shortening strip stubs of neighboring elements).

All three scatterer arrays (i.e. the reference and two with element-rearrangement) were tested for magnitude and frequency uniformity of *RCS* resonant peaks using several configurations of coding the bit word '11111011111111011111'. Firstly, scatterers in positions 6 and 15 (counted from the largest one) are missing. Secondly, in '11110011111111001111' the scatterers number 5, 6, 15, and 16 are missing. Thirdly, in case of '11111111110000000000', the scatterers number 11 to 20 are missing. As far

as the bit word '10101010101010101010' is concerned, every even scatterer is missing; see Fig. 4.2.

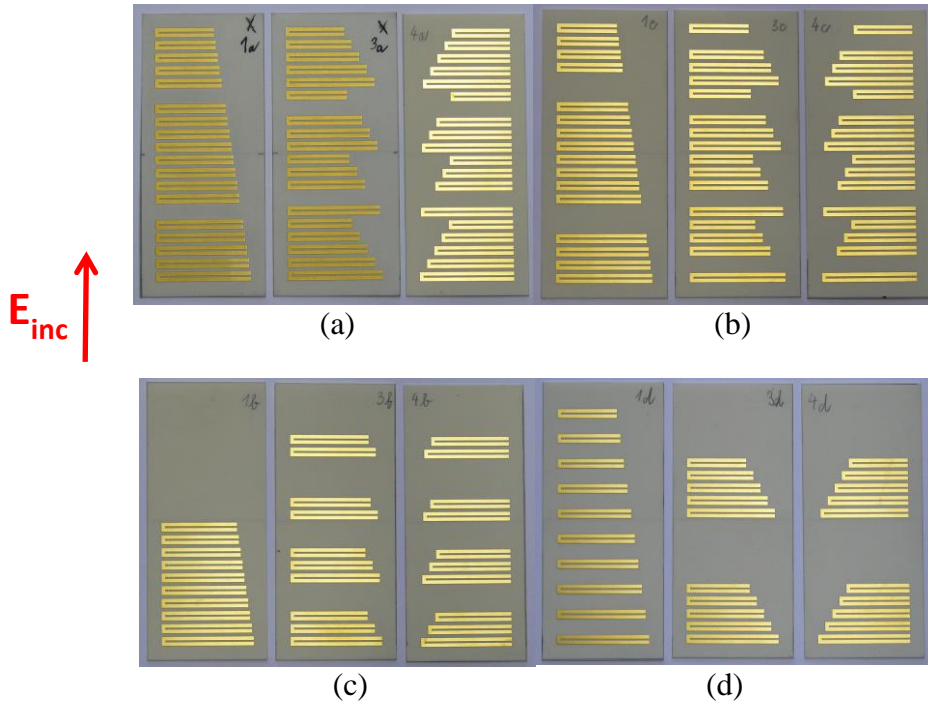(a)   (b)

(c)   (d)

Fig. 4.2: Layouts of 20-bit chipless tag composed of an array of the U-shaped strip scatterers representing bit words a) '11111011111111011111', b) '11110011111111001111', c) '11111111110000000000', and d) '10101010101010101010' in original arrangement with alignment to the short ends (left), and in element-rearranged configurations with alignment to the short end (middle), and to the open end (right). 0" bits are represented by absence of particular elements.

Chipless tags were simulated by MoM software Zeland IE3D, using the infinite dielectric layer implementation with 20 cells per wavelength with narrow edge cells in order to perform a precise modeling of current density distribution of in transversal cut of the strip. Each of the following Fig. 4.3 to Fig. 4.6 contains three plots corresponding to the tag configurations from Fig. 4.2a - d with the two *RCS* curves. The thin black line represents the reference 20-bit word '11111111111111111111' from Fig. 4.1, whereas thick red line symbolizes the bit word, where two or more '0' bits are coded according to configurations in Fig. 4.2a - d.
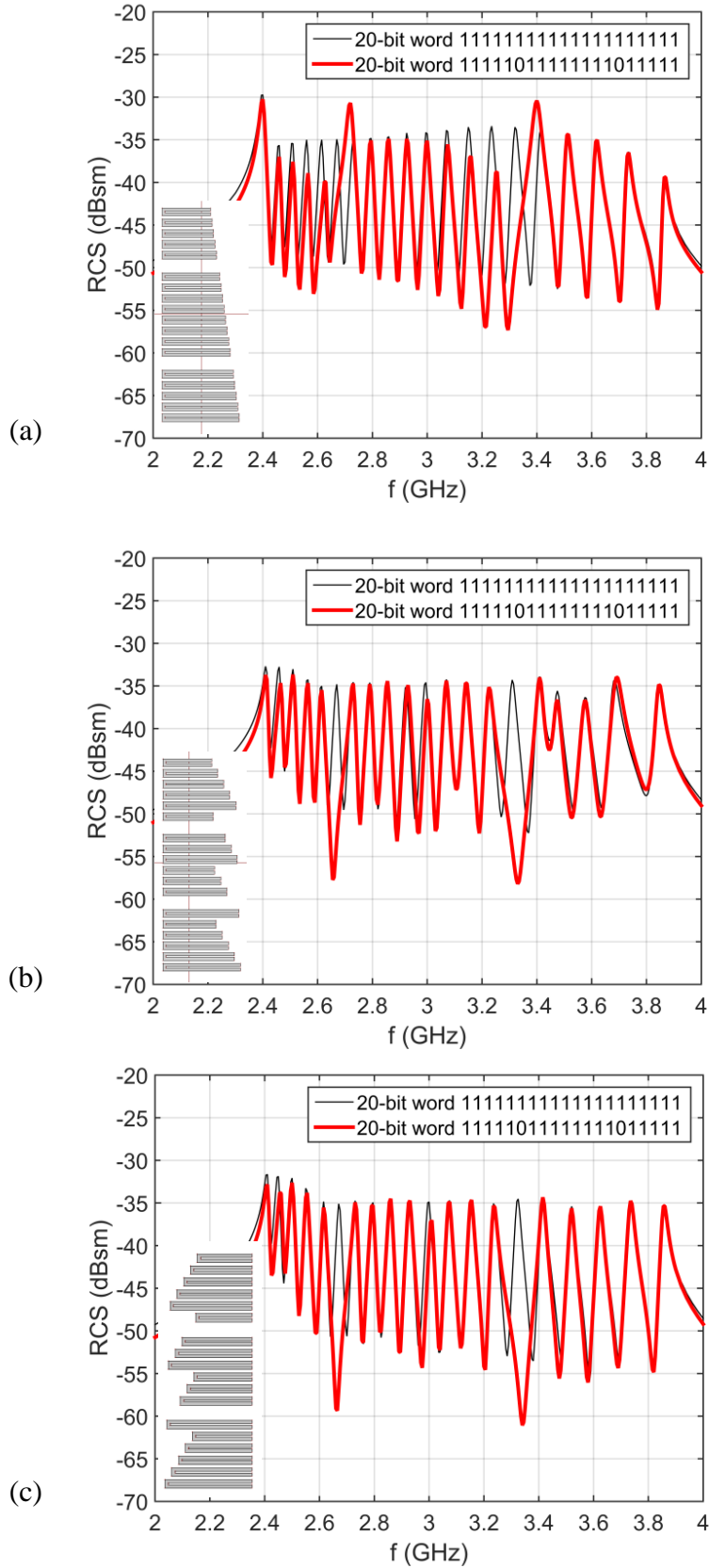
Fig. 4.3: Simulated *RCS* response of 20-bit chipless tag composed of an array of the U-shaped strip scatterers representing a bit words '11111111111111111111' and '11111011111111011111' in (a) original alignment to the short ends, and inter-element rearrangement with alignment (b) to the short end, and (c) to the open end.
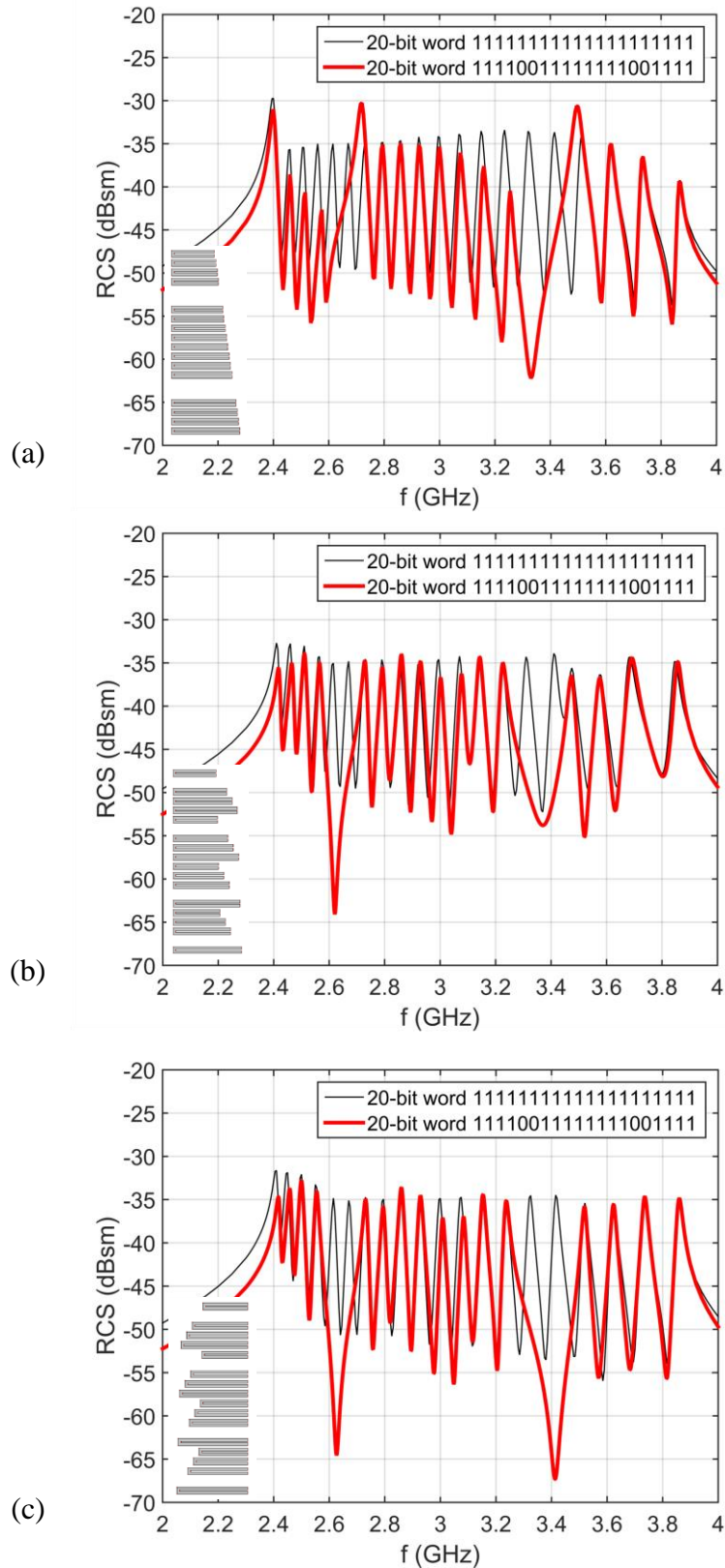
31

Fig. 4.4: Simulated *RCS* response of 20-bit chipless tag composed of array of the U-shaped strip scatterers representing bit words '11111111111111111111' and '11111001111110011111' in (a) original alignment to the short ends, and inter-element rearrangement with alignment (b) to the short end, and (c) to the open end.

Furthermore, the lowest and the highest resonant peaks in *RCS* curve of bit word '11111111111111111111' are significantly higher and lower, respectively, than the rest of the inner peaks. On the other hand, both element-rearranged arrays coding a bit word '11111011111111011111' exhibit missing resonances without the effect of distortion of magnitude and frequency interval uniformity of *RCS* curve; see Fig. 4.3b, c. The difference between the highest (-32 dBsm) and the lowest (-36 dBsm) *RCS* magnitudes is about 3-4 dB.

Simulated *RCS* response of 20-bit chipless tags representing a bit words '11111111111111111111' and '11111011111111011111' is depicted in Fig. 4.3. In case of reference tag; see Fig. 4.3a we may notice that due to removing of 6th and 15th scatterers corresponding resonant peaks are missing. However, two lower neighboring resonant peaks significantly reduced their magnitude and one higher neighboring peak increases its magnitude. The overall magnitude uniformity is thus deteriorated. The difference between the highest (-30 dBsm) and the lowest (-40 dBsm) *RCS* magnitude peaks is about 10 dB. Further, we may notice that the nearest lower and higher neighboring peaks slightly change their resonant frequencies in the direction to the original missing resonance. Thus, both magnitude and frequency interval uniformity of *RCS* response is worsen.

The element-rearranged configuration with alignment to the short ends exhibits slightly higher magnitude distortion of 16th to 18th resonant peaks. Further, we may notice, that the three lowest resonant peaks of a bit word '11111011111111011111' are about 2-3 dB higher than the rest of the peaks; see Fig. 4.3(b), (c).

The simulated *RCS* response of 20-bit chipless tag representing the bit words '11111111111111111111' and '11110011111111001111' is shown in Fig. 4.4.

In case of the original tag (Fig. 4.4a), it is obvious that due to removal of 5th, 6th, 15th and 16th scatterers, the corresponding resonant peaks are missing. In comparison to the previous case of the bit word '11111011111111011111', the effect of magnitude and frequency interval distortion of resonant peaks that are just next to the missing scatterer resonances is enhanced. The difference between the highest (-30 dBsm) and the lowest (-43 dBsm) *RCS* magnitude peaks is then about 13 dB; see Fig. 4.4a.

Again, both element-rearranged arrays coding the bit word '11110011111111001111' exhibit the missing resonances without significant effect of magnitude distortion and frequency interval uniformity of *RCS* curve; see Fig. 4.4(b), (c). The difference between the highest (-33 dBsm) and the lowest (-36 dBsm) *RCS* magnitudes is approx. equal to 3 dB. The element-rearranged configuration with alignment to the short ends demonstrates a slightly higher magnitude distortion of 16th to 18th resonant peaks. Furthermore, we may notice that the three lowest resonant peaks

of the bit word '11111011111111011111' are just by about 1-2 dB higher than the rest of the peaks; see Fig. 4.4b, c.
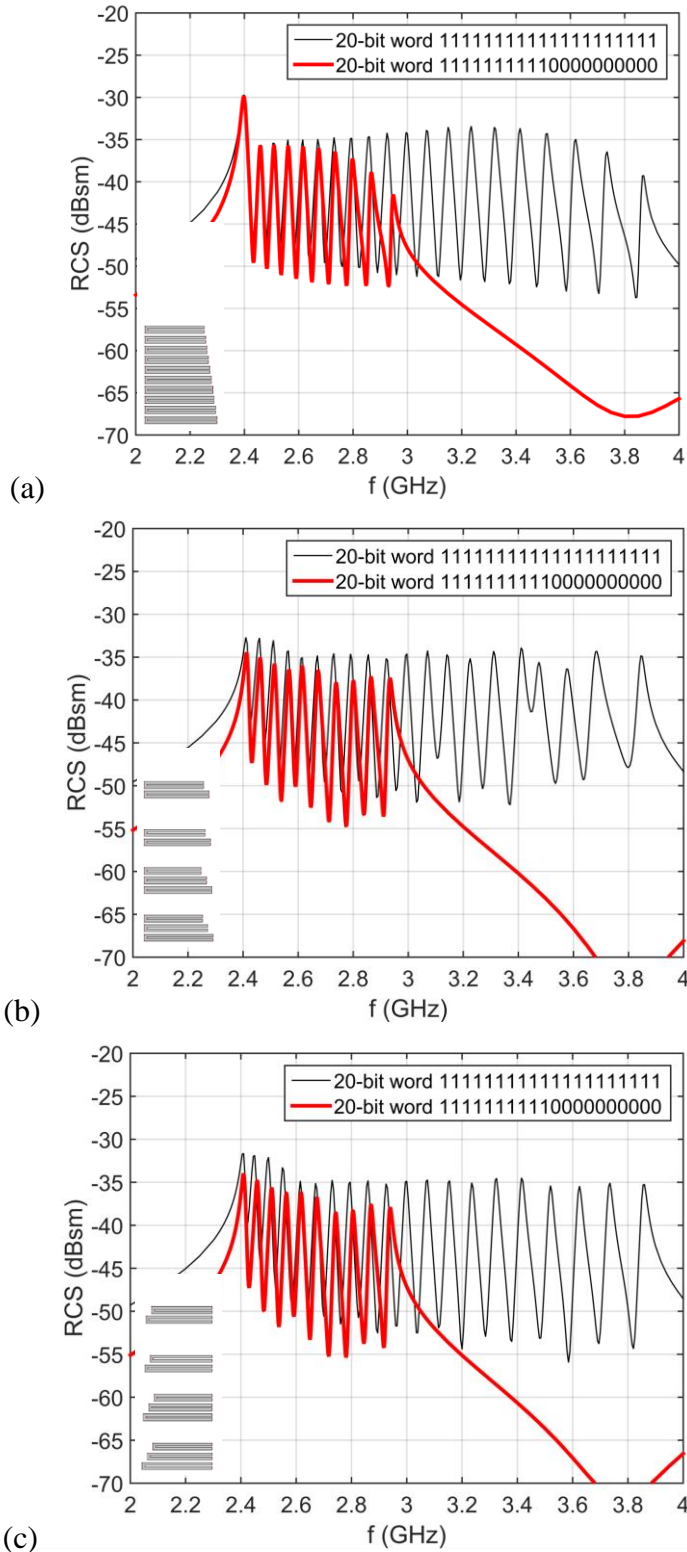

(a)

(b)

(c)

Fig. 4.5: Simulated *RCS* response of 20-bit chipless tag composed of array of the U-shaped strip scatterers representing bit words '11111111111111111111' and '11111111110000000000' in (a) original alignment to the short ends, and inter-element rearrangement with alignment (b) to the short end, and (c) to the open end.

Based on the above-presented simulation results, we may conclude that (compared to the reference tag configuration) the tag configurations with rearranged elements, where one or two '0' bits are coded, show a significantly improved robustness of *RCS* curve.

The tag reference configuration coding the bit word '111111110000000000' contains merely the lower half of scatterers of the reference tag. The difference between the highest (-30 dBsm) and the lowest (-42 dBsm) *RCS* resonant peak magnitudes equals about 12 dB; Fig. 4.5a. The frequency position of the two highest resonant peaks is, with respect to the bit word '111111111111111111', observably shifted to higher frequencies.

Both rearranged tag configurations exhibit considerably better magnitude uniformity of *RCS* curve than the reference tag. The difference between the highest (-35 dBsm) and the lowest (-38 dBsm) *RCS* resonant peak magnitudes of the bit word '111111110000000000' is of about 3 dB; see Fig. 4.5b, c. The frequency position of the highest resonant peaks of both rearranged configuration is less shifted to higher frequencies than in case of the reference tag configuration in Fig. 4.5a.

The presented simulation results predict that the tag configurations with rearranged elements, where the half of bits coding the '0' information, demonstrate (in comparison to the reference tag configuration) the highly improved amplitude robustness of *RCS* curve. Such amplitude uniformity and frequency stability of *RCS* peaks is crucial for the reliable reading of the bit information, especially in case that the distance between the reader and the tag makes the received power corresponding to the lowest resonant peaks of *RCS* curve reach the sensitivity threshold of the reader.

The tag that codes the bit word '101010101010101010' contains exclusively the odd scatterers of the reference tag. As a result, the mutual coupling of remained resonators is reduced due to their larger distance. Fig. 4.6a shows that the difference between the highest (-35 dBsm) and the lowest (-38 dBsm) *RCS* resonant peak magnitudes is cca of 3 dB.

Both element-rearranged tag configurations coding the bit word '101010101010101010' have nearly the uniform *RCS* curves, see Fig. 4.6b, c. The difference between the highest (-35 dBsm) and the lowest (-36 dBsm) *RCS* resonant peak magnitudes equals nearly 1 dB. The frequency position of resonant peaks is not observably affected. The especially element-rearranged tag configuration with alignment to the short end shows excellent magnitude uniformity as well as the frequency position stability of the *RCS* curve; see Fig. 4.6c.
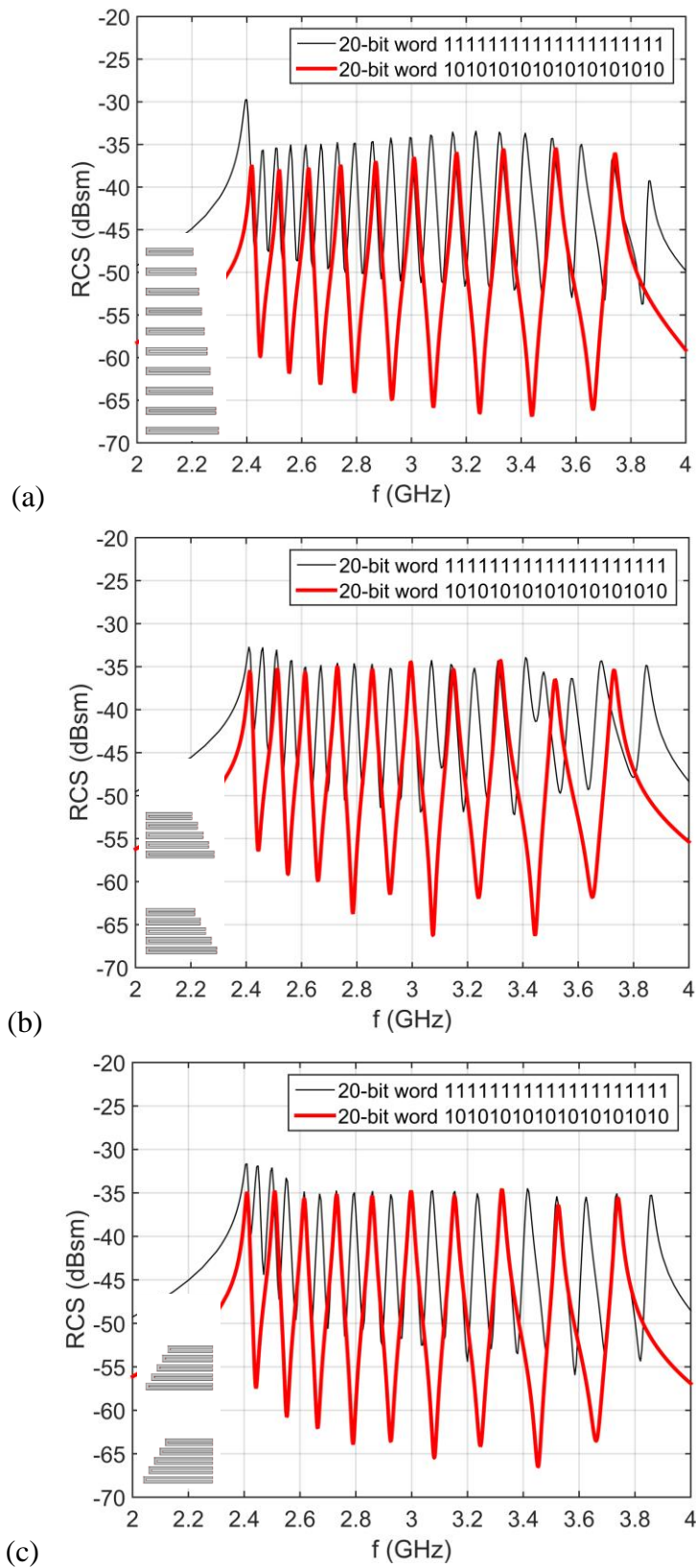
Fig. 4.6: Simulated *RCS* response of 20-bit chipless tag composed of array of the U-shaped strip scatterers representing bit words '11111111111111111111' and '10101010101010101010' in (a) original alignment to the short ends, and inter-element rearrangement with alignment (b) to the short end, and (c) to the open end.
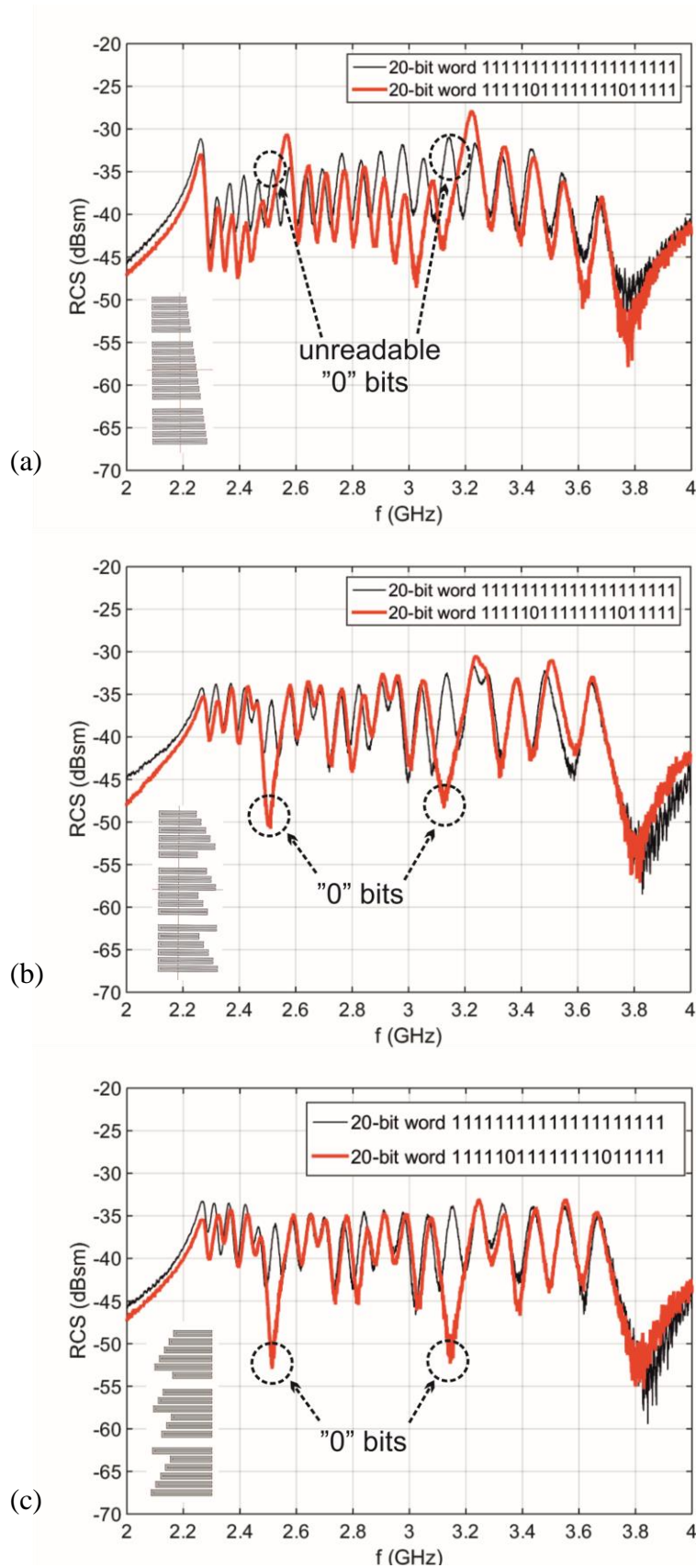
Fig. 4.7: Measured RCS response of 20-bit chipless tag composed of an array of the U-shaped strip scatterers representing a bit words '11111111111111111111' and '11111011111111011111' in (a) original alignment to the short ends, and inter-element rearrangement with alignment (b) to the short end, and (c) to the open end.

The monostatic measurement of tag *RCS* response was performed in an anechoic chamber in order to verify the simulated results; see subsection 4.4 for the description of the measurement method. The distance between the double ridge horn antenna DRH20 [86] and a measured tag was 750 mm. The rectangular metal plate used as a reference scatterer was 100×100 mm^2 in size and 0.3 mm in thickness. The measured data are smoothed to suppress the noise caused by a number of residual reflections. It was done in Matlab via the "smooth" function using the method "rloess" with the coefficient 0.015.

Fig. 4.7 illustrates the measured *RCS* response of all three 20-bit chipless tags, original arrangement aligned to the short ends [31], inter-element rearrangement aligned to the short ends, and to the open ends, representing a bit words '11111111111111111111' and '11111011111111011111'.

The two element-rearranged tag configurations provide a comparable uniformity of *RCS* curve. However, the second configuration aligned to the open ends of the scatterers exhibits a slightly better amplitude and frequency interval of the *RCS* robustness.

Another scatterer suitable for a tag design is the dual-spiral loaded dipole (DSLD) scatterer which is described and evaluated in chapter 3 as the S3 arm v2 dipole scatterer. The performance parameters of DSLD tags were investigated using the arrays of 20 elements, Fig. 4.8. The side-by-side arrangement whose size is gradually decreasing (Fig. 4.8a) represents the basic form with strong mutual coupling of neighbouring elements that negatively affects the *RCS* robustness. This phenomenon is obvious in the case that the zero bits are coded; see Fig. 4.9a. Resonance frequencies corresponding to the resonators next to the zero bit one (missing resonator) are shifted. Consequently, the bit information can be distorted.
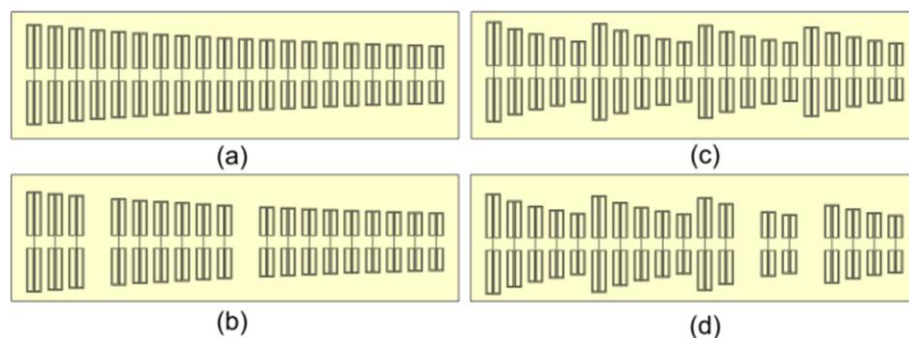

Fig. 4.8: Configurations of layouts of 20-bit chipless tag in linear arrangement, composed of array of the DSLD representing bit words '11111111111111111111' and '11101111110111111111'. (a, b) in side-by-side arrangement, (c, d) in element rearranged configuration.

To reduce the mutual coupling between neighboring elements, a modification of element arrangement proposed in [82] was used; see subsection 4.1.1. The original ascending order according to the element length '1 2 3 4 5 6 7 ... 20' is modified to '1 5 9 13 17, 2 6 10 14 18, 3 7 11 15 19, 4 8 12 16 20'; see Fig. 4.8c. In this layout, the resonators with neighboring resonance frequencies are located further apart and thus their coupling is substantially reduced. However, a small frequency shift can be observed on bit positions "7" and "8" and the *RCS* response uniformity does not attain satisfactory levels; see Fig. 4.9b. A circular arrangement was proposed in order to reach a sufficient level of uniformity; see subsection 4.1.2.
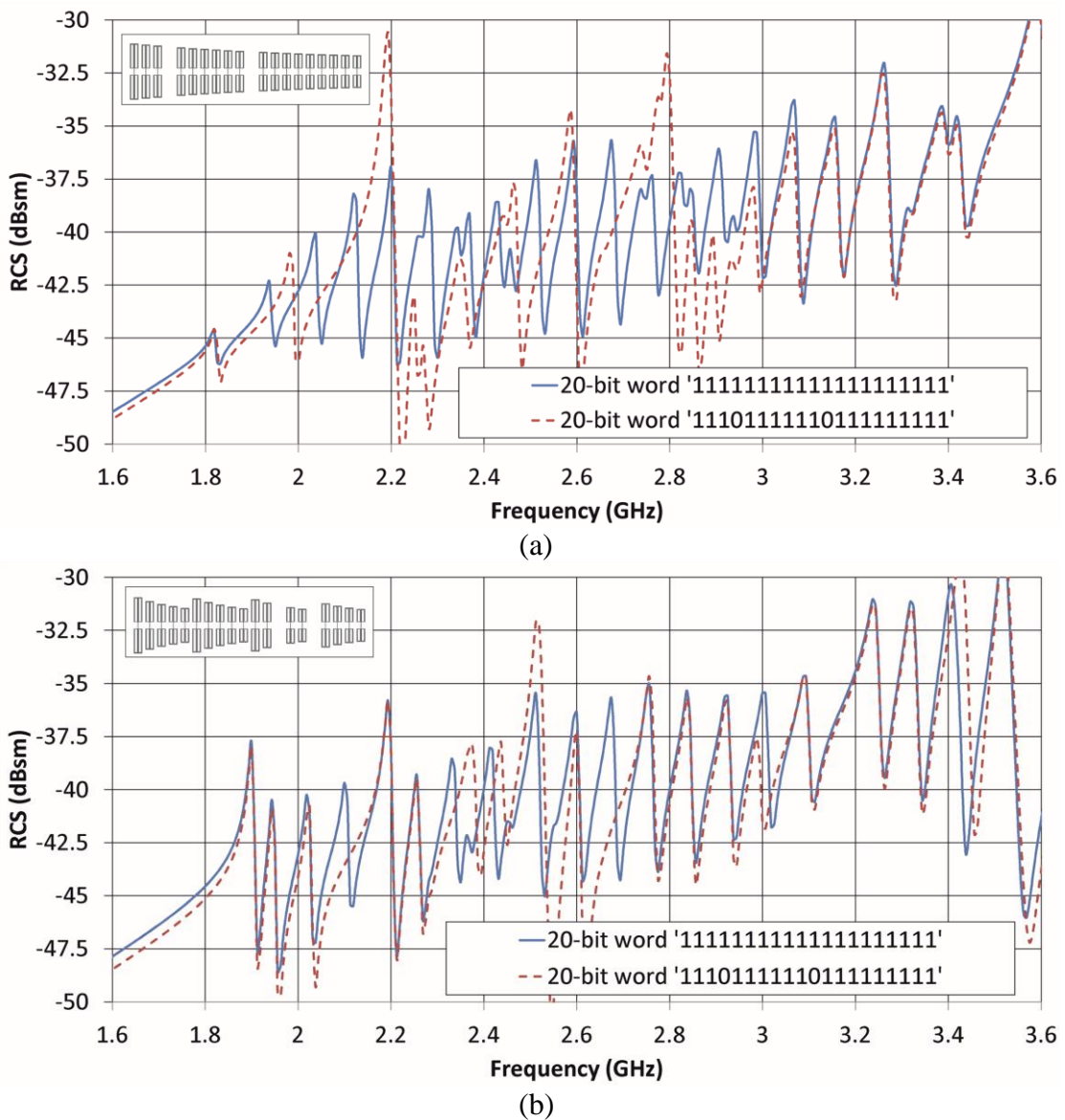

(a)

(b)

Fig. 4.9: Simulated *RCS* response of 20-bit chipless tag in linear arrangement, composed of array of DSLD representing bit words '11111111111111111111' and '11111011111111011111'. (a) in sequent arrangement, (b) in element rearranged configuration.

In both previously described cases, the outer size of the largest element is equal to 16.7×2.5 mm^2, while the dimensions of the smallest one equal 9.7×2.5 mm^2, with the strip width and the gap size of 0.1 mm. The distance between each two neighboring elements is 1 mm (20-bit tag size is 16.7×69 mm^2). The tag motive was etched on the low-loss dielectric substrate Rogers RO4350 ($\varepsilon_r = 3.66$, $\tan\delta = 0.002$) with the thickness of 0.254 mm. The incident excitation field is oriented parallel to the dipole length, i.e. vertically to the tags presented in Fig. 4.8. All presented structures were simulated by the method of moments Zeland IE3D software, using the infinite dielectric layer implementation with 20-cells per wavelength.

4.1.2 POLARIZATION INDEPENDENT TAG USING DUAL-SPIRAL LOADED DIPOLE IN CIRCULAR ARRANGEMENT

In this subsection, a circular arrangement of 20-bit electrically small dual-spiral loaded dipole scatterer (DSLD) array with improved robustness of *RCS* response is presented. Several capacitively loaded dipole scatterers were originally proposed in [77]; see chapter 3. To improve the frequency stability and amplitude uniformity of the chipless tag *RCS* curve, the scatterers were investigated in the circular arrangement, which enable the reduction in mutual coupling. In addition, this arrangement also ensures excellent *RCS* amplitude stability and polarisation independence at the expense of two-channel orthogonal polarisation measurement.

Given the results of single scatterer analysis [76, 77] completed by the study of *RCS* performance of scatterer development versions, the DSLD scatterer was chosen as a promising candidate for significant improvement of parameter performance of the chipless RFID tag. Compared to the thin strip U-dipole type scatterer of the same footprint size [31], it exhibits a higher *RCS* level (-33.5 vs. -35.0 dBsm), substantially smaller electrical size *ka* (0.35 vs. 0.62), and comparable 3 dB bandwidth (17.2 vs. 18.2 MHz); see Table 3.2 in section 3.2.

The 20-bit tag with circular arrangement was simulated by the method of moments Zeland IE3D software, using the infinite dielectric layer implementation with 20-cells per wavelength. Given that the IE3D enables the structure excitation by means of linearly polarized plane wave, the *RCS* response of circular arrangements was evaluated in two steps and the *RCS* response was calculated by the following relation:

$$\sigma_{dB} = 10\log\left(\sigma^E + \sigma^H\right) \tag{4.1}$$

where σ_{dB} stands for the simulated transponder *RCS* stated in dBsm; σ^E and σ^H represent the values of simulated transponder *RCS* in orthogonal polarization planes and linear scale, respectively.
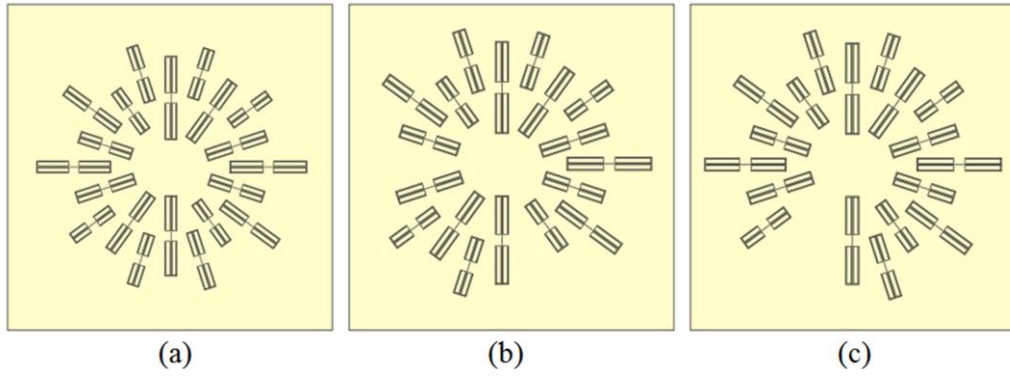
40

Fig. 4.10: Layout configurations of 20-bit chipless tag in circular arrangement, composed of array of DSLD in element rearranged configuration representing bit words: (a) '11111111111111111111', (b) '11101111110111111111', (c) '11111011111111011111'.
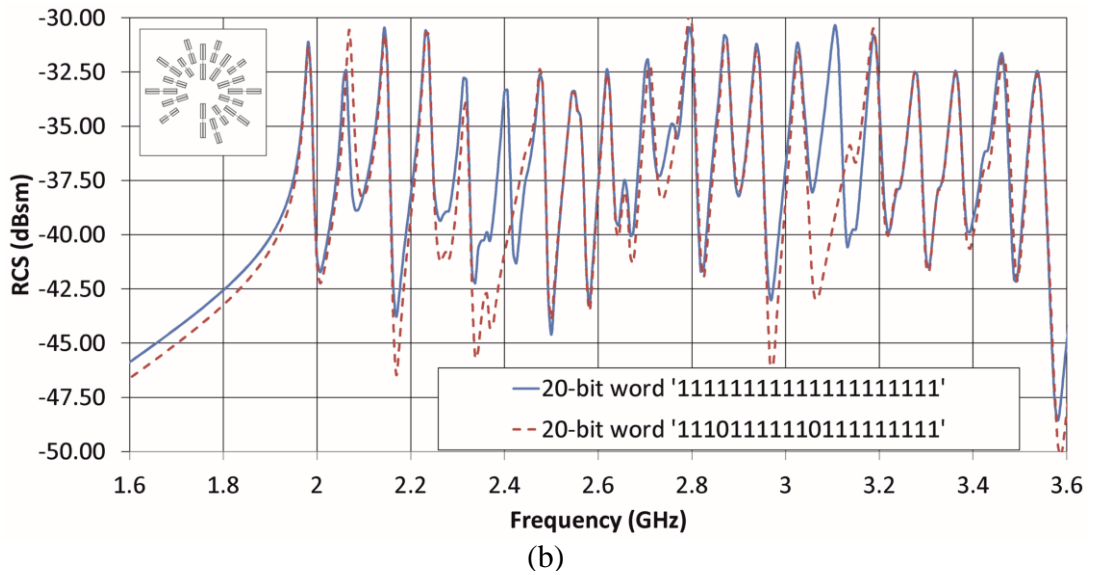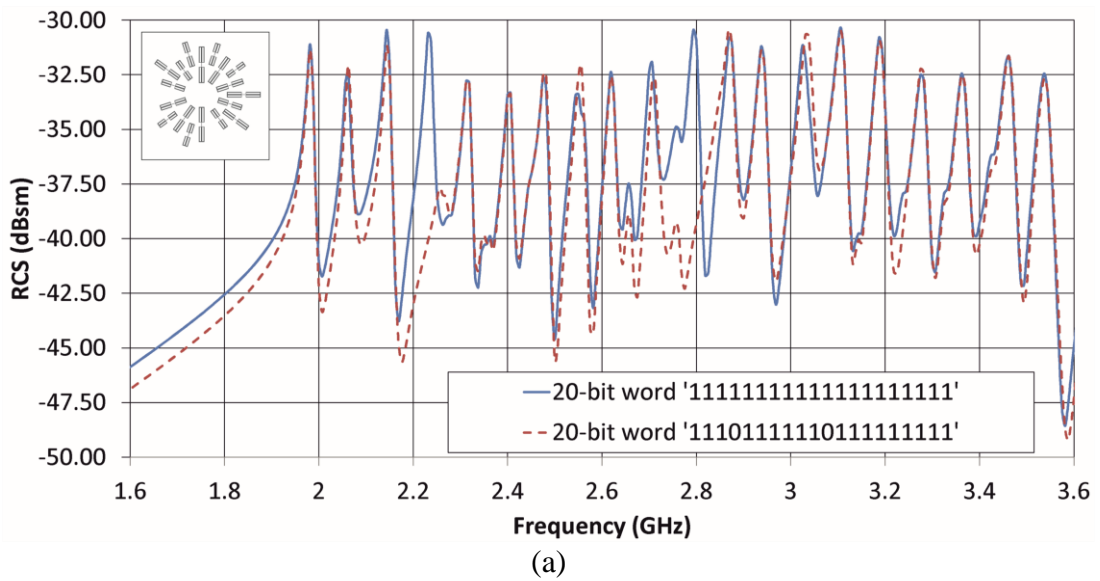

(a)

(b)

Fig. 4.11: Simulated *RCS* response of 20-bit chipless tag in circular arrangement, composed of array of DSLDs in element rearranged configuration representing bit words '11111111111111111111' and: a) '11101111110111111111', b) '11111011111111011111'.

The mutual coupling between particular DSLD scatterers, which can be partly reduced by the rearrangement described at the end of subsection 4.1.1, represents a drawback of these transponders. The amplitude uniformity and frequency stability can be further enhanced by placing the scatterers into circular arrangement, the elements being retained in the reordered position. As the neighboring scatterers are situated angle-wise and/or alternatively shifted into the circular pattern center (Fig. 4.10), the circular arrangement ensures a further reduction in mutual coupling between the elements.

Fig. 4.11 depicts significant improvement in *RCS* response uniformity as well as frequency stability. In addition, it offers the analysis and comparison of full 20-bits tag and two different tags with a pair of zero bits, situated in mutual distant as well as adjacent positions. Partial disadvantages of this solution are represented by the employment of two-channel measuring method and the use of two-port orthogonal-polarized antenna; see detailed description of the measurement method below. On the other hand, the polarization independence and excellent amplitude robustness of *RCS* response of circularly arranged transponder represent significant benefits.

The outer dimension of transponder equals 55×55 mm^2. The tag layout was etched on the low-loss dielectric substrate Rogers RO4350 ($\varepsilon_r = 3.66$, tan $\delta = 0.002$) with the thickness of 0.254 mm. The geometry and outer size of elements are the same as in the linear arrangement described at the end of subsection 4.1.1.
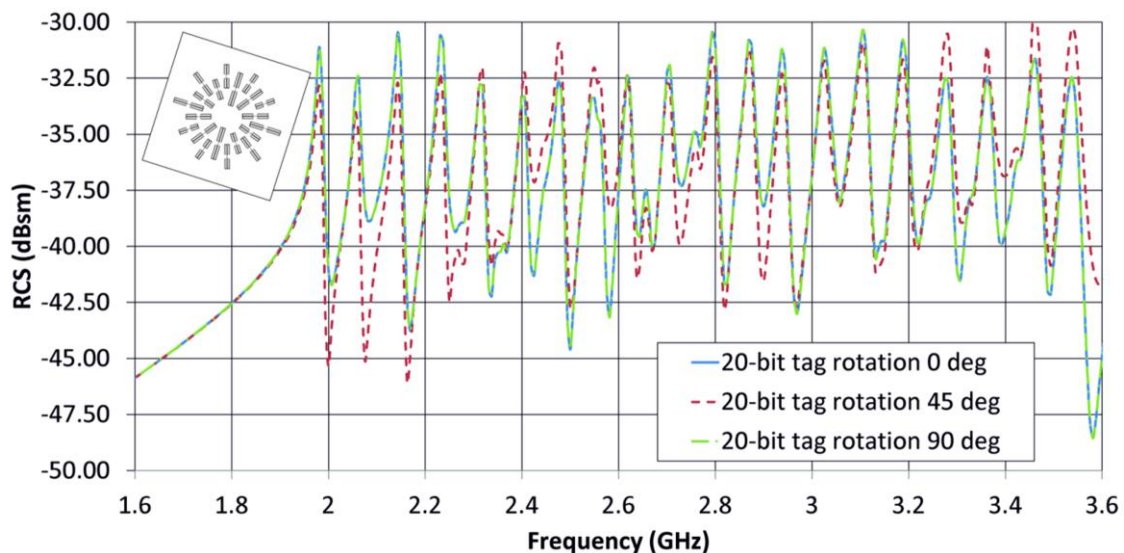

Fig. 4.12: Simulated verification of polarization independence of 20-bit chipless tag in circular arrangement, composed of array of DSLDs in element rearranged configuration representing bit word '11111111111111111111'.

As it was already indicated, the polarization independence constitutes a substantial benefit of circular arrangement that was verified by both, simulations and

measurements for the full 20-bits transponder representing the bit word '11111111111111111111'; see Fig. 4.12 and Fig. 4.15 respectively.

In conformity with expectations, the *RCS* responses for rotation angles 0° and 90° are completely identical. Small differences can be observed in the *RCS* response for the rotation angle 45°, yet the peaks resolution and consequently the bit word identification still attain satisfactory levels.

To verify the simulated results, the monostatic measurement of tag *RCS* similar to the method described in section 4.4 was performed in the anechoic chamber by means of R&S ZVA 40 network analyzer within the frequency band ranging from 1.6 to 3.6 GHz. The measurement was based on the evaluation of reflection coefficient of a quad ridge horn antenna QRH 20 [87] in front of which a transponder at distance of 0.25 m was placed; see Fig. 4.13. Reflection coefficients of both antenna orthogonal inputs were measured simultaneously by two-port VNA Model. As the far field for the horn aperture diagonal of the size of 0.1 m equals about 0.17 m at 2.5 GHz ($2D^2/\lambda_0$), the condition for evaluation of *RCS* by measurement was fulfilled.

The calculation of *RCS* response of the transponder was performed in line with the relation used in [82] and modified so that it was applicable to the two-port orthogonal case that is in line with (4.1).

$$\sigma^{tag} = 10\log\left|\frac{\left(S_v^{tag} - S_v^{iso}\right)}{\left(S_v^{ref} - S_v^{iso}\right)} + \frac{\left(S_h^{tag} - S_h^{iso}\right)}{\left(S_h^{ref} - S_h^{iso}\right)}\right|^2 \sigma^{ref} \qquad (4.2)$$

where S_v^{tag} and S_h^{tag} are the vertical (port-1) and horizontal (port-2) reflection coefficients for the case that the measured tag is used as a scatterer. S_v^{ref} and S_h^{ref} represent the reflection coefficients in the case that the reference plate is employed as a scatterer. S_v^{iso} and S_h^{iso} symbolize the reflection coefficients of antenna itself in the case that no scatterer is used and comprises the residual reflection from experimental surroundings. σ^{tag} stands for the *RCS* of measured tag and σ^{ref} embodies the reference
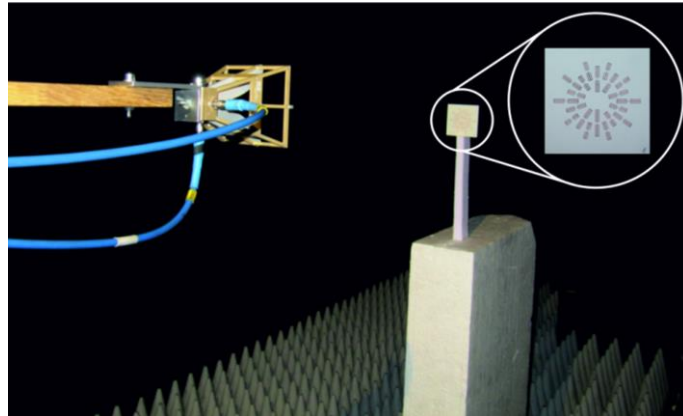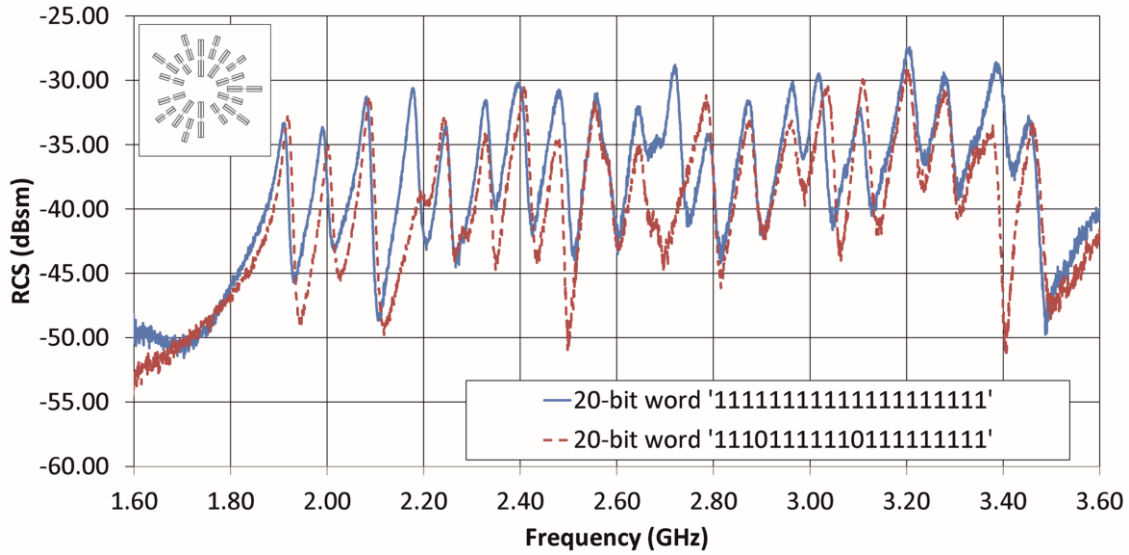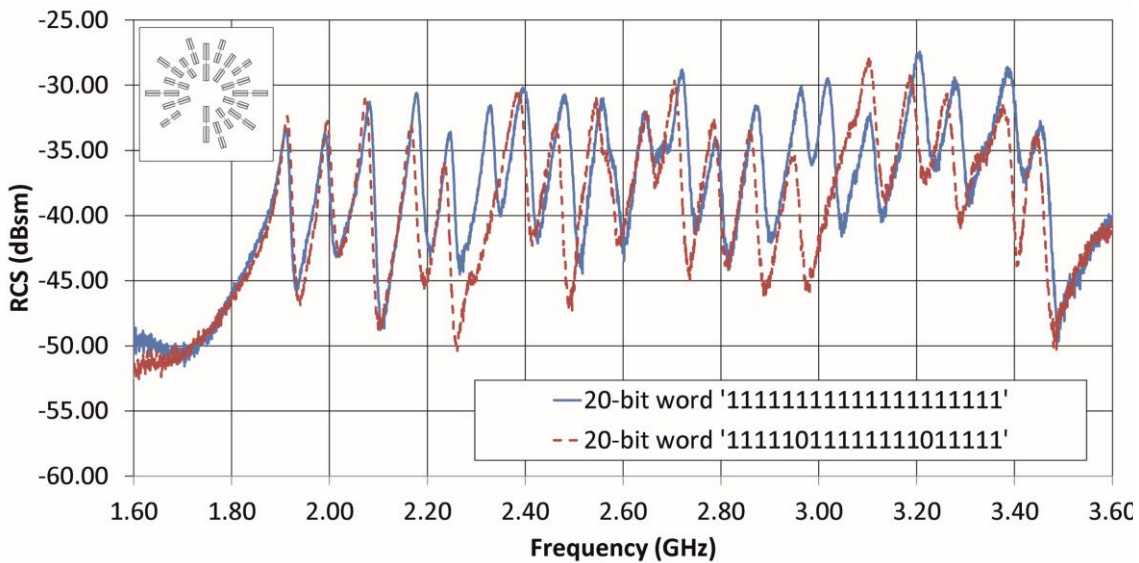

Fig. 4.13: Measurement setup using monostatic configuration, detailing circular element-rearranged 20-bit tag.

scatterer *RCS*, which is the rectangular metal plate of 60×60 mm^2 in size (corresponding with the measured tags) and 0.3 mm in thickness. Its analytical formula for *RCS* is equation (4.10) in section 4.4.

(a)

(b)

Fig. 4.14: Measured *RCS* response of 20-bit chipless tag in circular arrangement, composed of array of DSLDs in element rearranged configuration representing bit words '11111111111111111111', and (a) '11101111110111111111', (b) '11111011111111011111'.

Fig. 4.14 shows the measured *RCS* response of 20-bit chipless tag in circular arrangement. Full 20-bits tag and two different tags with pair of zero bits (in distant as well as adjacent positions to each other) were compared, see b, c. Significantly improved *RCS* response uniformity and a good frequency stability were confirmed.

Moreover, the depth of peaks better than 5 dB over the whole operating frequency band can be observed.

The measurement results of *RCS* response in several different angle orientation conformed the polarization independence of circularly arranged transponder; Fig. 4.15. Contrary to simulations showed in Fig. 4.11, the *RCS* response for the rotation angles 0° and 90° are not fully identical in this case. It is due to the non-identical placement of transponder in the measuring position.
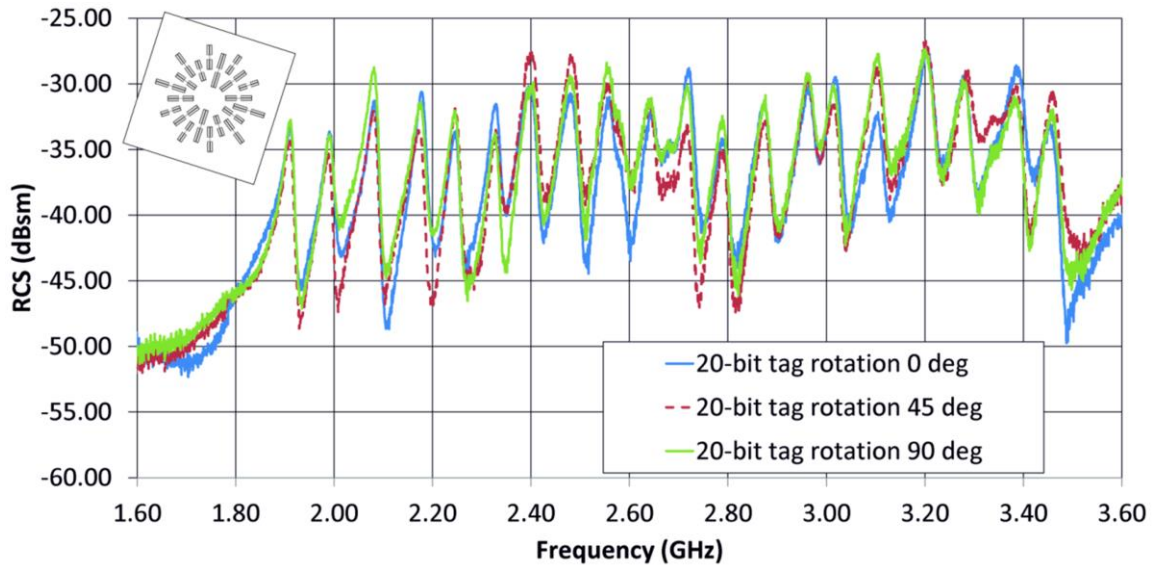

Fig. 4.15: Measured verification of polarization independence of 20-bit chipless tag in circular arrangement, composed of array of DSLDs in element rearranged configuration representing bit word '11111111111111111111'.

4.2 EQUIVALENT CIRCUIT MODELING OF MUTUAL COUPLING IN U-DIPOLE SCATTERER ARRAY

This section proposes a topological modification of the individual scatterer based on the work [34, 88, 89], which improves the amplitude uniformity of *RCS* response of the whole tag including the peak-to-valley level, frequency stability and resolution (increased *Q* of scatterers), providing significantly higher encoding capacity within the specified frequency range. The reduction in the resonant frequency of coding particle
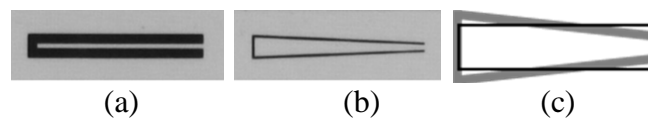

Fig. 4.16: Layouts of investigated modifications of folded-dipole scatterers. (a) U-folded dipole (UD), (b) Tapered U-folded dipole (T-UD), (c) Approximation of the T-UD by a rectangular loop.

allows to decrease the size occupied by the scatterer, and thus to increase the density of coded information per area unit. As demonstrated by an equivalent circuit modelling, mutual coupling between the resonators is reduced by inclination of their arms so that the adjacent resonators are located effectively at a longer distance [85]. Further, the decreased inter-element mutual coupling positively affects amplitude uniformity and frequency stability of resonant peaks in *RCS* response of tags that code the logical "0" by removing scatterers. Unfortunately, as it was expected, both improvements are at the expense of the *RCS* response reduction of the proposed transponder.

The geometry of the proposed uniplanar strip scatterers was inspired by the U-folded dipole presented in [31]. In order to correctly compare the performance of the proposed scatterer with the one investigated in [31], the scatterers were designed and analysed on the low loss substrate Rogers RO4003 ($\varepsilon_r = 3.38$, tan $\delta = 0.002$) of the 0.2 mm thickness, providing planar resonators with a lower dielectric loss and higher Q than those manufactured onto 0.8 mm FR-4 substrate used in [31, 34].

The original U-folded dipole (UD) scatterer of the outer size 20×2.5 mm^2 with the 1 mm strip width and the gap size of 0.5 mm, which is in accordance with [31] is shown in Fig. 4.16a. Modified tapered U-folded dipole (T-UD) scatterer of the same outer size is depicted in Fig. 4.16b.
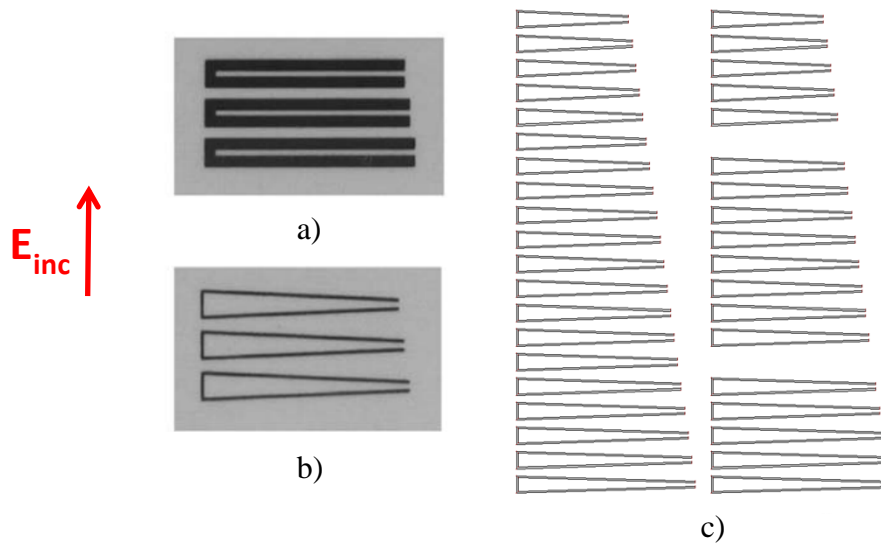

Fig. 4.17: Investigated groups of U-folded dipole scatterers: a) U-folded dipole (UD) triplet, b) tapered U-folded dipole (T-UD) triplet and c) 20-element arrays coding information 11111111111111111111, and 11111011111111011111 by missing 6th and 15th elements.

The geometrical modifications consist in narrowing the strip width from original 1 mm to 0.25 mm to enable to taper the gap between the longitudinal dipole arms toward the open end to 0.5 mm. This taper shape reduces the mutual coupling between two neighbouring coding particles, because their arms are more spatially separated. As it is indicated in Fig. 4.17a, b, the fabricated triplets consist of three scatterers that are

20, 19.5, and 19 mm in length and of the same width. The distance among them at short ends is 1 mm, which is the same as in [31]. All scatterers are placed on the substrate that extends their dimensions by about 3 mm at each side of the scatterer.

The scatterer triplets were measured in the R32 waveguide setup, while being fixed on a thin polystyrene stand and located at the transversal position in the centre of the waveguide section that is 37 mm long and inserted between the reference planes. The free space *RCS* is then extracted from the measured S-parameters by the procedure described in [90]. The performance properties of scatterer triplets that are 20 mm in length are as follows; see Table 4.1.

Scatterer	Resonant frequency (GHz)	3 dB bandwidth (MHz)	*RCS* lowest (dBsm)
Original UD	3.20	16.7	-46.5
Tapered UD	2.75	17.8	-44.7

Table 4.1: Measured performance properties of the highest resonant peak of scatterer triplets.

The highest resonant peak of the scatterer triplet composed of original dipoles (UD) shows the resonant frequency of 3.20 GHz, which exceeds 2.75 GHz reached in the case of tapered dipole. This means that the proposed T-UDs are relatively smaller and therefore assure a higher density of information per tag unit surface. The lowest *RCS* peak of scatterer UD triplet is -46.5 dBsm (@ f = 3.2 GHz) which is only about 1.8 dB lower than the lowest *RCS* peak of T-UD triplet -44.7 dBsm (@ f = 2.756 GHz).
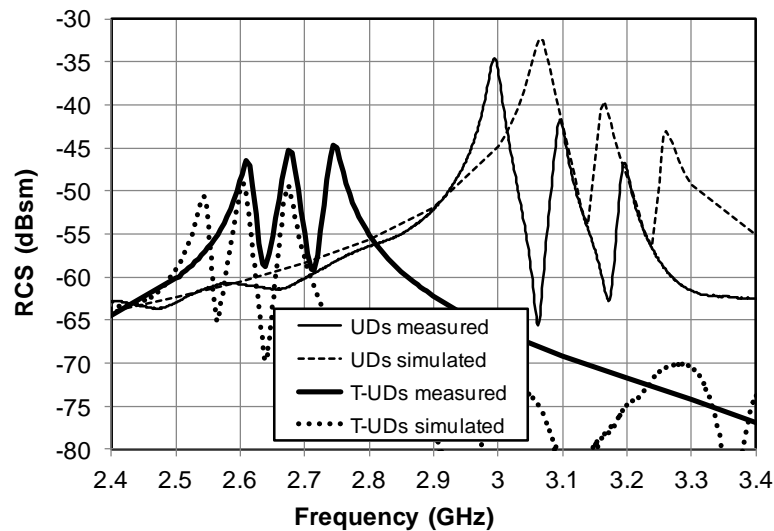

Fig. 4.18: Simulated and measured *RCS* response of triplets of original UD and T-UD.

As it can be seen in Fig. 4.18, the arrangement of particular scatterers closely spaced into the triplet detunes the resonant frequencies due to the mutual coupling. Namely in case of UD, we can obviously observe a significant non-uniformity of *RCS* response magnitude. The tapering of gap between the dipole arms of the T-UD by about 4.5° from the original parallel direction reduces the mutual coupling, see Fig. 4.20. As a result, the amplitude uniformity of *RCS* response of T-UD is significantly improved.

The issue of coupling scatterers is analyzed using an equivalent circuit model where the ith single resonator is composed of a series resonant circuit L_i, C_i, and R_i, see Fig. 4.19 [84]. The circuit is fed by the source of voltage V_i that corresponds to the incident electric field E irradiating the tag

$$V_i = E\, l_{ieff} \tag{4.3}$$

where l_{ieff} is effective length of the ith resonator working as a receiving antenna. Changing amplitudes and phases of V_i we can simulate oblique incidence of the wave, or its different forms – planar, cylindrical, spherical. The presented analysis is done for the perpendicular incidence of the plane wave, so all voltages are taken $V_i = 1$ and are in-phase. Magnetic field of the reflected wave excited by dipoles corresponds linearly to the current flowing along these dipoles [91]. Predicted *RCS* is therefore proportional to the power of sum of currents in particular resonators of the equivalent circuit [92]

$$RCS \sim \left(\sum_{i=1}^{20} I_i\right)^2 \tag{4.4}$$

The particular resonant circuits are coupled by magnetic field, and this coupling is represented by mutual inductances. The coupling coefficient decreases with increasing
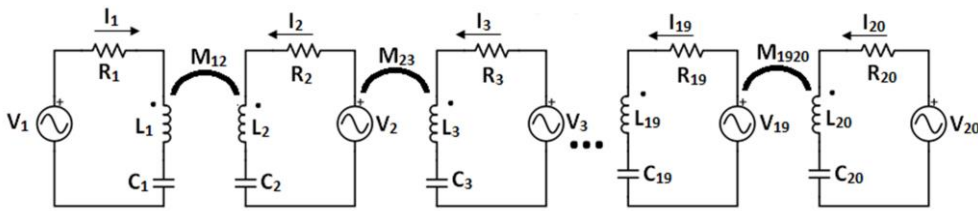

Fig. 4.19: Equivalent circuit of the tag composed of 20 resonant elements.

distance as shown in Fig. 4.20. Consequently, it is sufficient to consider only coupling of neighboring resonators. It has been proved by analyzing the circuit from Fig. 4.19 by adding mutual inductances even between the second neighbors.

The missing resonator that in the tag codes bit with logical '0" is represented by a circuit with resistance $R_i = 1$ MΩ that assures nearly zero value of the passing current and consequently no (or negligible) contribution to the response (4.4). Equations for each loop in the circuit from Fig. 4.19 read

$$-V_1 + (R_1 + X_{L1} + X_{C1})I_1 + X_{M12}I_2 = 0 \qquad (4.5.1)$$

$$-V_2 + (R_2 + X_{L2} + X_{C2})I_2 + X_{M12}I_1 + X_{M23}I_3 = 0 \qquad (4.5.2)$$

$$\cdots$$

$$-V_{19} + (R_{19} + X_{L19} + X_{C19})I_{19} + X_{M1819}I_{18} + X_{M1920}I_{20} = 0 \qquad (4.5.19)$$

$$-V_{20} + (R_{20} + X_{120} + X_{C20})I_{20} + X_{M1920}I_{19} = 0 \qquad (4.5.20)$$

where $X_{Li} = j\omega_{Li}$, $X_{Mij} = j\omega_{Mij}$, and $X_{Ci} = 1/(j\omega_{Ci})$. Solution of (4.5) determines the particular currents and the tag *RCS* response (4.4).

The folded dipoles showed in Fig. 4.16a, b can be viewed as current loops and their inductance and mutual inductance of a pair of the loops can be calculated by using the Neumann's formula, as, e.g., in [91] p. 234

$$M = \frac{\mu_o}{4\pi} \iint \frac{dl_1 \cdot dl_2}{|r_{12}|}, \qquad (4.6)$$

here dl_1 and dl_2 are elements of the loops and r_{12} is the oriented distance between these elements. To simplify the calculation, the original folded dipole is substituted by the current loop located at inner edges of strips, the tapered U-folded dipole is substituted by the rectangular current loop as drawn in Fig. 4.16c. The distribution of current passing along the dipoles arms described by sine function is approximated by its average value equal to $2/\pi$.

The coupling coefficient that describes the mutual inductance between the pair of elements with inductances L_1 and L_2 and mutual inductance M is defined by a standard way

$$\kappa = M/\sqrt{L_1 L_2}. \qquad (4.7)$$

The coupling coefficient of adjacent pairs of UDs, T-UDs, and rearranged UDs, see Fig. 4.16, Fig. 4.17 and Fig. 4.2, 25 and 25.5 mm in length located at distance *a* is plotted in Fig. 4.20. The mutual coupling of T-UDs is significantly weaker than the coupling between UDs. This proves the basic advantage of the proposed tapered U-folded dipoles. The method of mutual inter element coupling reduction using the resonator positions rearrangement in subsection 4.1.1 [82] is less effective, see corresponding coupling coefficient in Fig. 4.20.

Fig. 4.20 further shows line marked CST UD representing the transmission between two UDs calculated by the CST Microwave Studio. The two resonators are fed by point ports connected to the open end. This verifies the behavior described above.
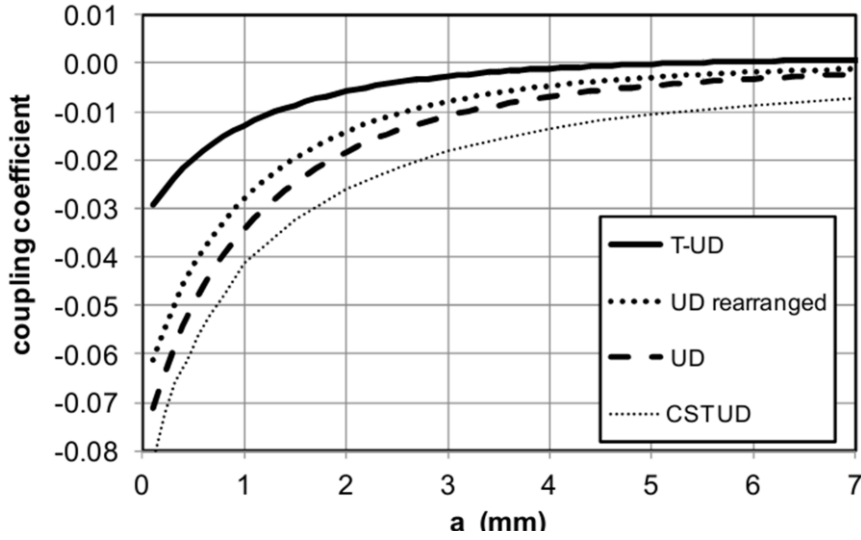
Fig. 4.20: Coupling coefficient of adjacent pairs of original UDs [31], T-UDs [78], and rearranged UDs [82].

The results of the equivalent circuit analysis (*RCS*) are normalized by considering all exciting voltages equal to 1 V. A rough estimate of *RCS* can be calculated by Eq. (4.4). The equivalent circuit analysis was applied to evaluate performance of up to 20-element arrays of proposed T-UD. The scatterers were sequentially detuned by changing their length by 0.5 mm from 16 to 25.5 mm, so the outer size of the array was 69×25.5 mm^2, see Fig. 4.17c [78].

The circuit parameters in the equivalent circuit were determined by procedure of calculation data for Fig. 4.20. Capacitances were calculated from resonant frequencies of particular resonators and their inductances. Resistor values were evaluated using skin effect [91]

$$R_i = l_i/(\sigma 2\delta w), \tag{4.8}$$

where l_i is total length of the strip w in width, σ is conductivity, and δ is penetration depth.

RCS response according to equivalent model depicted in Fig. 4.21 shows the response of the tag composed of 18 and 20-element UDs from Fig. 4.16a. The resonators are coupled here relatively strongly. The exceptions are in the case of the first and the last resonators. They have neighbors from only one side, so *RCS* at maximum of the first resonator response is higher than in the case of others, *RCS* at maximum of the last resonator is lower. Solid line shows response of the tag with particular UD resonators removed to code logical zero. Peaks adjacent to missing resonances are strongly distorted both in amplitude level and frequency position. Strong element coupling thus makes difficult to read properly the coded information and predicts that such kind of elements are not suitable for implementing chipless RFID tags.

i	f_{oi} (GHz)	l_i (mm)	L_i (nH)	κ_i (-)	R_i (Ω)
1	2.074	25.5	16	-0.024	0.3
2	2.110	25	15.7	-0.0238	0.295
3	2.159	24.5	15.4	-0.0236	0.29
4	2.200	24	15.1	-0.0234	0.285
5	2.252	23.5	14.8	-0.0232	0.28
6	2.296	23	14.5	-0.023	0.275
7	2.342	22.5	14.2	-0.0228	0.27
8	2.390	22	13.9	-0.0226	0.265
9	2.447	21.5	13.6	-0.0224	0.26
10	2.500	21	13.3	-0.0222	0.255
11	2.559	20.5	13	-0.022	0.25
12	2.624	20	12.7	-0.0218	0.245
13	2.692	19.5	12.4	-0.0216	0.24
14	2.763	19	12.1	-0.0214	0.235
15	2.833	18.5	11.8	-0.0212	0.23
16	2.903	18	11.5	-0.021	0.225
17	2.985	17.5	11.2	-0.0208	0.22
18	3.067	17	10.9	-0.0206	0.215
19	3.157	16.5	10.6	-0.0204	0.21
20	3.254	16	10.3	-0.0202	0.205

Table 4.2: Elements of the equivalent circuit from Fig. 4.19 used to calculate RCS of the tag from Fig. 4.17c as presented in Fig. 4.22.
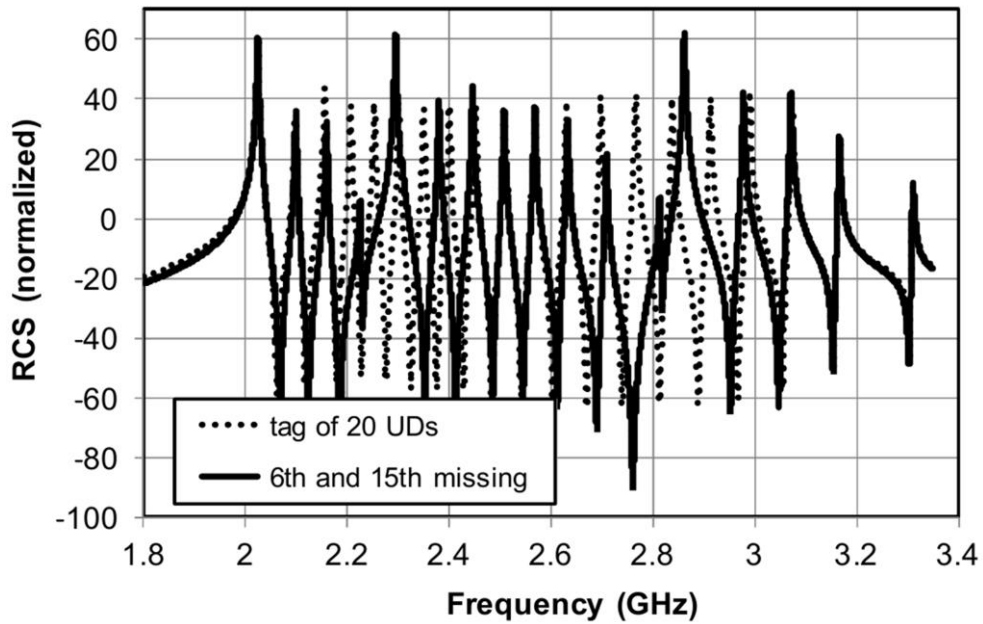
Fig. 4.21: Predicted RCS response of the equivalent circuit of 20-element tag composed of U-folded dipoles compared with the 18-element version coded by missing 6th and 15th elements.
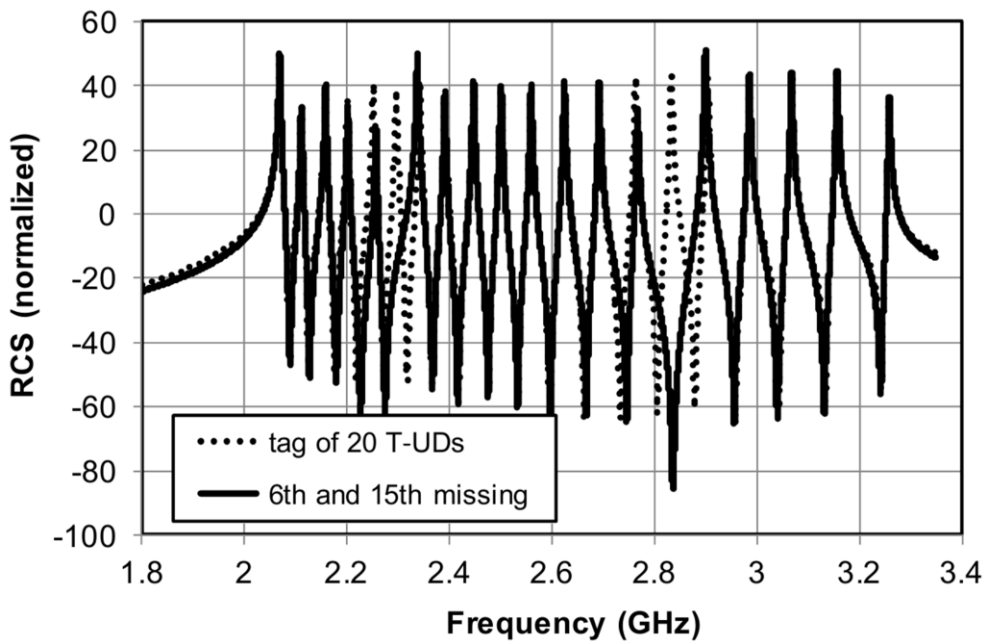

Fig. 4.22: Predicted RCS response of the equivalent circuit of 20-element tag composed of tapered U-folded dipoles from Fig. 4.17c compared with the 18-element version coded by missing 6th and 15th elements.

On the other hand, weak mutual coupling in case of an array of proposed T-UD resonators of Fig. 4.16b presented in [78] assures stable amplitude level and frequency positions of adjacent resonant peaks. Consequently, it enables their reliable identification in comparison with the *RCS* response of the full 20-bit tag; see Fig. 4.22.

Table 4.2 lists parameters of the equivalent circuit used to analyze the tag from Fig. 4.17c.

Method using equivalent circuit was also applied to array of planar resonators proposed in subsection 4.1.1 [82]. The positions of resonators in the array are rearranged according Fig. 4.2a. The result of the *RCS* response is in Fig. 4.23 It is possible to distinguish reliably the missing resonances of the missing resonant elements. The amplitudes and frequency positions of adjacent resonant peaks are not affected. The plot documents again the suitability of that simple solution to predict the tag behavior documented by measured *RCS* in Fig. 4.7b.

Besides the calculation with the help of the equivalent circuit, *RCS* response of the tag composed of T-UDs was simulated by Zeland IE3D software. The frequency range between the lowest and highest resonant peaks of UD and T-UD are approx. 1.5 and 1.2 GHz, respectively; see Fig. 4.3a and Fig. 4.24. This means that the proposed 20-element T-UD array provides approx. 1.25times higher information capacity per unit frequency range.
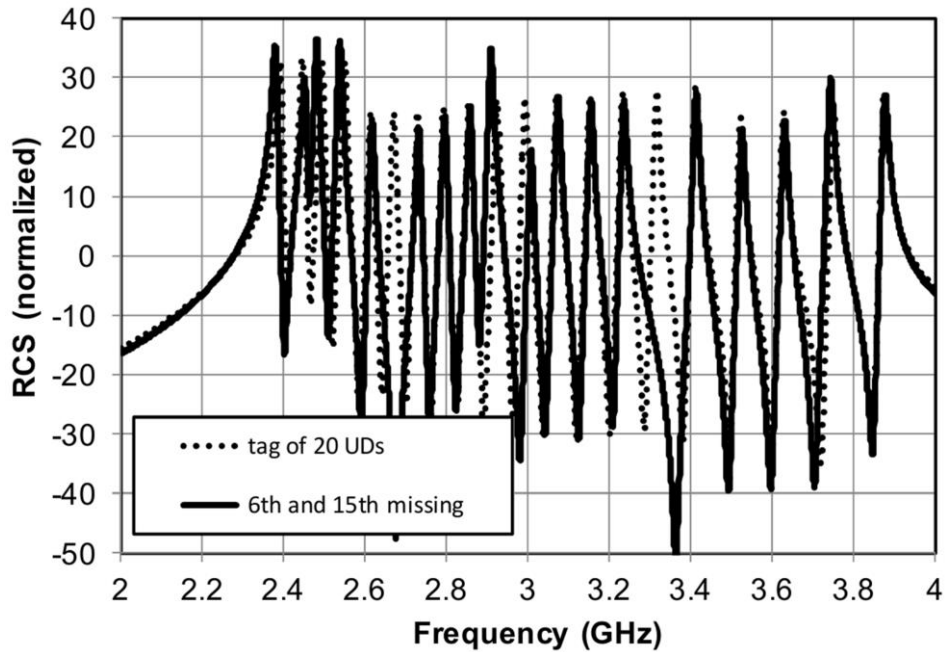

Fig. 4.23: RCS response of the equivalent circuit of 20-element tag with rearranged resonators [31], compared with the 18-element version coded by missing 6th and 15th elements from Fig. 4.2a.

In order to verify the influence of bit coding on the shape of the spectra, we removed the 6th and 15th scatterers; see Fig. 4.17c. We have found that the spectra of the original U-folded 20-element array exhibit an extensive change, namely in the case of resonant peaks neighbouring the removed one. These two peaks significantly alter their magnitudes; the lower one decreases, while the upper one increases by about 2 to 3 dB.

Furthermore, their resonant frequencies are detuned to the position of original resonance; see Fig. 4.3a. The same effect is presented in the results of Vena et al.; see Fig. 4 in [31].
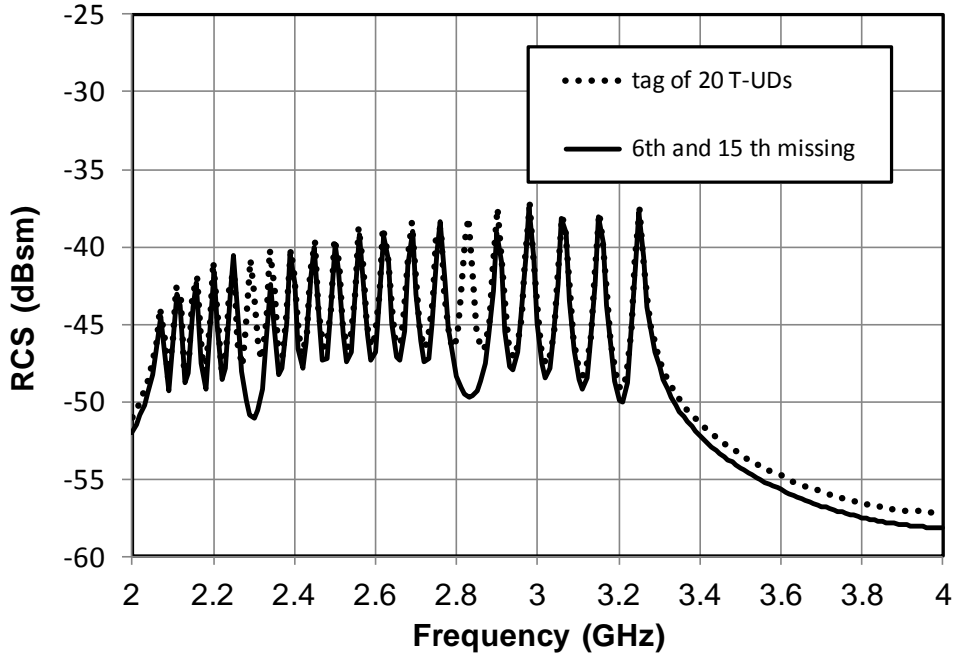

Fig. 4.24: Simulated *RCS* response of 20-element tag composed of tapered U-folded dipoles. compared with *RCS* of the version coded by missing 6th and 15th elements.

Consequently, the "0" bits are nearly invisible in the tag spectral response. On the other hand, such unwanted behaviour has not been observed in case of 20-element T-UD array; see Fig. 4.24 showing the simulation results, and Fig. 4.25 the measured data. The resonant peaks neighbouring the missing peaks remain exactly at the same frequency position and their magnitude change is considerably smaller than in the case of UD array. Moreover, a better amplitude uniformity and frequency stability of the *RCS* response of T-UD compared to UD array is apparent.

The T-UDs have smaller effective area due to the tapering than the UDs. These results in smaller *RCS* in comparison to the UDs by approximately 7-10 dBsm, see Table 4.1. As a consequence, the sensitivity of the proposed tag is lower than the original.

Fabricated tags were tested by one-port vector measurement of monostatic *RCS* in a free space described in section 4.4. Distance between measured scatterers and antenna DRH 20 was 150 mm. The received power for this distance was calculated with the use of equation (4.11) as approximately -52 dBm for the frequency band center, which is value with sufficient reserve in comparison with the noise threshold of the VNA or another receiving device. However, relatively low measurement distance was used to

guarantee significantly higher reflection from the measured tag in comparison with a number of residual reflections from the experimental surroundings. Consequently, clear RCS response can be evaluated from this measurement according equation (4.9).
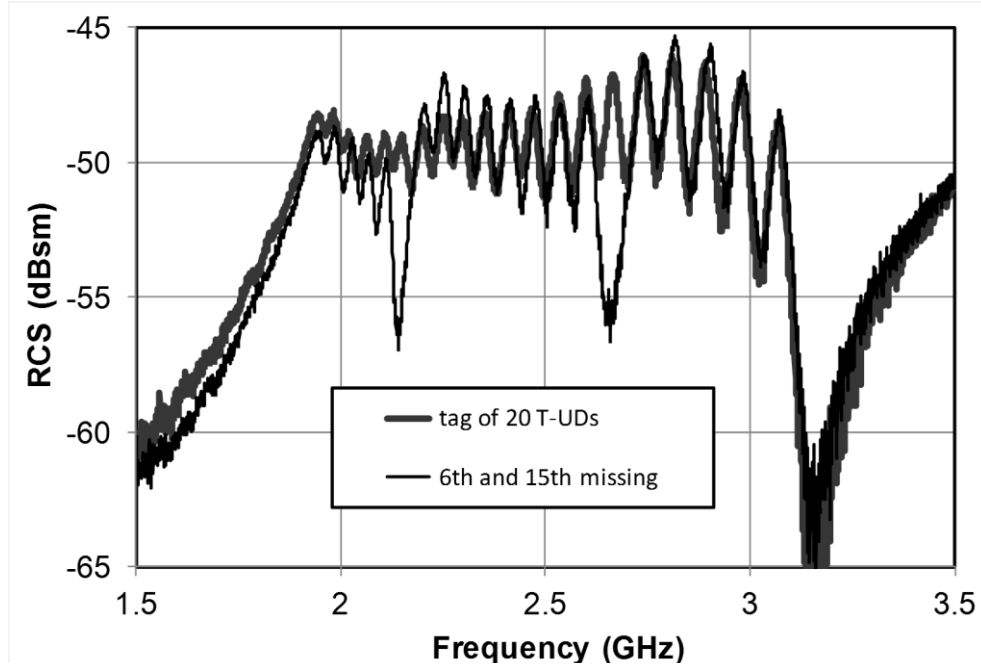

Fig. 4.25: Measured *RCS* response of 20-element tags composed of tapered U-folded dipoles coding information 11111111111111111111 – tag with 20 elements, and 11111011111110111111 – tag coded by missing 6th and 15th elements.

The results of the equivalent circuit analysis plotted in Fig. 4.22 are corresponding with experimental data in Fig. 4.25 [78, 85] showing measured *RCS* response of the T-UD tags composed of 20 and 18 resonators. What cannot be exactly compared is the level of the *RCS* response. The *RCS* calculated from the equivalent circuit represents normalized values as all voltages are taken equal to 1 V regardless of dipole effective lengths, and *RCS* values are substituted by the sum of currents (4.4). Predicted *RCS* shown in Fig. 4.22, and measured in Fig. 4.25, proves the suitability of structure, i.e. recognisability of individual resonances, from Fig. 4.17c to design the RFID tag. Measured *RCS* characteristics of the tag composed of UDs can be seen in Fig. 4.7a.

The coupling coefficient between two T-UD resonators, Fig. 4.17c, at their distance equal to 1 mm is -0.013. This is a sufficiently low value that assures reliable reading the coded information, see Fig. 4.22 and Fig. 4.25. To get the same behavior of the tag composed of UDs, Fig. 4.2, the distance between resonators must be increased to 2.7 mm, then the size of the tag would be significantly increased.

4.3 THE TAG USING SPIRAL LOADED DIPOLE

In this section, an electrically small spiral loaded (S-loaded) dipole [80] scatterer is presented and compared to the U-folded scatterer [31]; see chapter 3 and subsection 4.1.1. The advantage of the S-loaded dipole scatterer over the U-folded scatterer consists in the smaller electrical size and higher RCS, which is beneficial for both, the spectral bit capacity and spatial bit density. The scatterer design also reflects a mutual coupling minimization, which ensures the frequency and amplitude stability of RCS response. The scatterer suitability for chipless RFID design was investigated using an assembly of 20-bit tags manufactured on 0.254 mm thin microwave dielectric substrate. With regard to the current advancement in conductive ink printing technology, it can be supposed that achievable tolerances of this promising technology will enable mass production of the presented structure in the near future. To verify the simulated results, the monostatic measurement of tag RCS described in section 4.4 was performed using VNA and double ridge horn antenna [86].

A topology of the U-folded dipole scatterer [31] is described in chapter 3; see the Fig. 4.26a. The scatterer shows sufficient RCS = -34.3 dBsm and a narrow bandwidth BW_{3dB} = 18.1 MHz (0.49 %). However, its disadvantage is embodied in a mediocre factor ka = 0.79 among all treated scatterers; see Table 4.3. The performance parameters of all investigated scatterers were simulated in a free space using MoM IE3D software.

Scatterer	f_r (GHz)	area (mm^2)	ka (-)	σ (dBsm)	BW_{3dB} (MHz)	BW_{3dB} (%)
U-folded dipole [31]	3.66	51.3	0.79	-34.3	18.1	0.49
S-loaded U-folded dipole	2.56	18.9	0.21	-58.9	19.4	0.76
S-loaded dipole (asymmetrical)	2.194	20.7	0.47	-29.3	20.9	0.95

Table 4.3: Parameters of investigated single scatterers.

One of the most forthright design approaches to lower the ka factor of U-folded dipole is to add spiral ending loads. In order to fit the spirals between U strips, the width of all lines is reduced to 0.1 mm. It remains within the tolerance limit of common photo-etching technology. The scatterer occupies the rectangle area of 7.55 × 2.5 mm^2. The spacing between lines of the spiral endings is equal to 0.1 mm and the width of spirals is 1 mm; see Fig. 4.26b. The high level of electric length reduction (ka = 0.21) of the respective scatterer is attained in exchange for the inappropriate level of σ = -58.9 dBsm. The bandwidth BW_{3dB} = 19.4 MHz (0.95 %) slightly exceeds the U-folded dipole value; see Table 4.3. Such a scatterer cannot be used for chipless tag assembling due to an overly low RCS.

The necessary *RCS* improvement is reached after the U-folded shape is abandoned; see Fig. 4.26c. The spiral loaded dipole scatterer then occupies the rectangle area of 20.5×1.3 mm^2. The width of all lines is 0.1 mm, while the spacing between spiral arms accounts for 0.1 mm. The distance between spiral endings is equal to 2 mm. The last scatterer shows $\sigma = -29.3$ dBsm and $BW_{3dB} = 20.9$ MHz. These values are comparable to those of a basic U-folded dipole, yet its level of electric length reduction ($ka = 0.47$) is considerably better; see Table 4.3.
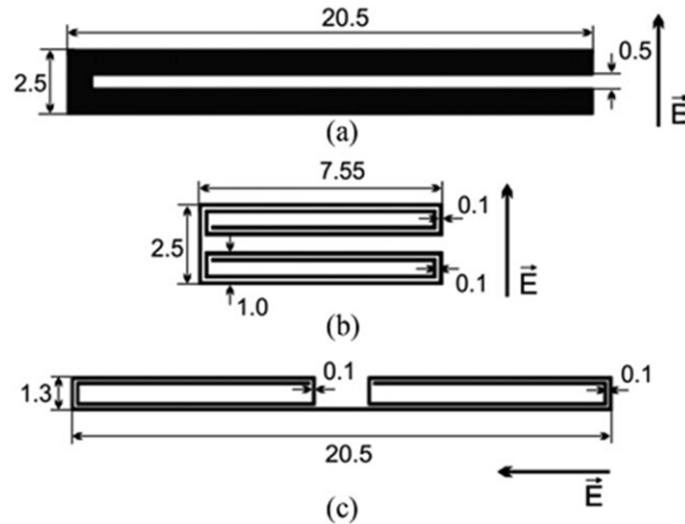

Fig. 4.26: Scatterer layouts (identical scale). (a) U-folded dipole scatterer (b) U-folded spiral loaded dipole scatterer and (c) spiral loaded dipole scatterer. All dimensions are stated in mm. Polarization of excitation field is denoted by E-field vector arrow.

The principle of chipless RFID tags based on the frequency domain method is to encode the bit information into tag's *RCS* response, which consists of a series of resonant peaks of particular scatterers. Presence or absence of the peak/scatterer represents one or zero bit, respectively. Due to its negative influence on the amplitude uniformity and frequency stability of the *RCS* response peaks, it is necessary to minimize especially the mutual coupling between neighboring scatterers in the tag, so that a high tag readability is achieved. The geometry of S-loaded dipole is asymmetrical around the axis of incident electric field; see Fig. 4.26c. This is convenient for mutual coupling reduction as the currents of adjacent strips of the closest scatterers are oriented in opposite directions; see Fig. 4.27. The symmetrical dual S-loaded dipole (DSLD) was investigated at the end of section 4.1.1; however, its mutual coupling is excessively strong. Consequently, the DSLD scatterers can be used for tag assembly in diagonal arrangement, which is highly inefficient from the spatial point of view [77], or in circular arrangement, which demands more difficult measurement method; see subsection 4.1.2 [79].
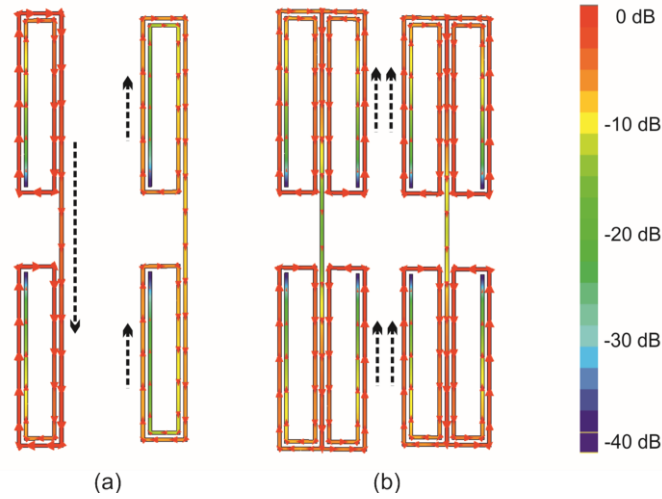
Fig. 4.27: Simulated currents distribution of S-loaded dipole scatterers pair in (a) asymmetrical and (b) symmetrical geometry. Dashed arrows denote orientation of adjacent strips currents.

Scatterer of the transponder	*RCS* min/max (dBsm)	Min peak-to-valley difference (dB)	Spectral bit capacity (bit/GHz)	Space bit density (bit/cm^2)	Uniformity of RCS response
U-folded dipole [31]	-37/-34	1.3	13.1	1.1	good
Dual-spiral loaded dipole	-38/-34	4.5	10.0	1.74	average
S-loaded dipole (asymmetrical)	-41/-30	2.1	12.5	1.77	Quasi-monotonously increasing

Table 4.4: Parameters of investigated 20-bit tags.

In order to encode the 20-bit information, the array of 20 S-loaded dipoles (each of them having a slightly different resonance frequency) is proposed to operate within the frequency range from 2.0 to 3.6 GHz; see Fig. 4.28c. The tag size is 16.7×67.8 mm^2. The simulated tag performance is compared with the one of the tag consisting of twenty U-folded dipoles [82]; see Fig. 4.29, Fig. 4.28 and Table 4.4 designed for the same frequency band. The size of U-folded dipole tag is however approximately twice as large, i.e. 29.5×69 mm^2. The lengths of both scatterer types are designed so they reach approximately 80 MHz frequency spacing between neighbouring resonance peaks. The distances between each two neighbouring elements are 1 mm and 2.2 mm for respectively the U-folded dipole tag and the one using S-loaded dipoles.
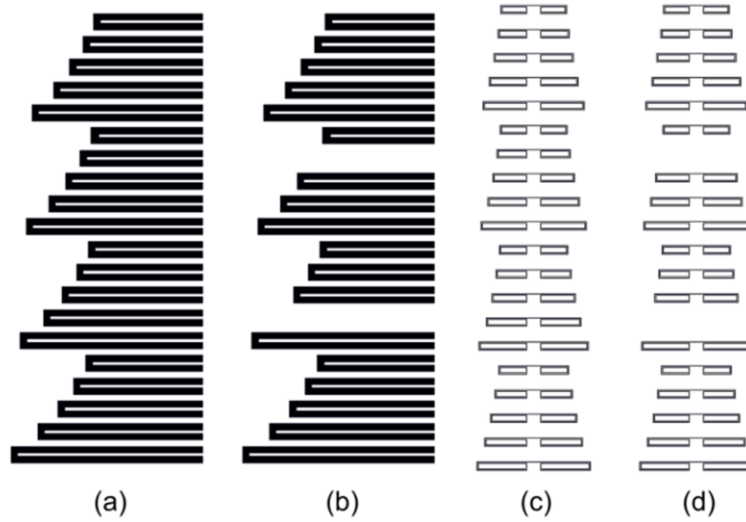
Fig. 4.28: Layouts of 20-bit chipless tags composed of array of U-folded dipoles (a, b) and S-loaded dipoles (c, d), both using rearrangement published in and both encoding bit words ''11111111111111111111' (a, c), and '11111011111111011111' (b, d).

For additional improvement in amplitude uniformity as well as frequency stability of *RCS* response (*RCS* response robustness) by reducing the mutual coupling between neighboring scatterers, a modification of scatterer arrangement proposed in [82] is used in both tag designs. The original ascending order according to the element length '1 2 3 4 5 6 7 ... 20' is modified to '1 5 9 13 17, 2 6 10 14 18, 3 7 11 15 19, 4 8 12 16 20'; see subsection 4.1.1 and Fig. 4.28. In this layout, the resonators with neighboring resonance frequencies are then located further apart, which gives rise to a substantial reduction in their coupling.

The performance of both tags is investigated for two different bit words in order to prove that the impact of mutual coupling on *RCS* response stability does not prevent reading of tags. The tags containing twenty scatterers represent the bit word '11111111111111111111', whereas the tags with only 18 scatterers encode the bit word '11111011111111011111'; see Fig. 4.28a, c and Fig. 4.28b, d respectively.

The incident excitation field is parallel to the dipole lengths in the case of spiral loaded dipole tag and perpendicular to the dipole arms in the case of U-folded dipole tag; see Fig. 4.26. The tags performance was simulated on the low-loss dielectric substrate Rogers RO4350 ($\varepsilon_r = 3.66$, tan $\delta = 0.003$) with the thickness of 0.254 mm; see Fig. 4.28. The same substrate was also used to manufacture the tags in order to verify the simulated *RCS* responses by the monostatic measurement.

The resonant peaks of simulated *RCS* response of the tag using U-folded dipoles, which encodes the basic bit word '11111111111111111111' differ from each other at the most by 2 dB; see Fig. 4.29a. Moreover, we can observe 2 dB differences in comparison to responses of different bit words in Fig. 4.29a. This arises from resonant

peaks number '2' and '11'. Likewise, in the said peaks, there are resonant frequency shifts amounting to ca. 10 MHz that are not vital for information reading though. The respective peaks belong to scatterers that are adjacent to the removed scatterers number '6' and '15'; see Fig. 4.28b. The difference between the resonant maxima and minima ranging from 14 dB to 20 dB was obtained in simulations only. The measured values vary between 3 and 10 dB [82].
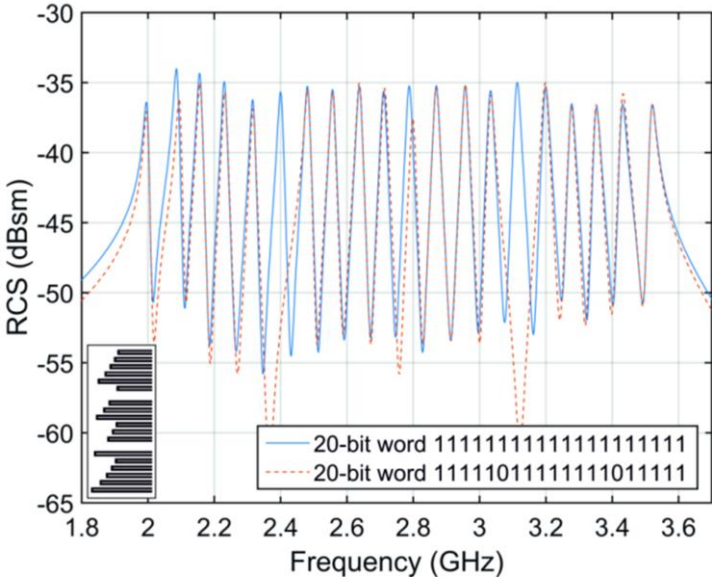
(a)
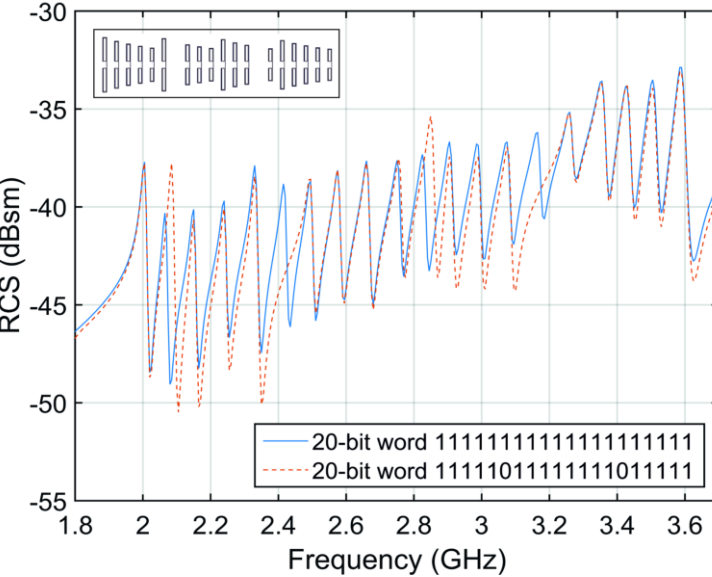
(b)

Fig. 4.29: Simulated *RCS* responses of 20-bit chipless tags composed of array of U-folded dipoles (a) and S-loaded dipoles (b), both encoding bit words '11111111111111111111', and '11111011111111011111'.

The resonant peaks of simulated *RCS* response of S-loaded dipole tag differ at the most by 7 dB, i.e. in the case of bit word containing only logical ones; see Fig. 4.29b. Nonetheless, the *RCS* curve shows a quasi-monotonous rise and is quite stable when different bit words are encoded. The cause of the rise is currently rather unclear. The deeper analysis, e.g. numerical, of this effect falls outside the intended scope of the paper. However, it is likely to be related to unequal size relations of the loaded spiral and dipole length with frequency tuning.

Hence for reading purposes, it would be simple to compute different thresholds for each resonant peak in order to make a logical value decision. The peak-to-valley value ranges froM3.5 dB to 10 dB. The information encoding conducted via scatterer removal also results in shifts in *RCS* magnitude and resonant frequency of the peak numbers '2' and '11'. The respective peaks belong to resonators next to the removed ones ('6' and '15'). The peak amplitude shift accounts for approximately 2 dB, while the frequency shift is equal to 25 MHz, which is acceptable from information reading point of view as well.

To verify the simulated results, the monostatic measurement of tags *RCS* performance was made in an anechoic chamber; see section 4.4. It was based on the reflection coefficient evaluation of the double ridge horn antenna DRH20 [86] in front of which a scatterer at a distance of 150 mm was placed. The tag's *RCS* response was calculated with the help of the relation used in [31] and modified so that it was applicable to the one-port case described in [82].
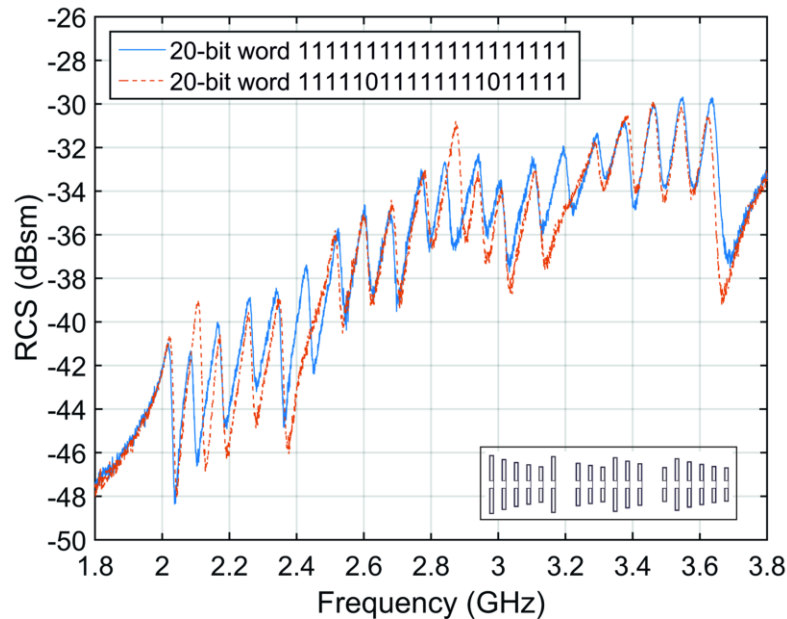

Fig. 4.30: Measured *RCS* response of 20-bit chipless tags using rearranged S-loaded dipoles, representing bit words '11111111111111111111', and '11111011111111011111'.

Measured *RCS* response of 20-bit chipless tag, which consists of rearranged spiral loaded dipoles encoding two bit words according to Fig. 4.28c, d is depicted in Fig. 4.30. It is identical to the simulated ones mentioned above. The *RCS* levels of resonant peaks range from -41.5 dBsm to -30 dBsm. The decision threshold for bit evaluation can be set as (in parts) monotonously constant or increasing curve interleaving the resonant peaks. It is conspicuous in both, the simulated and measured results. The peak-to-valley value ranges from 2 dB to 7 dB, which is slightly less than in simulation. The response of bit word '11111011111111011111' suffers from a minor distortion in comparison to the full word '11111111111111111111', which is similar to the simulated one. In general, the measured and simulated responses sufficiently correspond to each other.

4.4 ONE-PORT VECTOR MEASUREMENT METHOD OF MONOSTATIC RCS

All simulated results and other properties of the presented transponders were verified using one port measurement method of monostatic *RCS* described in this section unless otherwise stated. Completely different measurement method was used in the case of time-domain chipless RFID system, which is proposed in chapter 5.
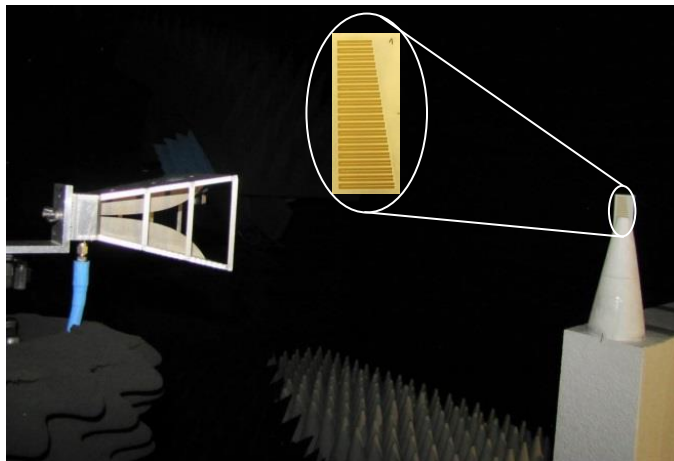

Fig. 4.31: Measurement setup using monostatic measurement configuration with an example of the 20-bit tag.

The monostatic measurement was utilizing an R&S ZVA 40 network analyzer within the frequency band of 1.5 to 4 GHz in an anechoic chamber; see Fig. 4.31. The measurements were based on the evaluation of the reflection coefficient of a double ridge horn antenna DRH 20 [86] in front of which a transponder was placed. The far field for a horn aperture diagonal of length 0.1 m is about 0.2 m at 3.5 GHz ($2D^2/\lambda_0$), meeting the condition required to perform accurate *RCS* measurements. The monostatic measurement arrangement in comparison with bistatic enables to avoid the use of

angular dependent formula for reference scatterer and eliminates the influence of mutual coupling between the transmitting and receiving antenna.

The calculation of transponder *RCS* response by means of monostatic measurements was performed according to the following relation [93]:

$$\sigma^{tag} = 20\log\left|\frac{S_{11}^{tag} - S_{11}^{iso}}{S_{11}^{ref} - S_{11}^{iso}}\right|\sigma^{ref} \tag{4.9}$$

where $S_{11}{}^{tag}$ is the reflection coefficient, provided that the measured tag is used as a scatterer. $S_{11}{}^{ref}$ is the reflection coefficients, when the reference plate is used as a scatterer. $S_{11}{}^{iso}$ is the reflection coefficient of the antenna itself in the case where no scatterer is used, which takes into account the residual reflection from experimental surroundings. σ^{tag} is the measured tag *RCS* and σ^{ref} represents the *RCS* of the reference scatterer, which is a rectangular metal plate of size $a \times b$ (same as the size of corresponding measured tag). An analytical formula for the *RCS* is given as follows:

$$\sigma^{ref} = 4\pi\frac{a^2b^2}{\lambda^2} \tag{4.10}$$

The measurement received power P_R can be determined using the well-known radar equation [94]:

$$P_R = \frac{\sigma^{tag}\lambda^2 G^2}{(4\pi)^3 r^4}P_T \tag{4.11}$$

where r is a distance between the antenna and the tag with RCS equal to σ^{tag}, VNA transmitted power P_T equals 10 dBm and gain of the transmitted/received antenna G is 8 dBi.

4.5 SUMMARY

Inter-element rearrangement of the 20-bit spectral signature-based chipless RFID tag composed of U-shaped strip scatterers significantly improved the uniformity and amplitude robustness of the *RCS* response; see subsection 4.1.1 [82]. The improvement in the *RCS* response has been obtained by replacing individual scatterers that originally adjoined the frequency spectrum further apart. Such amplitude uniformity and frequency stability of *RCS* curve is crucial for reliable recognition of all bits (presence/absence of resonant peaks) of the tag. This is especially important in case that the distance between the reader and the tag causes that the received power corresponding with the lowest peaks of *RCS* curve will reach the sensitivity threshold of the reader.

The improved uniformity of individual resonance peaks on the *RCS* curve has been verified on four tags that encode different bit words. The two proposed tag configurations provide a comparable uniformity of *RCS* curve. However, the second

configuration aligned to the scatterers' open ends exhibits a slightly better amplitude and frequency interval of the *RCS* robustness, mainly in case of the bit word '10101010101010101010'. It can be concluded that chipless RFID tags that use the proposed kind of inter-element rearrangement represent promising candidates for reliable recognition of coded information.

A chipless RFID tag, which is based on electrically small dual-spiral loaded dipole (DSLD) scatterers (chapter 3) was proposed and investigated in subsection 4.1.2 [79]. In order to significantly improve its performance parameters through minimization of mutual coupling between frequency-adjoined scatterers, they are arranged in a circular array, where elements are re-ordered and odd elements are radially shifted. The transponder exhibits a higher spectral bit capacity (11.1 vs. 10 bit/GHz) than the reference U-dipole transponder [77]. Its comprehensive encoding bit capacity is 45.3 bit/λ^2/GHz, which is lower than 57.1 bit/λ^2/GHz achieved by U-dipole transponder but higher than capacity of other polarization independent transponders compared in [93]. This performance parameter is evaluating a tag size in λ^2 instead of cm^2 and it was introduced in order to correctly compare tags designed for different bandwidths. In other words, a fair comparison of frequency-domain passive chipless RFID transponders requires frequency re-scaling.

In comparison to the side-by-side arrangements (subsection 4.1.1) and competitive solutions, the concurrently proposed circular arrangement exhibits excellent frequency stability and amplitude uniformity of the *RCS* response at the expense of lower spatial bit density (0.7 vs. 1.1 bit/cm^2 of U-dipole tag). The difference between the measured level of minimum and maximum *RCS* peak of single tag scatterers equal approx. 15, 12, and 3 dB for side-by-side, rearranged side-by-side, and circular arrangements, respectively. Furthermore, the proposed solution ensures the polarization independence of identification, yet in the exchange for the necessity to employ the two-channel measuring method.

Proposed chipless RFID tag composed of topologically modified uniplanar U-folded dipoles with inclined arms requires about 20% smaller frequency range for coding 20-bit information in the same unit area than the reference scatterer array composed of original U-folded dipoles with parallel arms; see section 4.2 [78].

The topology is designed to reduce the inter-element mutual coupling and thus provides a better amplitude uniformity and frequency stability of tag *RCS* response when logical "0" is coded by removing particular scatterers from the array. However, both improvements are achieved at the expense of small *RCS* magnitude reduction.

Further, the influence of mutual coupling between individual scatterers of chipless RFID tag on its *RCS* response was investigated by simplified equivalent circuit model [85]. Although the proposed steady state analysis is in fact, simple it predicts the

amplitude level and frequency positions of resonant peaks of predicted *RCS* response fast and with sufficient accuracy. This very fast and efficient tool is capable to pre-evaluate a suitability of the particular scatterers for implementing in the chipless RFID.

It was confirmed that using this simplified approach that topology modification of original U-folded scatterers or rearrangement of their position in a scatterer array reduces mutual coupling and improves amplitude and frequency stability of its *RCS* response which is crucial for reliable reading of coded information in chipless RFID tags. The issue is in the reading logical zeros represented by removed resonator that is realized by setting very high resistance (1 MΩ). Strong inter-element mutual coupling causes significant distortion of the amplitude level and frequency positions of adjacent resonant peaks of *RCS* curve, see Fig. 4.21. Such behavior makes difficult to read the coded information. This predicts that such elements are not good candidates for chipless RFID scatterers. It is rather recommended to use scatterers with reduced mutual coupling and/or rearrange the scatterers in the array in such a way that frequency adjacent resonators are placed further apart to reduce coupling. This has been proved by analyzing tag composed resonators in the shape of tapered folded dipoles. The taper effectively increases the distance between resonators [78]. The tag with rearranged resonators [82] was analyzed proving again the concept of reducing the mutual coupling to improve the reading reliability.

The 20-bit chipless RFID tag based on the frequency domain detection, consisting of electrically small spiral loaded dipole scatterers was proposed, developed, and verified in section 4.3 [80]. As the dipoles were loaded at the ends by spirals, the footprint size could be reduced to only 11.3 cm^2 (spatial density 1.77 bit/cm^2). It is necessary to note that the reference 20-bit tag [31, 82] was 20.4 cm^2 in size (i.e. spatial density 1.1 bit/cm^2). This significant size reduction was attained while maintaining comparable parameters of the spectral bit density and *RCS* response level. A comprehensive encoding bit capacity of the tag is 120.7 bit/λ^2/GHz, which is the highest value among frequency domain tags compared in [93]. Hence, there is a negligible disadvantage of the proposed tag, consisting in a quasi-monotonous rise of curve interleaving resonant peaks in *RCS* response, ranging from -41.5 dBsm to -30 dBsm. This non-uniformity can be considered a minor obstacle to the tag reading because the response is stable enough for different encoded bit words. Moreover, different logical values of decision threshold *RCS* levels for each resonant peak can be easily computed owing to linear nature of the non-uniformity. The peak-to-valley *RCS* values of novel tag are slightly lower (approx. by 1 to 3 dB) than in the case of U-folded dipole [31] tag employing the rearrangement described in [82]. However, its readability remains sufficient owing to the minimization of mutual coupling, achieved via the asymmetrical layout of the novel scatterer and its rearrangement in the tag.

5 APPLICATION OF SEQUENTIAL BIT READING TECHNIQUE FOR BIT CAPACITY IMPROVEMENT OF A TIME-DOMAIN RFID SYSTEM

Operating principle of the time-domain chipless RFID system described in this chapter was reported in [13, 27]; see the end of section 1.1. Contrary to frequency-domain systems, time-domain approach requires negligible amount of spectrum, which is not proportionally increasing with increasing bit capacity of the tag. Sequential bit reading in near-field of the reader allows high data storage capability, only limited by tag size. The thesis aim, which is addressed in this chapter is to improve already high bit capacity of the system via application of different type of resonator in the tag design. The tag described in section 5.2 achieves 100 bits and data density per unit length, as high as 16.7 bit/cm [95].

The proposed tags are implemented by printing all-identical resonators at equidistant positions forming a linear chain. Coding of bit information is achieved by detuning certain resonant elements by cutting them in the middle. It has been demonstrated that bit information erasing is also possible by simply short-circuiting those previously detuned resonant elements again [28].
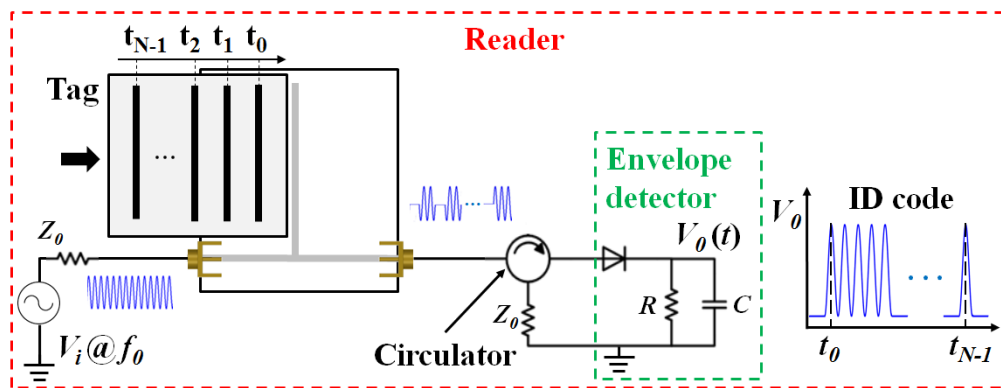

Fig. 5.1: Working principle of the proposed chipless-RFID system. In a reading operation, the tag is displaced at short distance over the reader through a mechanical guiding system providing tag/reader alignment.

The interrogation signal is a harmonic signal at the frequency f_0 of the resonant elements of the tag (or close to it), and tag reading proceeds by displacing the tag over a dedicated transmission line fed by the interrogation signal. Through tag motion, the amplitude of the feeding signal is modulated by the coupling between the line and the functional tag resonators, and the ID code is contained in the envelope function present at the output port of the line (which can be inferred by means of an envelope detector).

66

The system works similar to an amplitude modulator (AM), where the carrier signal is the interrogation signal and modulation is achieved by tag motion (Fig. 5.1). Similar to spectral signature barcodes, the envelope function exhibits dips, or peaks, providing the ID code, but in time domain. For this reason, we can designate these chipless-RFID tags as time-domain signature barcodes. Since the spectral bandwidth is virtually null, it follows that the number of bits is only limited by tag size, proportional to the number of bits.

Although a figure of merit of chipless-RFID tags is usually the data density per area unit, but this tag is based on linear chains of resonant elements, thus the relevant parameter is the number of bits per unit length. The reason is that the shape factor of the tag is extreme, and the number of bits is typically limited by tag length, rather than width. In [13, 27], by using split ring resonators (SRRs), a per-unit-length data density of 3 bits/cm was achieved. In section 5.2, a novel tag (and reader) with much higher density of information per unit length (i.e., 16.7 bit/cm) [95] is reported and validated. The tags are based on straight half-wavelength resonators, and the reader is a 50 Ω transmission line loaded with an open shunt stub.
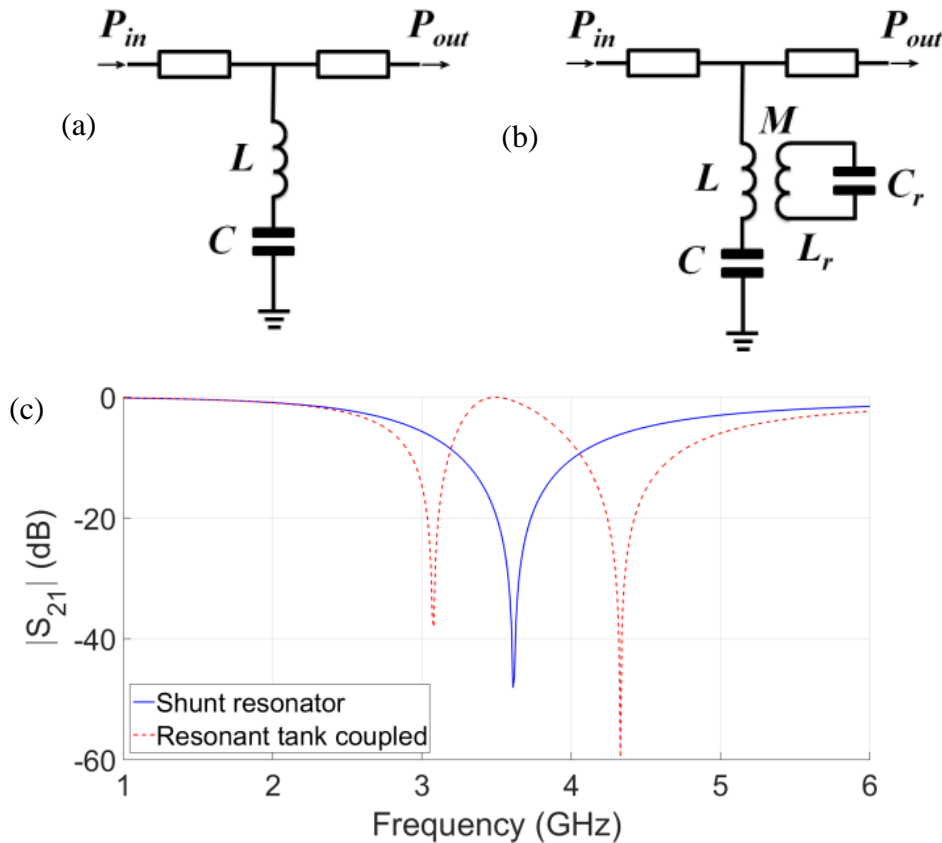

Fig. 5.2: Transmission line loaded with a shunt resonator (a), the same structure with a resonant tank coupled to it (b), and response of both structures inferred from *Keysight ADS* (c). Element values are L = 1.9 nH, C = 1.1 pF, L_R = 1.9 nH, C_R = 1.1 pF and M = 0.6 nH.

67

Let us consider a transmission line loaded with a shunt resonant element (Fig. 5.2a). The frequency response exhibits a single transmission zero, or notch, corresponding to the resonance frequency f_0 of the resonator. However, by coupling a resonant element to the shunt resonator (Fig. 5.2b), the original transmission zero splits into two notches with a frequency separation dependent on the level of coupling (Fig. 5.2c). Thus, at f_0, or in a frequency close to it, the excursion of the transmission coefficient is significant, and this effect can be useful for coding purposes. As the resonant element of the reader, an open shunt stub was chosen and as the resonant element of the tag, a linear half-wavelength resonator was chosen. Each of them represents one bit. Zero bit is coded by cutting the resonator in the middle; see Fig. 5.3.
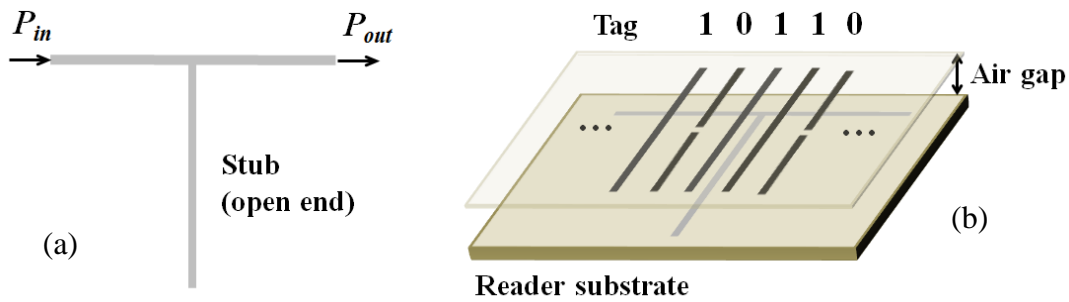
Fig. 5.3: Layout of the active part of the reader (a). Reader and fragment of the tag (b) with an example of coding '0' by detuning a strip (cut in the middle).

5.1 SYSTEM BASED ON THE FIRST RESONANCE OF THE READER STUB

The active part of the reader (stub-loaded line) was designed in microstrip technology by loading a 50 Ω line with an open shunt stub exhibiting its first transmission zero at f_{01} = 3.64 GHz. The considered substrate is Rogers RO3010 with dielectric constant ε_r = 10.2 and thickness h = 0.64 mm. The width of the 50 Ω line is 0.6 mm, whereas the width of the stub is 0.4 mm, corresponding to a characteristic impedance of 60 Ω. The layout of the active part of the reader is shown in Fig. 5.3a. The length of the stub is 8 mm. The layout of the fragment of a tag with an example of '0' bit coding by detuning (cutting) one resonator is depicted in Fig. 5.3b. The length of the half-wavelength resonators is 30 mm and their period is 2 mm. Frequency response of the reader is depicted in Fig. 5.4. The half-wavelength resonators of the tag has been designed to be implemented on the Rogers RO4003C substrate with dielectric constant ε_r = 3.55 and thickness h = 0.2 mm. Resonant element width is 0.4 mm, which is of interest to maximize the per unit length information density of the tag (where the resonant elements are disposed orthogonal to the tag chain axis). The frequency response of the reader and only one half-wavelength resonator on top of it, at different

68

relative positions, is also depicted in Fig. 5.4. It can be seen maximum splitting occurs when the half-wavelength resonator is perfectly aligned with the stub ($d = 0$ mm). The same effect can be explained using coupled resonant circuits theory Fig. 5.2.
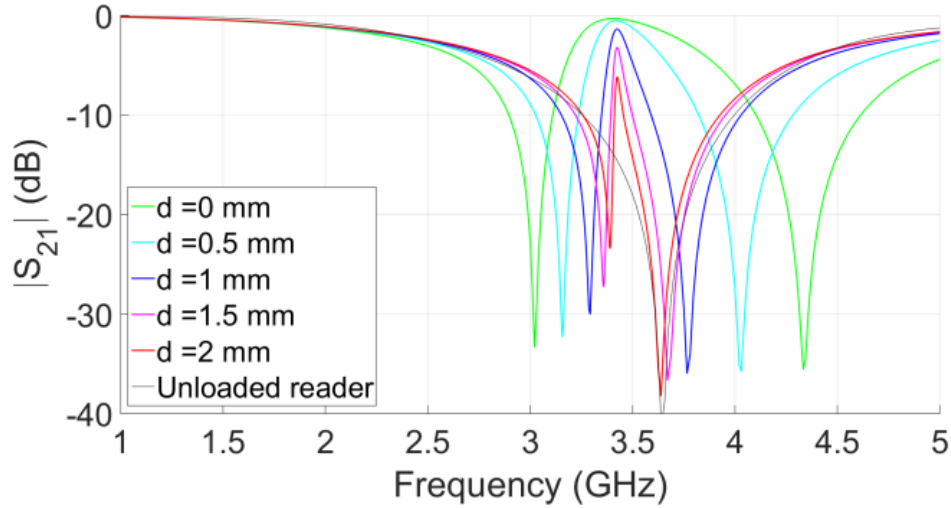

Fig. 5.4: Frequency response (S_{21}) of the unloaded reader, and reader loaded with a half-wavelength resonator placed at different positions. The vertical distance (air gap) between the reader and the tag is 0.3 mm.
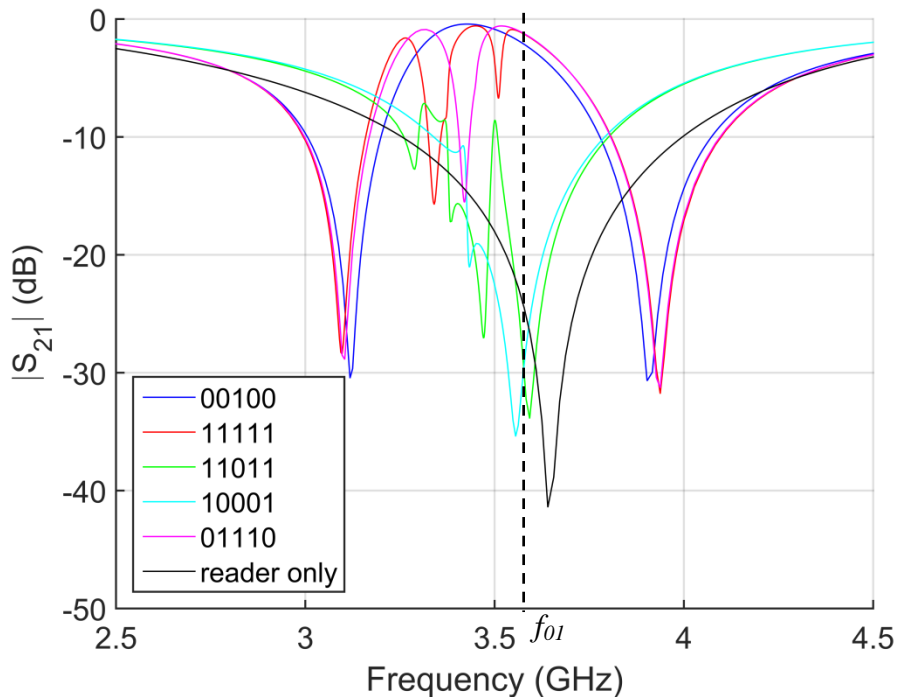

Fig. 5.5: The first version of the system, frequency response for different bit words.

Simulation results of transmission coefficient $|S_{21}|$ for different 5-bit words are depicted in Fig. 5.5. Middle strip (bit) is read (i.e. perfectly aligned with the reader stub) in all these cases (red and magenta are '1', green and cyan are '0'). Multiple coupling

69

between tag strips causes parasitic dips, which are dependent on particular bit word. Considering this effect reading frequency f_{01} was set out of parasitic dips band to 3.64 GHz, which provides slightly less $|S_{21}|$ than frequency of the single strip peak value (blue line).

Frequency positions of all resonant dips are also dependent on an air gap width between the tag and the reader substrates, which have an influence on effective dielectric constant of the whole system. Stability of the air gap width is dependent on mechanical qualities of the tag guiding system of the reader. Although the presented system operates reliably for designed air gap width of 0.3 mm, there could be a reading error if its variation exceeds for more than ± 0.1 mm, because of the frequency distance between the parasitic dip minimum and f_{01} is only circa 100 MHz; see Fig. 5.5. The distance between tag dipoles is 1.6 mm in order to keep parasitic dips insignificant at the cost of lower per-unit-length bit density. These issues are solved by employing the second resonance of the reader stub; see section 5.2.
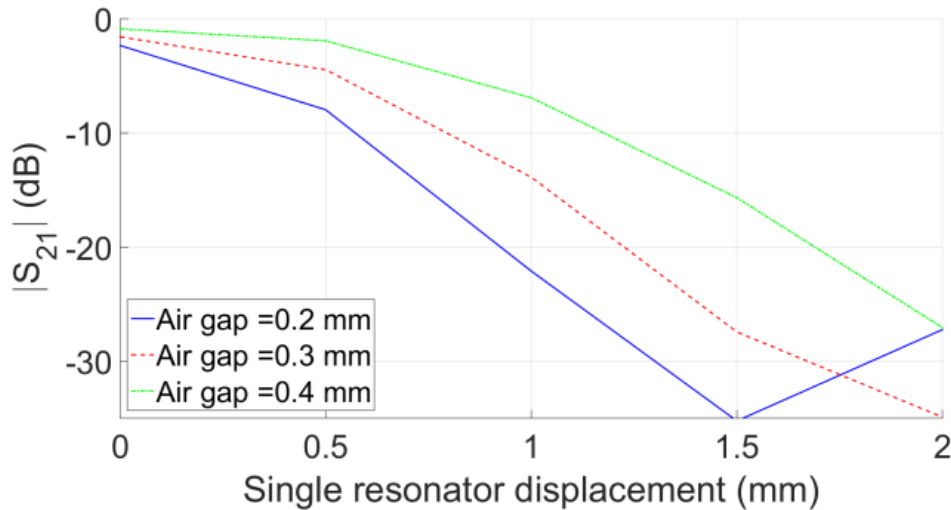

Fig. 5.6: Transmission coefficient at f_{01} for different relative displacements between the resonant element of the tag and the stub. Different width of an air gaps is considered.

The variation of the transmission coefficient at f_{01} for the different relative displacements d between the tag resonator and the open stub is depicted in Fig. 5.6, where it can be appreciated that a significant excursion of the transmission coefficient results, as required for reading purposes.

Since it is difficult to ensure a uniform air gap during reading operation of the real system, it is important to analyze the effects of the air gap variation on the transmission coefficient at f_{01} when the half-wavelength resonator is displaced over the stub. The results, also depicted in Fig. 5.6, indicate that certain air gap variation with regards to

the nominal value (0.3 mm), compatible with a significant excursion in the transmission coefficient, is still acceptable.

Let us now consider the presence of various half-wavelength resonators in the tag, corresponding to several bits. In order to avoid multiple couplings, the tag period has been set to 2 mm (corresponding to a per-unit length data density of 5 bit/cm). Nevertheless, such period is significantly smaller than the period of the tags reported in [13, 27] (note that the interrogation signal is tuned to a frequency, which is similar to f_{01}). The excursion of the transmission coefficient at f_{01} when the 40-bit tag with all-functional bits (i.e., with all bits set to '1') is displaced over the stub is depicted in Fig. 5.7 (the displacement has been restricted to nine resonators, or bits). Other bit combinations, achieved by resonator detuning (providing a cut in the central position, see Fig. 5.3b), are also depicted in Fig. 5.7. In view of such figure, the tags can be correctly read. Note that, contrary to previous works based on this near-field chipless-RFID approach (but using different tags and reader), negative logic is used, i.e., the dips in the transmission coefficient correspond to the logic state '0', whereas the logic '1' (functional resonator on top of the stub) provide roughly total transmission.
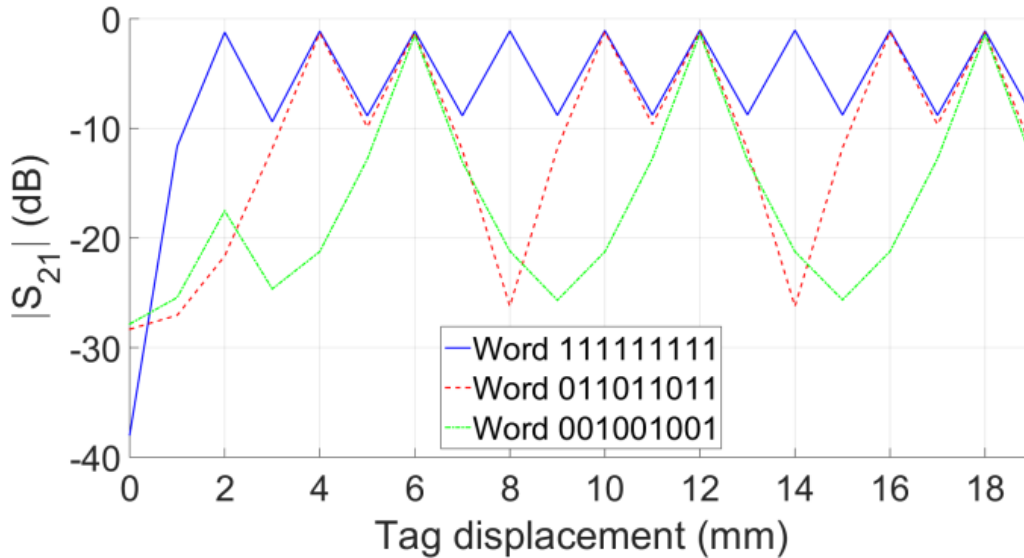

Fig. 5.7: Transmission coefficient at f_{01} as a result of displacing the tag over the reader, for various bit combinations (indicated).

A 40-bit tag with all-functional resonators and the reader have been fabricated by means of a standard photo-etching and a *LPKF H-100* drilling machine, respectively (Fig. 5.8). Then the tag has been read by means of a set-up similar to the one used in [13], that uses a function generator (to generate the interrogation signal), an envelope detector preceded by an isolator (to obtain the envelope function), and an oscilloscope (to display the results). The forty peaks in the time-domain response (Fig. 5.9) indicate that all resonators are functional (all bits set to '1'). However, when certain resonant

elements are detuned ('0') by cutting them, then the corresponding peak disappears, as Fig. 5.9 illustrates. Therefore, the functionality of this new near-field chipless-RFID system is validated.

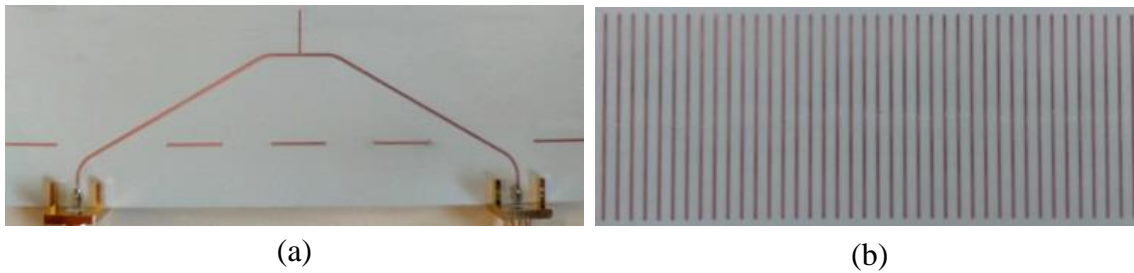(a)   (b)
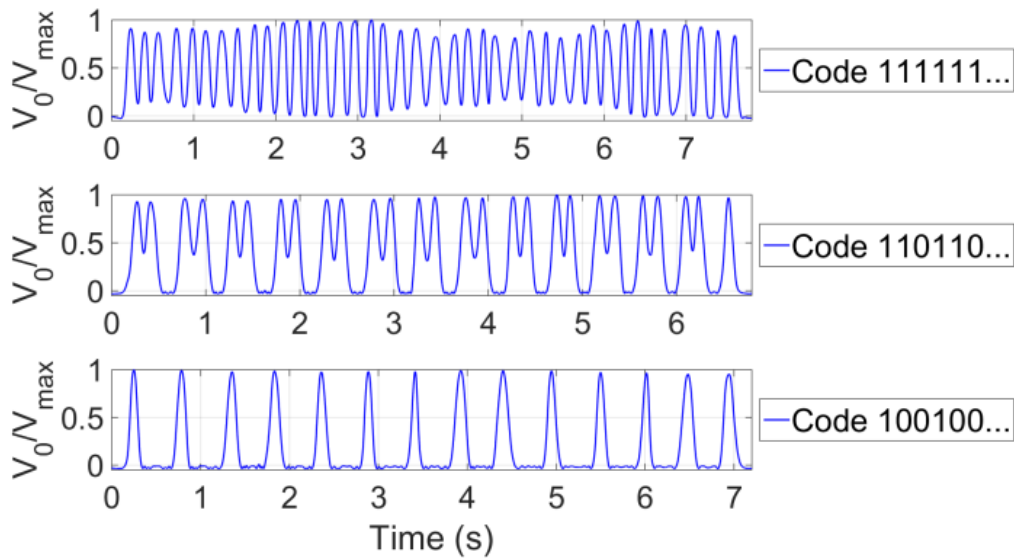
Fig. 5.8: Photograph of the reader (a) and the tag (b).

Fig. 5.9: Envelope function for various bit combinations of the tag.

5.2 SYSTEM BASED ON THE SECOND RESONANCE OF THE READER STUB

The active part of the reader is a stub-loaded microstrip line, implemented on the Rogers RO3010 substrate with thickness $h = 0.635$ mm and dielectric constant $\varepsilon_r = 10.2$. The length and width of the stub are 26 mm and 0.2 mm, respectively. The width of the transmission line is 0.6 mm (50 Ω line); see the layout in Fig. 5.3a. This structure exhibits a stop band response, with transmission zeros at the frequency where the electrical length of the open stub is 90º and at its odd harmonics (Fig. 5.10). The 3D view of the loaded reader with one of the half-wavelength resonators of the tag aligned with the reader stub can be seen in Fig. 5.3b. The separation between adjacent resonators in the tag chain is 0.2 mm and resonator dimensions are 34 mm × 0.4 mm (so

that the tag period is 0.6 mm). The tag chain has been implemented on the Rogers RO4003C substrate with thickness $h = 0.2$ mm and dielectric constant $\varepsilon_r = 3.55$.

By locating straight half-wavelength resonator on top of the stub, as Fig. 5.3b illustrates, the response of the structure is modified as depicted in Fig. 5.10, where two transmission zeros in the vicinity of the fundamental (first) resonance of the stub-loaded line appear (frequency splitting). Note that the half wavelength resonator can be tuned to operate at different frequencies, not necessarily at the fundamental frequency of the stub-loaded line. The response for the half-wavelength resonator tuned to the second resonance is also included in Fig. 5.10. It can be seen it is possible to achieve frequency splitting in the vicinity of any of the stub resonances. For the loaded reader, two different cases have been considered with regards to the half-wavelength resonator, i.e., either tuned at the first (described in previous section 5.1) or second resonance of the stub. The considered air gap is 0.3 mm. These results have been inferred by electromagnetic simulation, using *Keysight Momentum*.
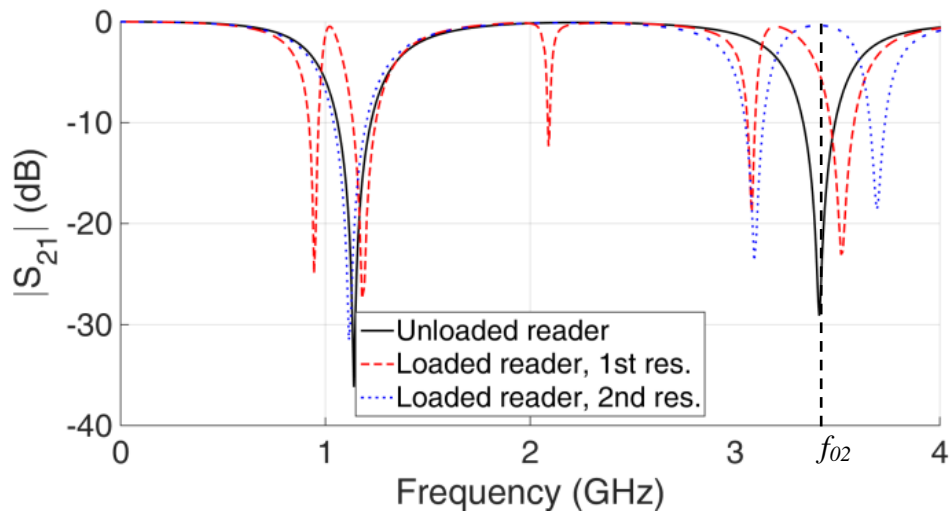

Fig. 5.10: Magnitude of the transmission coefficient (S_{21}) of the unloaded reader and reader loaded with a single half-wavelength resonator perfectly aligned.

In addition to the main split of the original transmission zero of the reader stub, which is used to bit encoding (Fig. 5.2), there are parasitic dips caused by multiple couplings between the stub and the tag half-wavelength resonant elements. Depths and frequency positions of these dips depend on a particular bit word and variation of an air gap width between the tag and the reader substrates, as it was explained in section 5.1. Substantial parasitic dips in a band of the stub first resonance dip were reduced at the expense of losing per-unit-length bit density by increased spacing between resonators of the tag; see Fig. 5.5.

A version utilizing the second resonance was designed in order to solve this problem. In this case, parasitic dips are situated completely out of the stub second

73

resonance dip band; see Fig. 5.11 (black line). Reading frequency $f_{02} = 3.47$ GHz was set as a compromise between the bit word containing a single '0' and the word with three '0' in a row between '1' bits (green and cyan line respectively). The absence of parasitic dips proximity to f_{02} provides more than 3 times higher per unit length bit capacity with slightly better dynamic range and comparable robustness against reader to the tag air gap width fluctuation than the version based on the first resonance of the reader stub.
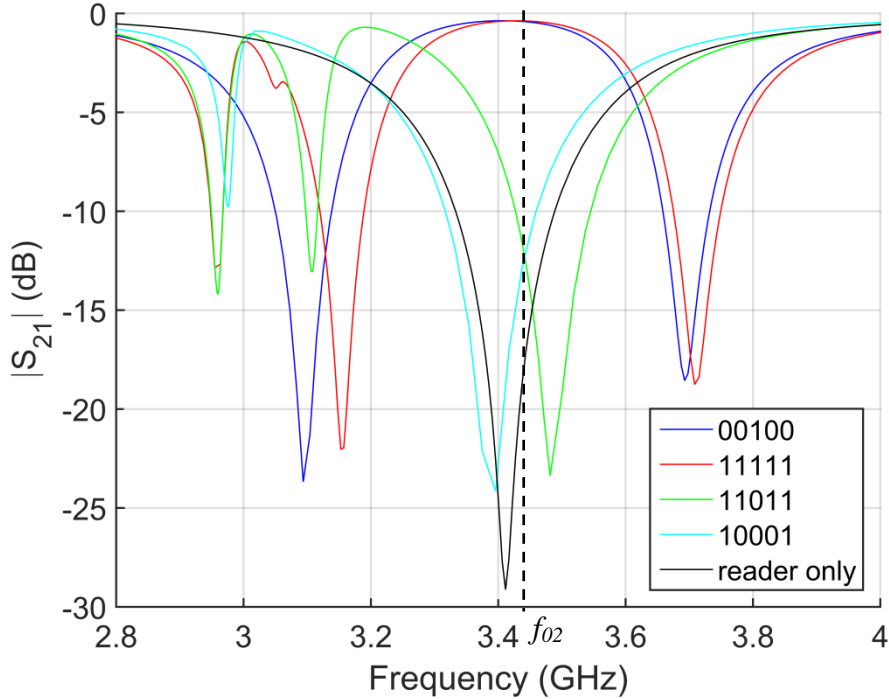
Fig. 5.11: Second version of the system, frequency response for a different bit words.

Fig. 5.12 depicts the variation of the transmission coefficient at the frequency of the interrogation signal, set to f_{02}, as a 7-bit tag is displaced above the reader. Two different bit combinations, indicated in the figure, have been considered, in order to validate, at simulation level, the proposed system. An important aspect is the robustness against air gap variations. Therefore, we have repeated the simulations of the considered 7-bit tags for air gaps of 0.2 mm and 0.4 mm (the nominal air gap being 0.3 mm). The corresponding responses are also included in Fig. 5.12, and it can be appreciated that differences with the air gap variation arise. These differences are caused by frequency shift of the second resonance of the stub as a result of the air gap variation, and are mainly manifested by a different level of the transmission coefficient when a detuned resonator is on top of the reader stub. Nevertheless, for all bit combinations, the responses exhibit the expected behavior. Namely, for a logic state '1', corresponding to the presence of a functional resonator on top of the stub, maximum transmission is achieved; conversely, when the half-wavelength resonator is detuned (i.e., not

functional) by cutting it, corresponding to the logic state '0', the transmission coefficient is severely reduced. Note, therefore, that, as compared to papers [13, 27], a negative logic is utilized in this paper.
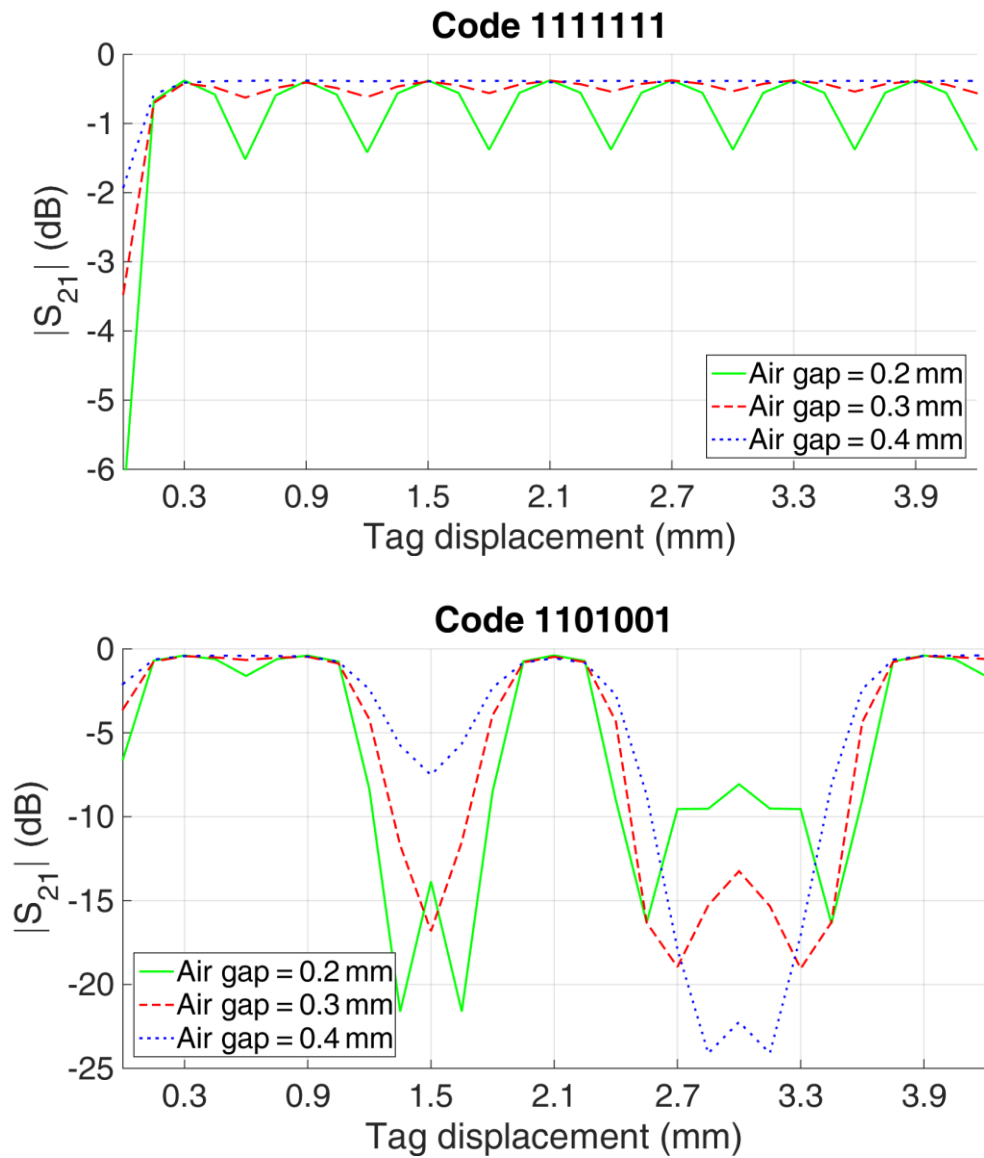

Fig. 5.12: Variation of the transmission coefficient at the interrogation signal frequency that results from a relative displacement between the tag and the reader for the indicated codes. Several widths of the air gaps are considered.
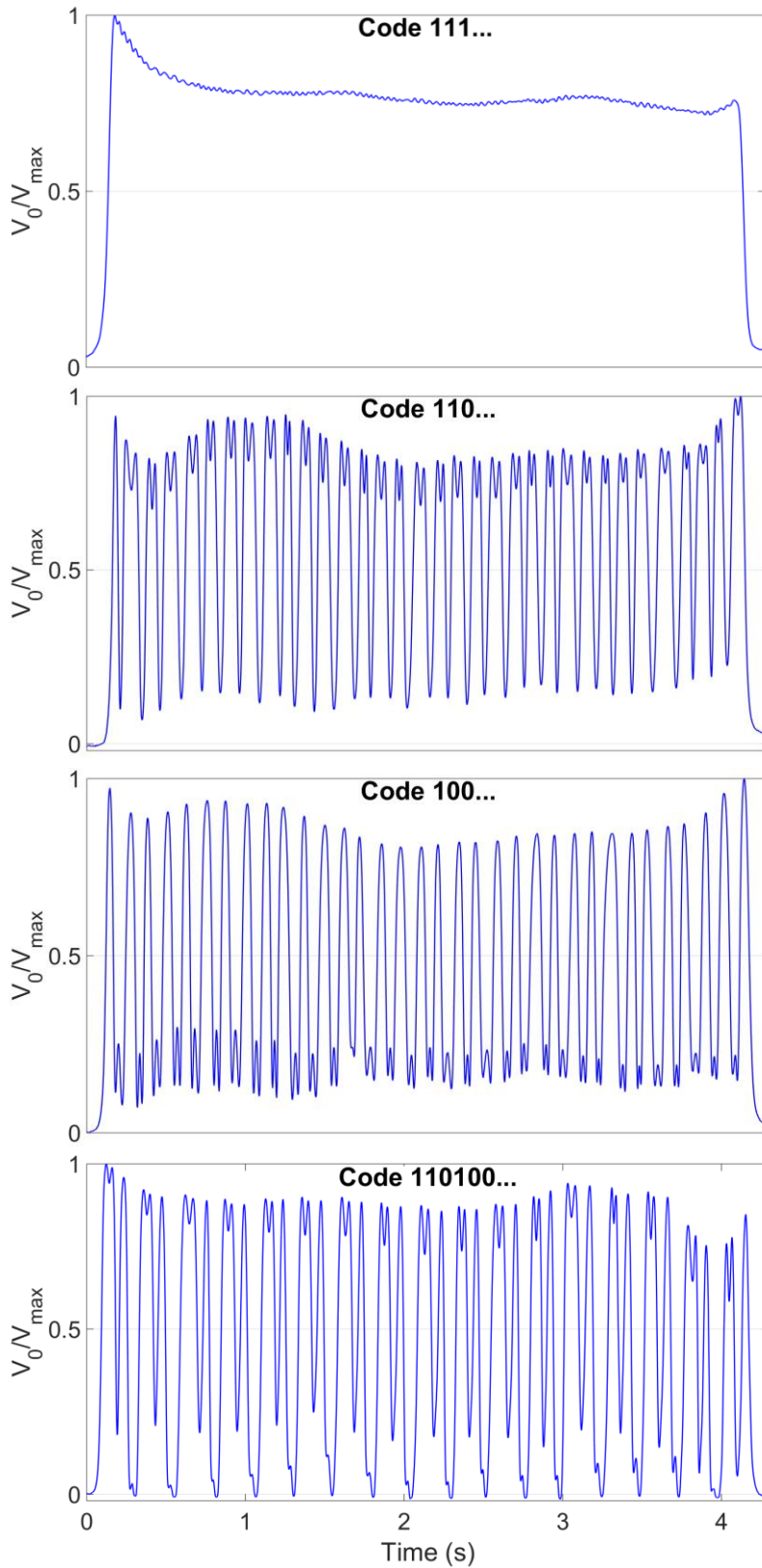
Fig. 5.13: Measured normalized envelope for the 100-bit tags with the indicated codes. For each code, the repeating period is shown. The reason of the variation of the maximum voltage in the figures is related to the fact that absolute uniformity in the gap space between the tag and the reader cannot be guaranteed.

To experimentally validate the proposed system, we have fabricated a 100-bit tag by means of standard photo-etching, where all-functional resonators have been etched. Conversely, the reader has been fabricated by means of a *LPKF HF-100* drilling machine (the photographs are depicted in Fig. 5.13). We have then read this tag by means of the set-up present in our laboratory, described in [13], consisting of a function generator, an envelope detector and an oscilloscope (to display the time domain response of the tag, i.e., the AM signal containing the ID code), plus the mechanical guiding system. The measured envelope is depicted in Fig. 5.13, where it can be seen that dips are not present, as long as all bits are set to '1'. Then we have detuned some resonant elements by cutting them (hence setting some bits to '0'), and the measured normalized envelope reveals the presence of such '0' states (as dips in the time-domain responses). Thus, tag programming can be simply done by cutting the required resonant elements, similar to [13, 28]. Note that three codes have been programmed, as it is visible in Fig. 5.13, and in all the cases such codes have been correctly read.

The achieved surface information density of the tag is 4.9 bit/cm^2 which is not as good as the one reported in [13, 27], i.e., 8.9 bit/cm^2. But 100 bits, were accommodated in a length of 60 mm, corresponding to a per-unit-length density of 16.7 bit/cm, i.e., substantially larger than the one of previous similar works based on tags implemented with split ring resonators [13, 27]. Such high per-unit-length information density has been achieved by driving the separation of the resonant elements of the tag to the limit of the available technology (0.2 mm). Further reducing this spacing may have negative effect on tag readability due to possible couplings between the line stub (reader) and adjacent resonators in the tag. Coupling effect has been found to be negligible for spacing considered in this work. It should be also pointed out that it is possible to reduce the width of the tag (in order to increase the data density per surface) by increasing the frequency of the interrogation signal. In such case, both the reader stub and the resonant elements of the tag can be shortened.

Finally, concerning the substrate of the tag and its fabrication, chemical etching of a laminated microwave substrate Rogers RO4003C (thickness $h = 0.2$ mm and $\varepsilon_r = 3.55$) has been considered (mainly focused on demonstrating the potential of this new approach to enhance the density of bits per unit length). Nevertheless, it was demonstrated in [27, 28] that by replacing such tag substrates and fabrication procedure with a flexible substrate, such as paper, and inkjet printing, the functionality of the tags is preserved. Rather than the quality factor of the resonant elements, the key aspect for system functionality is the effect of coupling between the sensitive part of the reader (the stub in our case) and the resonant element of the tag. Such coupling does not depend critically on the substrate material of the tag, and for that reason the functionality is preserved in [27, 28]. It should be pointed out, however, that the quality

factor of the resonant elements may have influence on the effects of neighbor resonators, if its value is too low. Nevertheless, under these circumstances, the solution is to simply increase the distance between adjacent resonators. According to the period of the reported tags (0.6 mm), there is a margin to proceed in that way (if necessary, depending on the considered substrate), yet keeping a significant density of bits per unit length.

5.3 SUMMARY

The functionality of a time-domain near-field chipless RFID system with sequential bit reading has been demonstrated. The tag was implemented as a chain of linear (straight) half-wavelength resonators (planar dipole) and the reader as a stub-loaded microstrip line. The first version of the system operating on the first resonance of the reader stub achieved per-unit-length bit density 5 bit/cm; see section 5.1 [96]. A bit density and reading reliability are both limited. The former one because of the parasitic resonance dips caused by mutual coupling between neighboring tag dipoles and the later due to transmission coefficient dependence on the width variation of an air gap between the reader and the tag.

This issue was solved by employing the second resonance of the reader stub; see section5.2 [95]. The 100-bit tags and the reader were designed for operation at frequency f_{02} = 3.47 GHz. Moreover, the achieved information density per area and length (the most important one in this type of tags based on a resonator chain) is 4.9 bit/cm^2 and 16.7 bit/cm, respectively. By using the proposed system, the shape factor of the tags has been severely improved as compared to those of previous tags based on a sequential bit reading.

6 THE TAGS WITH A HIGH OVERALL RCS RESPONSE CONTAINING RESONANT DIPS

The read distance in specific chipless RFID applications may be limited due to the low *RCS* of their tags. Therefore, *RCS* responses of the tags presented in chapter 4, which are at the level around -35 dBsm, can be insufficient from this point of view. Chipless RFID tags that offers a higher *RCS* at the level around -15 dBsm are proposed in this chapter [93, 97]. These tags are based on scattering from larger planar objects, such as wideband slotted or notched dipoles or rectangular plates with high *RCS*. Bit information is coded by means of resonant dips caused in the *RCS* response by either embedded or closely spaced additional resonators.

The first tag is based on a uniplanar structure where coplanar slots are used as resonators and etched in a metallic rectangular plate; see section 6.1 [77, 97]. Coplanar slots shorted at the one end are a complementary resonator of U-folded dipole presented in subsection 4.1.1. The second tag is composed of a metallic rectangular plate and an array of detuned dipoles used as resonant elements closely coupled to it; see section 6.2 [93, 98].

6.1 THE TAG USING A METAL PLATE WITH U-SLOTS

The proposed tag is based on a complementary structure, which consists in coplanar slots introduced in a continual metallic layer, unlike the strip-based scatterers presented e.g. in [31, 50]. This pattern then exhibits a generally larger and typically monotone *RCS* curve over a selected frequency interval, with dips corresponding to the resonances of individual slots; [64]. The mutual coupling between particular resonators was reduced by rearranging scatterers in the same manner as in subsection 4.1.1. The new tag response considerably improves the frequency and amplitude robustness of *RCS* response without the mean-value of *RCS* level being decreased. Thereby the reliability of reading the coded information is significantly enhanced.
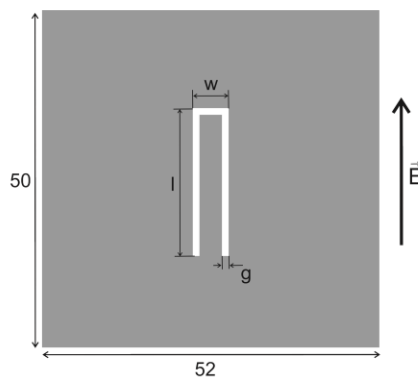

Fig. 6.1: A single coplanar slot embedded into the rectangle 52×50 mm^2 in size.

The tag is based on a metallic rectangular plate 52×50 mm^2 in size chosen to provide a monotonous *RCS* curve over a frequency range of 2 to 4 GHz; [52]. The shorted coplanar slot forming an inverted letter "U" is introduced symmetrically into the rectangle so that the slot is collinear with the unit polarization vector of the incident field. Vertical polarization of the incident wave excites the electric field in the narrow shorted part of the slot; see Fig. 6.1.

A brief parametric study of geometry of a single resonator in the plate is presented in Fig. 6.2. It can be observed that the peak depth can be increased by the resonator width *w* or gap width *g* increasing. It follows that a trade-off between the peak depth and resonator size (bit capacity of the transponder) needs to be found.

(a)

(b)
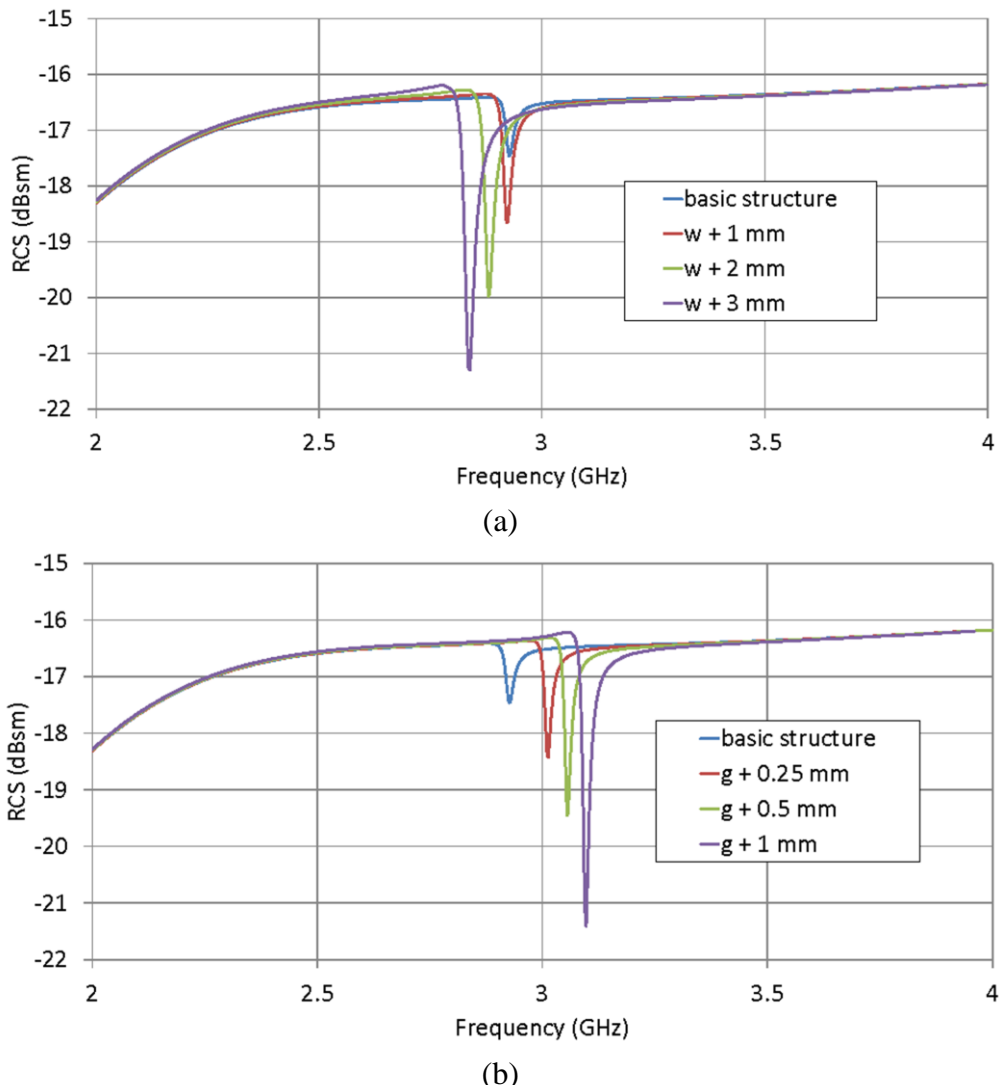
Fig. 6.2: Parametric analysis of simulated RCS response of one resonator with resonator width *w* as a parameter (a) and resonator gap *g* as a parameter (b).

The 20-bits tag was designed by adding 20 shorted coplanar slots of different length into the metallic rectangular plate 52×50 mm^2 in size; see Fig. 6.3. The slot-arm length l ranges from 15.0 to 24.5 mm, with 0.5 mm length difference between the two neighboring slot couple. The slot gap is $g = 0.25$ mm and the width of the shorting slot is 2 mm, so that the metallic gap between the two adjacent slot-arms is 1.5 mm. The coplanar slots in an array are equidistant from each other, at a distance equal to 0.5 mm. The binary information is encoded into the slot array by presence of the slot represents a notch in the *RCS* curve, and absence (or shorting) of the slot represents a smooth *RCS* curve. A 20-element coplanar slot array with the 6th and 18th slots missing thus presents the 20-bit word '11111011111111111011'; see Fig. 6.3b.

In the basic arrangement with sequent situated resonators see Fig. 6.3a - Fig. 6.3c, we can observed relatively strong mutual coupling of the neighbouring resonators, which can lead to the frequency shift of particular peaks in the *RCS* response; see Fig. 6.4a. As it can be seen in Fig. 6.4b, this phenomenon cannot be eliminated even by coding of the zero bits by shorting; see Fig. 6.3c.
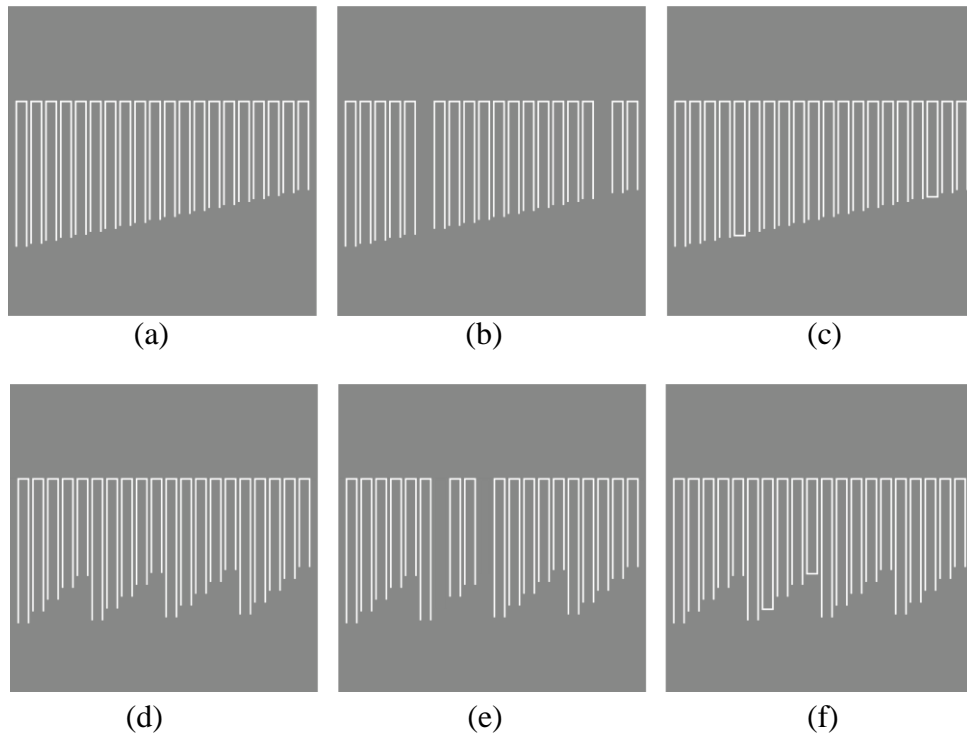

(a)	(b)	(c)
(d)	(e)	(f)

Fig. 6.3: Original arrangement of the slots in the rectangle representing the 20-bit words '11111111111111111111' (a) and '11111011111111111011' coded by removing (b) and shorting (c). Modified arrangement of the slots in the rectangle in descending order according to their length, representing the 20-bit words '11111111111111111111' (d) and '11111011111111111011' coded by removing (e) and shorting (f).

However, this phenomenon can be minimised by the resonators rearrangement that each fourth resonator is moved to the corresponding quarter of the array so that the original ascending order according to their length '1 2 3 4 5 6 7... 20' is modified to '1 5 9 .. 2 6 10 .. 3 7 11 .. 4 8 12 16 20'; see Fig. 6.3d. The same rearrangement was also applied for mutual coupling reduction in case of U-shaped dipole; see subsection 4.1.1.
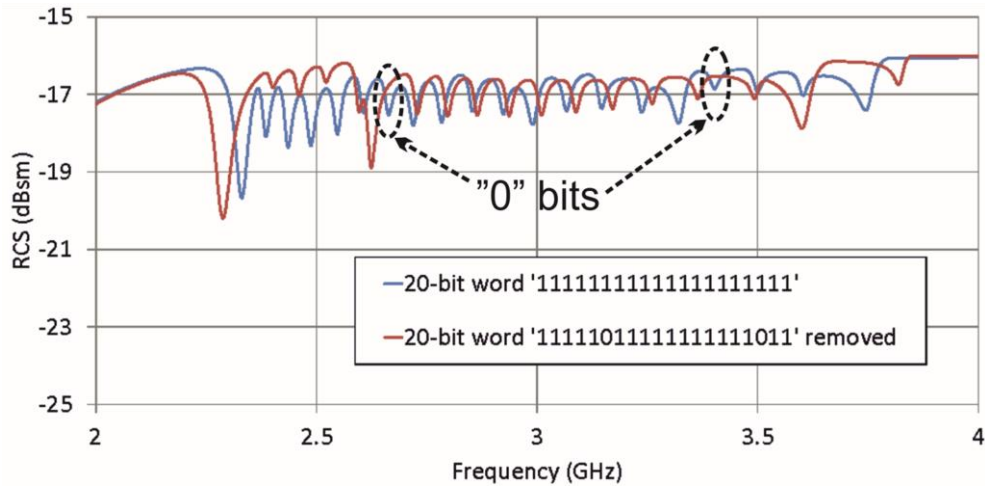
(a)
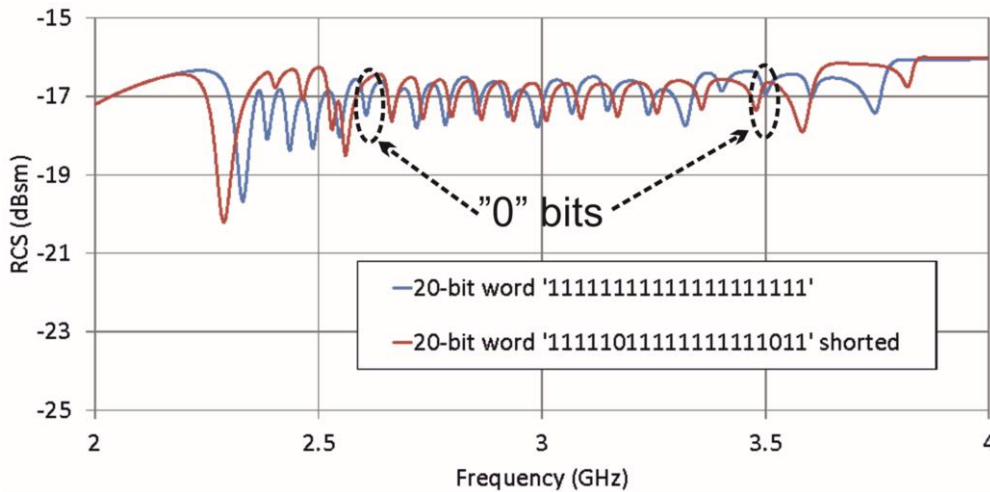
(b)

Fig. 6.4: Simulated *RCS* response of 20-element coplanar slot array with sequent arrangement of inter-elements representing comparison of a bit words '11111111111111111111' and '11111011111111110111' for (a) encoding by resonator removing and (b) encoding by resonator shorting.

It can be observed that the greater the distance, the smaller is the mutual coupling of originally neighboring resonators, and the smaller is the frequency shift of the neighboring resonance if '0' bit is applied; see Fig. 6.5. Coding of the zero bits by shorting doesn't offered next improving of the frequency stability; see Fig. 6.5b.

The monostatic measurement of tag *RCS* response was performed in an anechoic chamber in order to verify the simulated results; see subsection 4.4 for the description of the measurement method. The distance between the double ridge horn antenna DRH20 [86] and a measured tag was 250 mm. The rectangular metal plate used as a reference scatterer was 50×52 mm^2 in size (corresponding with the measured tags) and 0.3 mm in thickness. The measured data are smoothed to suppress the noise caused by a number of residual reflections.

Fig. 6.6 illustrates the measured *RCS* response of two variants of scatteres arrangement in 20-bit chipless RFID tags, i.e. with sequent arrangement and with re-arrangement of inter-elements representing comparison of bit words '11111111111111111111' and '11111011111111111011' for encoding by resonator removal. Significant improvement consisted in inter-element mutual coupling minimisation and frequency stability of the peaks can be observed.
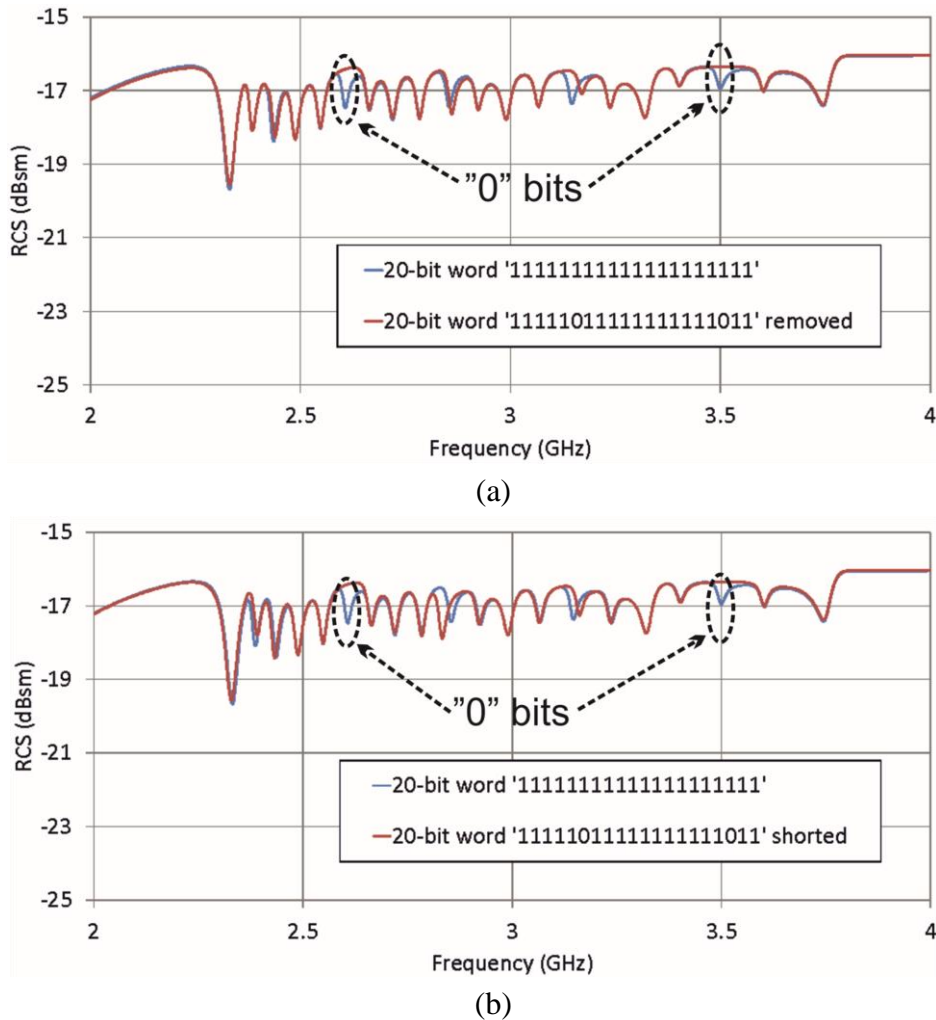

(a)

(b)

Fig. 6.5: Simulated *RCS* response of 20-element coplanar slot array with rearrangement of inter-elements representing comparison of a bit words '11111111111111111111' and '11111011111111110111' for (a) encoding by resonator removing and (b) encoding by resonator shorting.
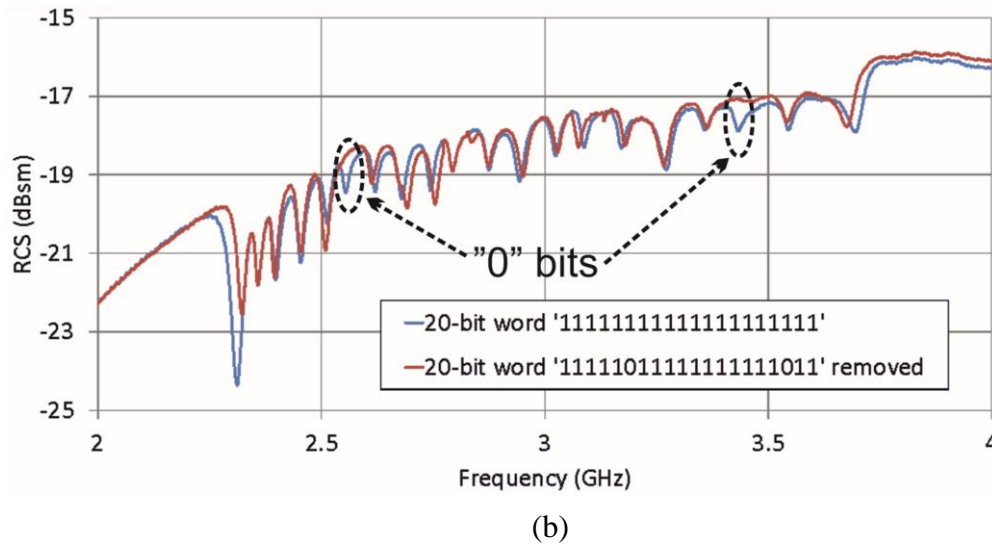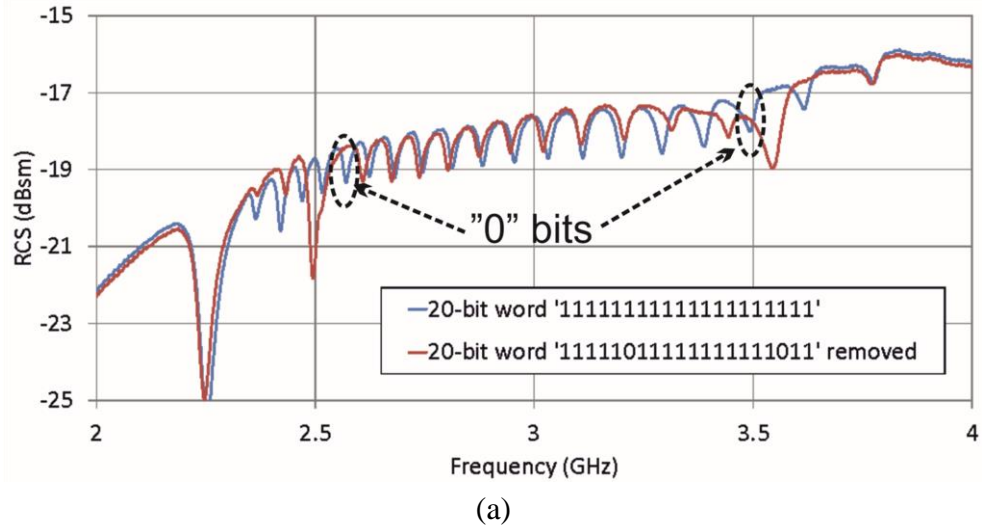
Fig. 6.6: Measured *RCS* response of 20-element coplanar slot array with sequent arrangement (a) and with re-arrangement of inter-elements (b) representing comparison of bit words '11111111111111111111' and '11111011111111111011' for encoding by resonator removal.

6.2 THE PLATFORM TOLERANT TAG USING DIPOLES OVER A METAL PLATE

The introduced chipless RFID transponder is based on an array of detuned dipoles used as scatterer elements closely coupled to a metallic plate [93, 98]. An analytical approach was applied in order to study the quality factors, absorption properties and reflection coefficients of a single dipole-plate scatterer placed above a grounded dielectric layer and illuminated by an incident TEM plane wave. The said approach is based on coupled mode theory [99], originally introduced for general resonator terminating waveguides or optical modes, and further applied for analyses of reflect-

array elements [100]. The motivation is to find the optimum scatterer size and its height above the plate to ensure sufficiently deep resonant minima in the *RCS* response. Moreover, we extensively evaluate the platform tolerance of electrical parameters when tags are attached to various packaging materials, such as cardboard, plastic, wood, metal or a human body phantom. The proposed concept embodies a relatively high *RCS* response level (about -15 dBsm) and a satisfactory resonance drop depth ($2 - 5$ dB) of individual removed scatterers (coding zero bits). Compared to the known solutions, the high spectral bit capacity (>15 bit/GHz) together with good performance immunity when situated in close proximity to dielectric and metallic objects represent significant advantages of the presented solution. Very good robustness in the frequency and amplitude stability of the *RCS* response in the case where zero-bit words are coded, can be considered as an essential benefit for reliable reading. On the other hand, the double layer substrate represents an inherent property and also a disadvantage of the presented structure, which nevertheless might be acceptable in specific applications.

6.2.1 THEORETICAL ANALYSIS

In contrast to common antenna applications, in frequency-domain chipless RFID, it is preferable to have the frequency bandwidth of each single tag element as narrow as possible, *i.e.* a high-quality factor of the element with sufficient value of *RCS* is required. Both key properties are met in the case of the dipole-array closely coupled to a finite-sized metallic plate, thereby creating a dipole array-plate scatterer [94]; see Fig. 6.7.
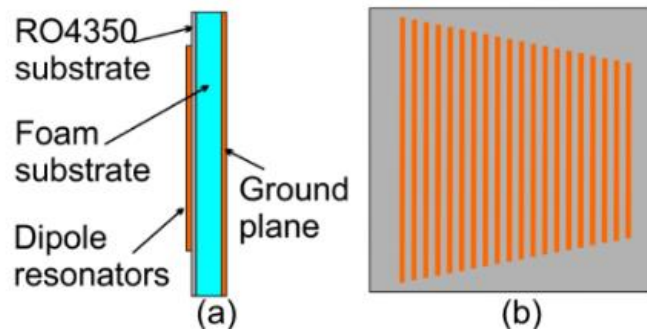

Fig. 6.7: Cross-section (a) and top view of investigated 20-bit chipless RFID transponder formed by 20 detuned dipoles placed above a metallic plate.

The image principle can be used to simply explain why the quality factor significantly increases at dipole resonant frequencies. The original dipole and image ground plane currents show approximately the same amplitude, yet they possess opposite phases [94] and therefore the field distribution supports energy storage, which increases the value of the quality factor [101-104].

One of the single dipole-plate scatterers from Fig. 6.7, excited by an incident plane wave, forms a resonant cavity, which is considered to couple to a TM$_{01}$ patch mode (exhibiting conductive and dielectric dissipation losses inside the cavity), and a radiation mode (through which the energy leaks into the form of a propagating wave). According to the theory [94], such a resonator might be treated as a one port device exhibiting a reflection coefficient at the interface of the resonator and the external waveguide/outside space (*i.e.* at the patch surface reference plane). This can be expressed in the following way:

$$\Gamma(f) = \frac{\dfrac{1}{Q_r} - \dfrac{1}{Q_0} - \dfrac{2j(f - f_r)}{f_r}}{\dfrac{1}{Q_r} + \dfrac{1}{Q_0} + \dfrac{2j(f - f_r)}{f_r}}, \tag{6.1}$$

where Q_r is the radiation, *i.e.* external, quality factor, Q_0 represents the unloaded quality factor of the patch cavity, and f_r is the resonant frequency. The CAD formula for the space wave radiation quality factor was derived by Jackson [105] (chapter 7) as:

$$Q_r = \frac{3}{16} \frac{\varepsilon_r}{p c_1} \frac{L_{\text{eff}}}{W_{\text{eff}}} \frac{\lambda_0}{h}, \tag{6.2}$$

where ε_r is relative permittivity and p is the ratio of power radiated into space by the patch to the power radiated into space by the equivalent dipole (that has the same dipole moment as the patch). In addition, c_1 is a substrate material dependent constant, L_{eff}, and W_{eff} represent respectively the effective length and width of the patch, λ_0 represents the free space wavelength, and h is the dipole height above the metallic plate.

$$p = 1 + \frac{a_2}{10} \left(k W_{eff}\right)^2 + \frac{3}{560} \left(a_2^2 + 2a_4\right) \left(k W_{eff}\right)^4 + \frac{1}{5} c_2 \left(k L_{eff}\right)^2$$
$$+ \frac{1}{70} \left(k W_{eff}\right)^2 \left(k L_{eff}\right)^2, \tag{6.3}$$

where k is the free space wave constant, $a_2 = -0,16605$, $a_4 = 0,00761$, $c_2 = -0,0914153$,

$$c_1 = \frac{1}{n^2} + \frac{2}{5n^4}, \tag{6.4}$$

and $n = \sqrt{\mu_r \varepsilon_r}$ is the index of refraction of the substrate. The unloaded quality factor Q_0 comprises both conductor and dielectric losses of the patch cavity and is given by [94]

$$Q_0 = \frac{Q_c Q_d}{Q_c + Q_d} \tag{6.5}$$

$$Q_c = h\sqrt{\frac{\omega}{2}\mu\sigma} \tag{6.6}$$

$$Q_d = \frac{1}{tan\delta} \tag{6.7}$$

where ω is the angular frequency, μ represents the permeability, σ is the conductivity of the metal plates forming the top and bottom cavity walls, and $\tan\delta$ is the loss tangent of the dielectric. The total (*i.e.* loaded) quality factor Q_t of the cavity comprising all loss phenomena except for the effect of surface waves, which have been found to be negligible (namely by three orders of magnitude lower for the considered air and foam substrates with thicknesses of up to 3 mm) is computed as:

$$\frac{1}{Q_t} = \frac{1}{Q_r} + \frac{1}{Q_c} + \frac{1}{Q_d}. \tag{6.8}$$

The reflection coefficient at the resonant frequency is derived from (6.16.16.1) as

$$\Gamma(f_r) = \frac{\dfrac{1}{Q_r} - \dfrac{1}{Q_0}}{\dfrac{1}{Q_r} + \dfrac{1}{Q_0}}. \tag{6.9}$$

It is useful to observe that there are three different conditions for coupling of dissipation and leakage modes:

1) $Q_r > Q_0$, under-coupled,

2) $Q_r < Q_0$, over-coupled,

3) $Q_r = Q_0$, critically-coupled.

Unlike the analysis performed by Karanti in [100], we are interested in the maximum energy absorption of the representative resonator and dipole-plate scatterer, which is achieved for critical coupling. We consider a low loss air and foam substrate with $\tan\delta \sim 10^{-6}$ and $\tan\delta \sim 10^{-3}$. This enables the designer to achieve the highest total quality factor. The metal conductivity is considered to be $\sigma = 4.9 \times 10^7$ S/m. The dipole length is $L = 46$ mm, which is approximately a half-wavelength at $f = 3.2$ GHz in the case of a dipole situated at a height of $h = 1$ mm above the metallic plane. The quality factors of a cavity formed by dipoles with widths of 1 mm and 0.2 mm placed at variable heights above the metallic backplane are depicted in Fig. 6.8 and Fig. 6.9, respectively.

Obviously, the critical coupling for the dipole of width $w = 1$ mm is attained at a height of $h = 0.7$ mm and $h = 1.2$ mm for the case of an air substrate and foam substrate,

respectively. The corresponding radiation quality factors are $Q_{r, air} = 601$ and $Q_{r, foam} = 503$, and the total quality factors are equal to $Q_{t, air} = 300$ and $Q_{t, foam} = 252$, respectively; see Fig. 6.8a and Fig. 6.9a. The critical coupling for a dipole of width $w = 0.2$ mm is achieved at a height of $h = 0.9$ mm and even $h = 1.5$ mm for an air substrate and foam substrate, respectively. The corresponding radiation quality factors attain slightly higher levels of $Q_{r, air} = 757$ and $Q_{r, foam} = 540$, with total quality factors equal to $Q_{t, air} = 382$ and $Q_{t, foam} = 275$, respectively; see Fig. 6.8b and Fig. 6.9b.

It follows that the narrower the dipole width, the higher the total quality factor. However, the effect of narrowing the dipole width intended to increase the total quality factor is less significant if the substrate possesses a higher relative permittivity and is lossy. To see this we compare $Q_{t, 1mm} = 300$ and $Q_{t, 0.2mm} = 382$ in the case of an air substrate with $Q_{t, 1\ mm} = 252$ and $Q_{t, 0.2\ mm} = 275$ in the case of a foam substrate.

Apparently, there is an optimum dipole height for achieving a maximum total quality factor, which is in the range from 0.6 mm to 0.7 mm for both investigated dipole widths placed on the air substrate (Fig. 6.8). Similarly, the range is from 0.7 mm to 0.9 mm for both widths of dipoles when placed on the foam substrate (Fig. 6.9). If the dipole height is lower, then it is seen that the total quality factor dramatically drops; see also Fig. 6.10. In addition, it is worth mentioning that the higher the permittivity and loss of the substrate, the higher the dipole height must be above the metallic plane to achieve critical coupling (*i.e.* the theoretical point where the reflection coefficient goes to zero).

Comparing the heights of the dipoles for which the Q_r and Q_0 curves intersect, we observe: 0.7 mm vs. 1.2 mm for the dipole width $w = 1$ mm; see Fig. 6.8a and Fig. 6.9a, and 0.9 mm vs. 1.5 mm for $w = 0.2$ mm; see Fig. 6.8b and Fig. 6.9b. Furthermore, the higher the substrate permittivity and loss, the larger the difference between the optimal height required to achieve the maximum total quality factor (in indirect proportion) and the optimal height to achieve critical coupling (in direct proportion).

The dependence of the reflection coefficient on frequency and dipole height above the metallic plane is depicted in the form of the surface plots in Fig. 6.11 and Fig. 6.12. As the relative permittivity and loss increase, the value of the reflection coefficient degrades, which constitutes the most significant effect (compare Fig. 6.11b vs. Fig. 6.12b). The same effect applies in the case of narrowing the dipole width; compare Fig. 6.11a vs. Fig. 6.11b and Fig. 6.12a vs. Fig. 6.12b.
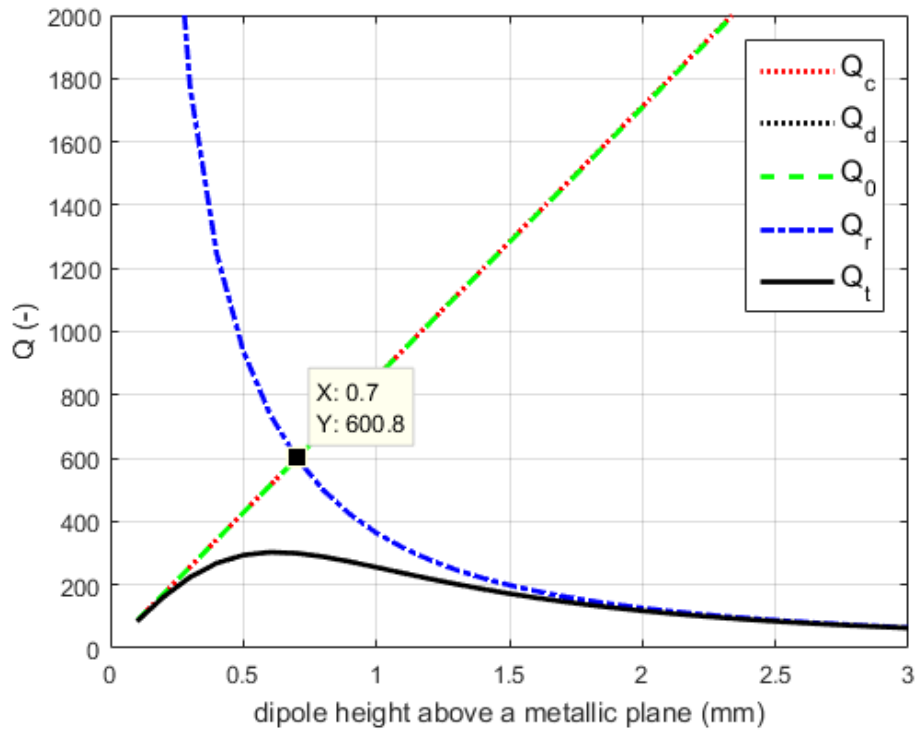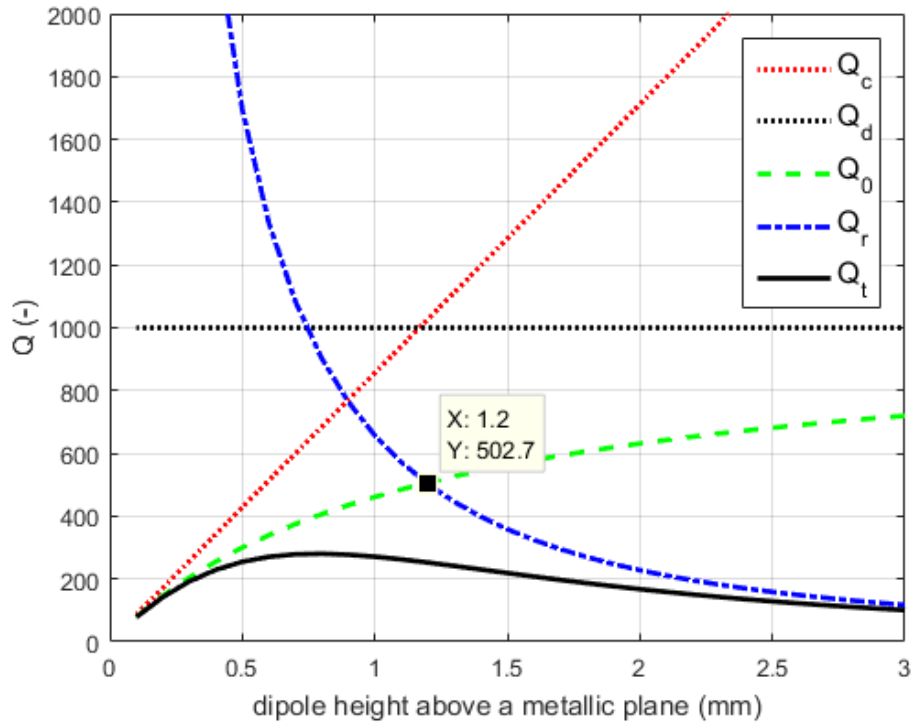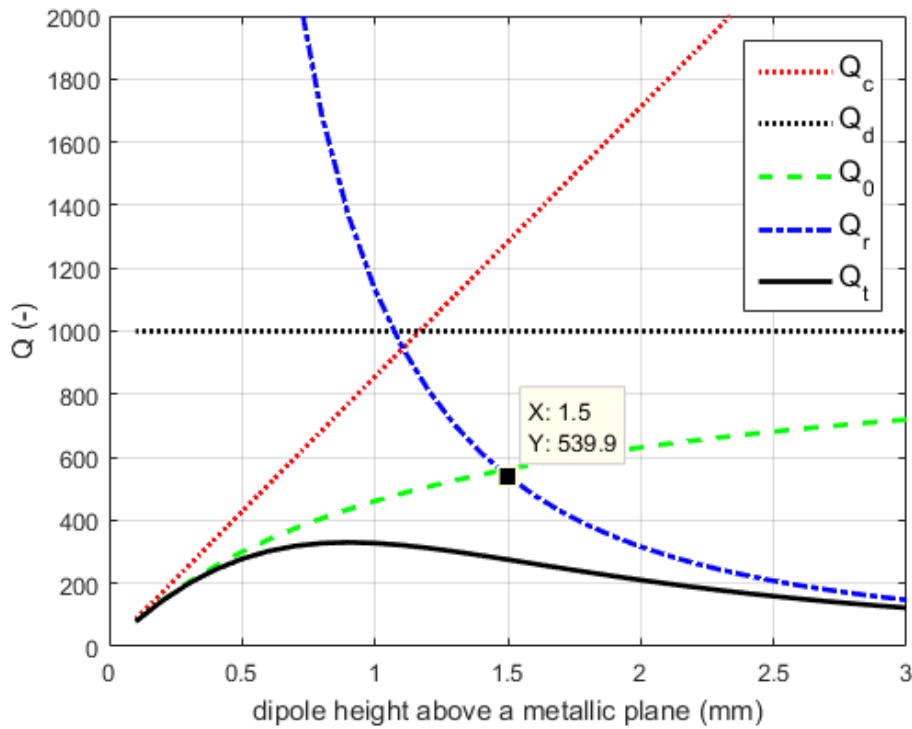
(a)
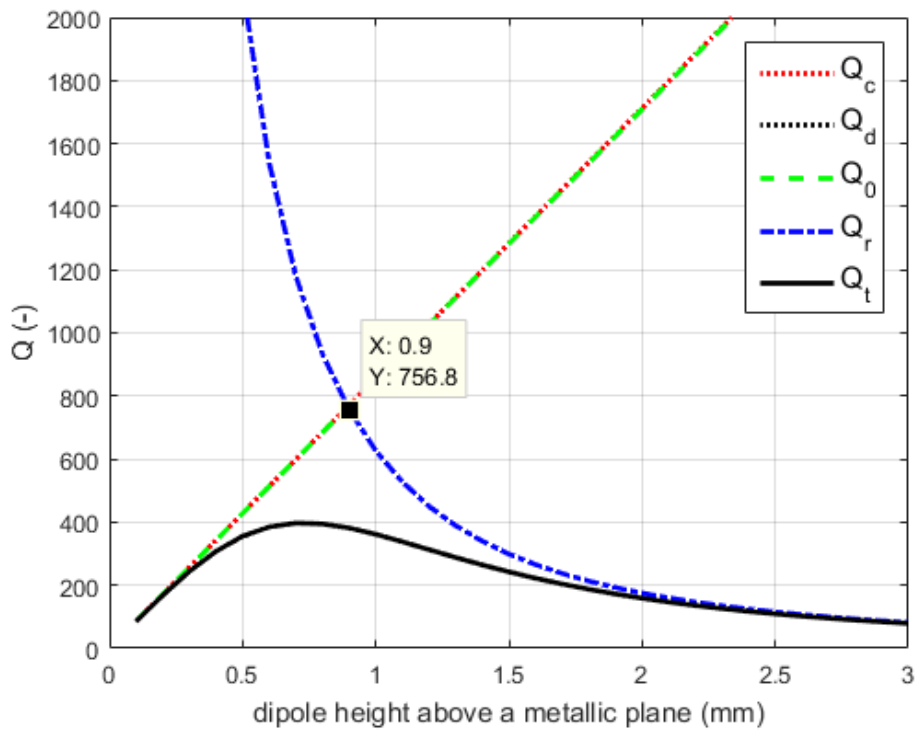
(b)

Fig. 6.8: Quality factors vs. height of a dipole placed on an air substrate above an infinite metallic plane. Dipole size equates to: (a) 46×1 mm^2, and (b) 46×0.2 mm^2. Intersection of the Q_0 and Q_r curves correspond to critical coupling according to [106].

(a)

(b)

Fig. 6.9: Quality factors vs. height of a dipole placed on a foam substrate above an infinite metallic plane. Dipole size equates to: (a) 46×1 mm^2, and (b) 46×0.2 mm^2. Intersection of the Q_0 and Q_r curves correspond to critical coupling according to [94].

Therefore, there is a trade-off between: maximization of total quality factor (which minimizes the single scatterer resonance bandwidth and maximizes the overall transponder bit density), minimization of the reflection coefficient (affecting the deep resonant minima of the *RCS* curve), and the requirement for a low profile and a small surface area of the transponder. When we utilize a low permittivity and a low loss foam-type substrate that enables the support of a thin dielectric substrate with a metallic transponder motif above a metallic plate, the targeted trade-off between the three competing requirements can be achieved using half-wavelength dipole strips of approximately 1 mm in width and placed at a height of approximately 1 mm above a plate. Further reducing either the strip width or its height above the plate degrades either the depth or bandwidth of the resonant minima on the *RCS* curve; see also Fig. 6.13 and Fig. 6.14.
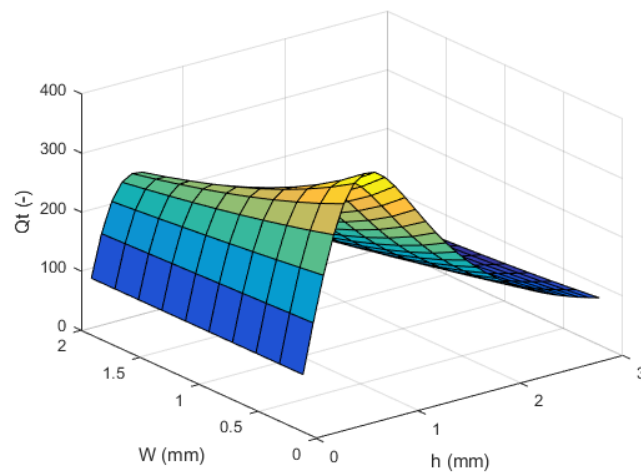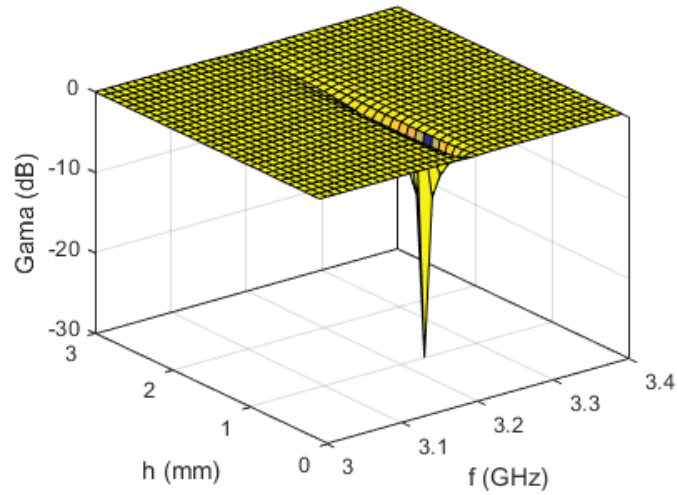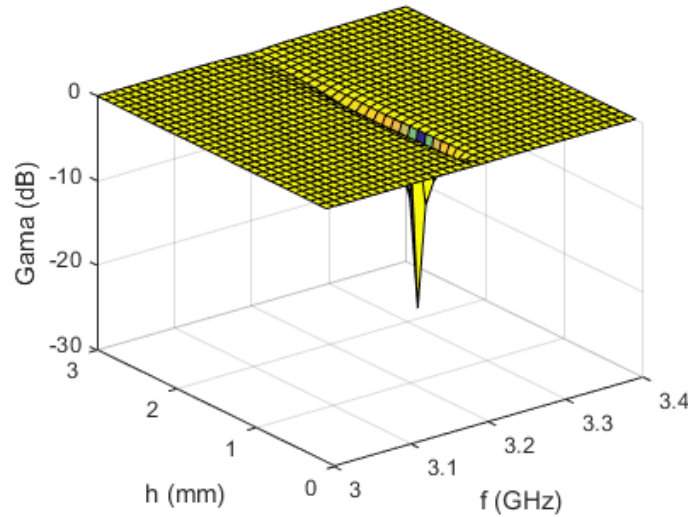

(a)
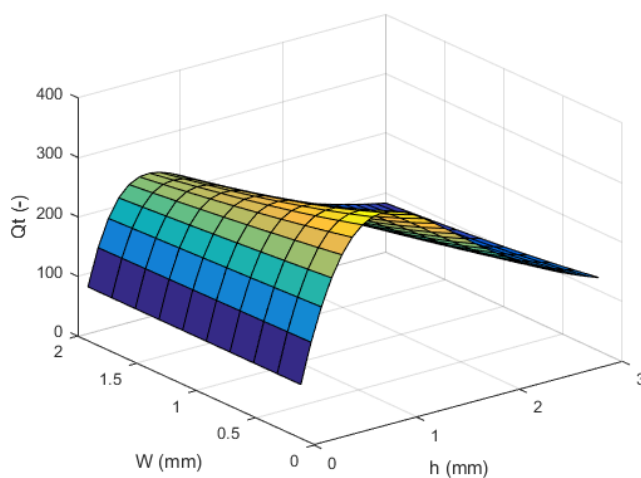
(b)

Fig. 6.10: Total quality factor corresponding to a dipole length of 46 mm as function of dipole width and height above a metallic plane for: (a) an air, and (b) a foam substrate.
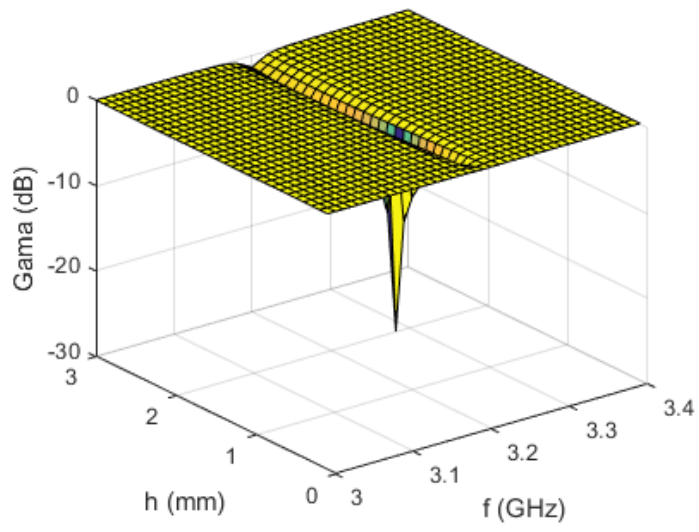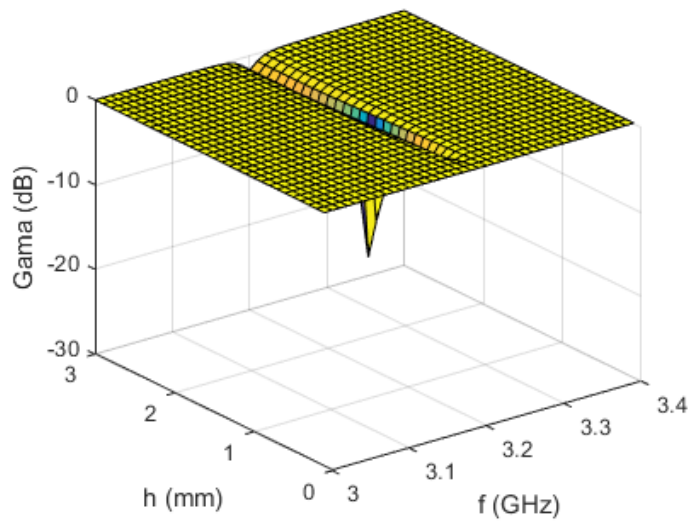
(a)

(b)

Fig. 6.11: Reflection coefficient vs. frequency and dipole height on an air substrate placed above a metallic plane, the dipole size is: (a) 46×1 mm^2, and (b) 46×0.2 mm^2.

In order to consider metallic losses of a dipole-plate model, we employ the commercial MoM simulator Zeland IE3D to perform parametric studies of a single half-wavelength dipole, which is closely coupled to a metallic plate of 60×60 mm^2; see Fig. 6.13 to Fig. 6.15. A planar dipole was selected as a reference, which is assumed to operate in free space at a resonant frequency of 3.12 GHz. The length l of the reference dipole is 47 mm, while its width w is 1 mm. It is situated on an air substrate with a relative permittivity $\varepsilon_r = 1$ and thickness $h = 1$ mm (referred to as 'base size' in Fig. 6.13 to Fig. 6.15)

Fig. 6.12: Reflection coefficient vs. frequency and dipole height on a foam substrate placed above a metallic plane. The dipole size is: (a) 46×1 mm^2, and (b) 46×0.2 mm^2.
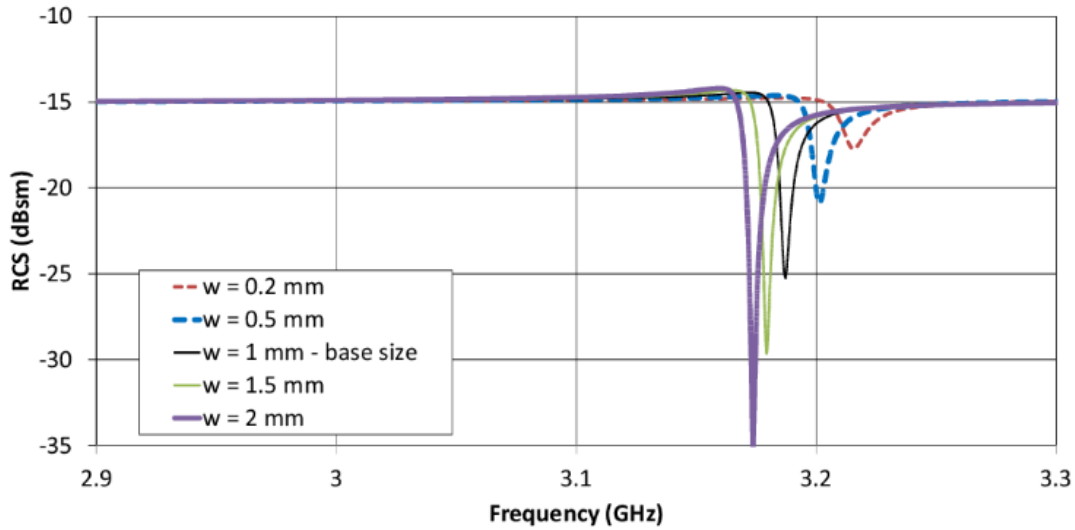
Fig. 6.13: *RCS* response of a half-wavelength planar dipole closely coupled to a finite-sized metallic plate of size of 60×60 mm^2 at a height of 1 mm with the dipole width w serving as a parameter.

As was mentioned above, the aim of the quality chipless RFID transponder design is to reach a high *RCS*, sufficiently narrow and deep resonance drops and, at the same time, a small overall size. These parameters have an antagonistic effect, so an acceptable trade-off must be found. As it can be seen in Fig. 6.13 and Fig. 6.14, the depth of the resonance drop is directly proportional to the dipole width and requires a specific value of the substrate thickness (approximately 2 mm for an air substrate).
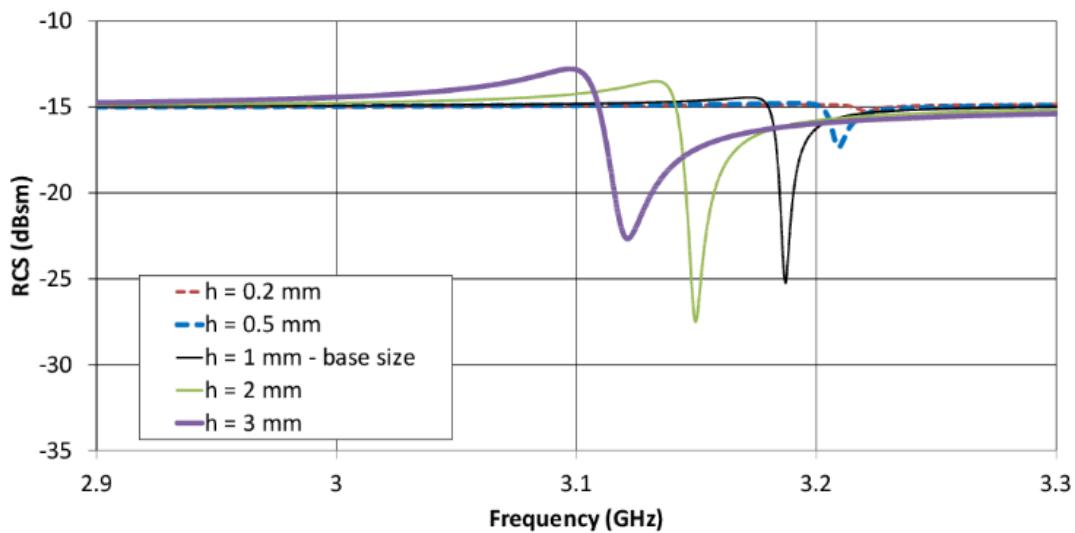

Fig. 6.14: *RCS* response of a half-wavelength planar dipole of width 1 mm closely coupled to a finite-sized metallic plate of size 60×60 mm^2 with the substrate height h serving as a parameter.

Therefore, the increase in the dipole width leads to an inconveniently large transponder area. Furthermore, the increase in the substrate height decreases the total quality factor, which in turn results in a wider resonance. Similarly, the increase in ground plane size raises the *RCS* level and reduces the depth enhancement, while at the expense of a larger structure; see Fig. 6.15. For a given ground plane size it can be found a dipole length *l* at witch a depth of a dip caused by the dipole is maximal. In case of plate size 60 × 60 mm^2 this happens approximately for a length equal to 26 mm; see Fig. 6.16.
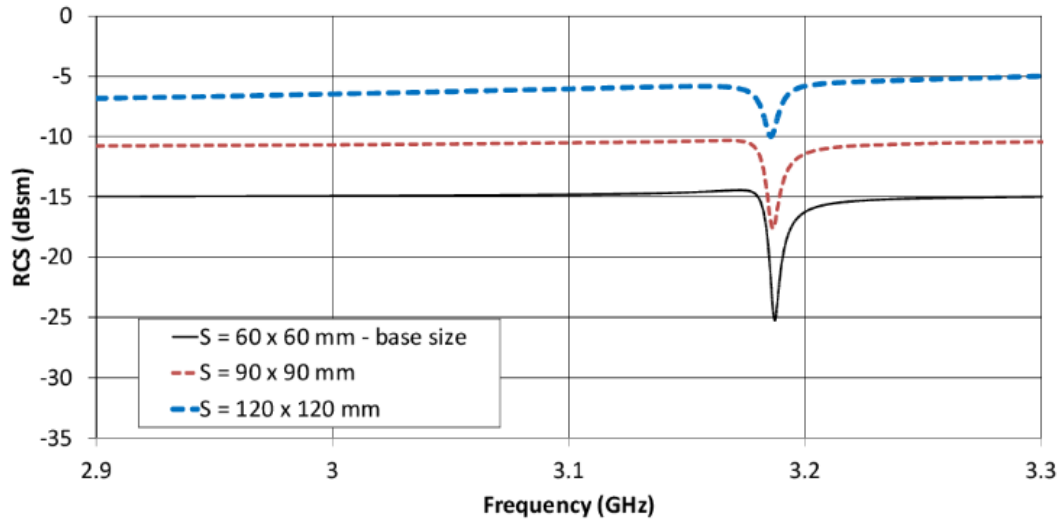

Fig. 6.15: *RCS* response of a half-wavelength planar dipole closely coupled to a finite-sized metallic plate with plate size *S* serving as a parameter.
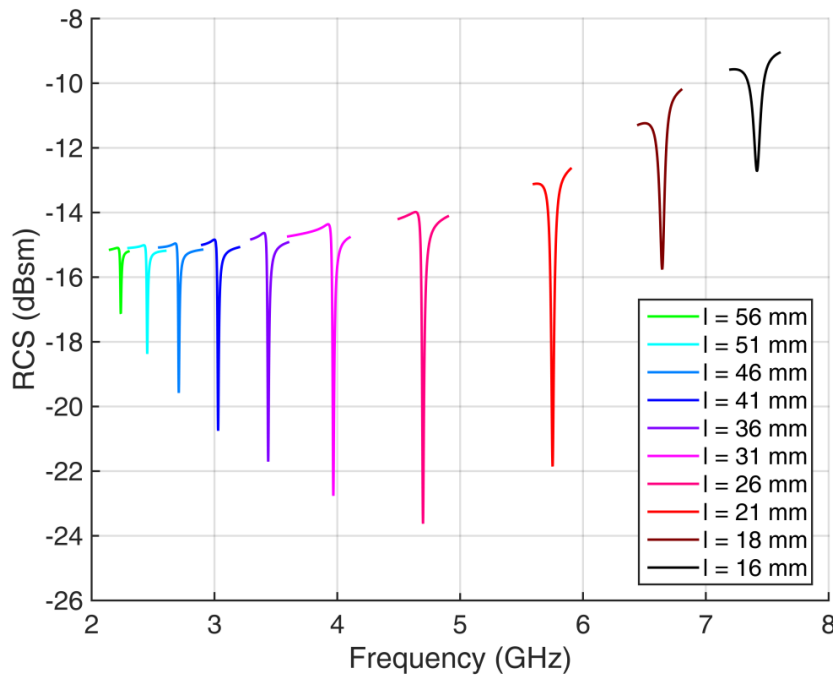

Fig. 6.16 *RCS* response of a half-wavelength planar dipole closely coupled to a metallic plate of size 60 × 60 mm^2 with dipole length *l* serving as a parameter.

The application of a high permittivity substrate, which can minimize the structure thickness, leads to a significant reduction in the depth of the resonance due to the electromagnetic field storage between the dipole and the plate; see Fig. 6.17.
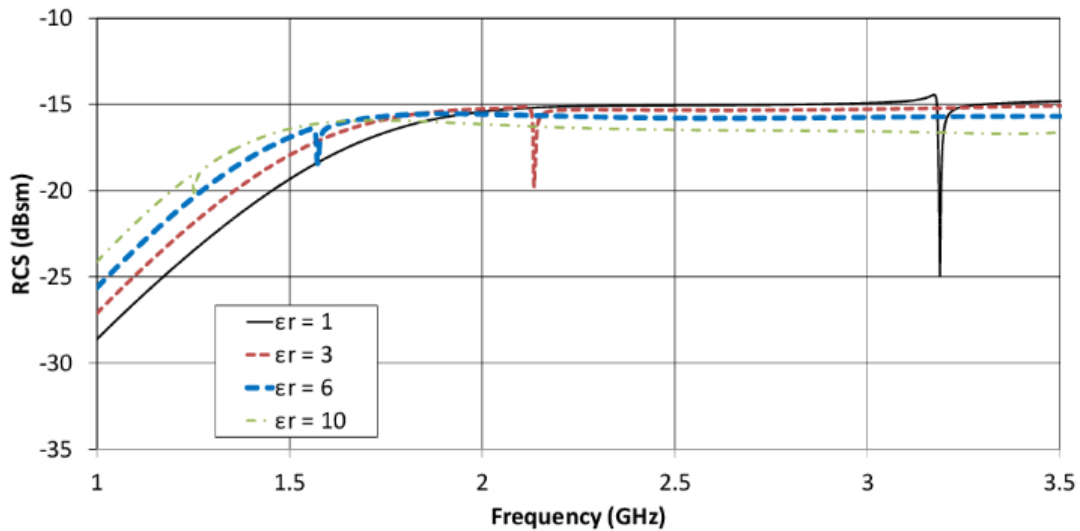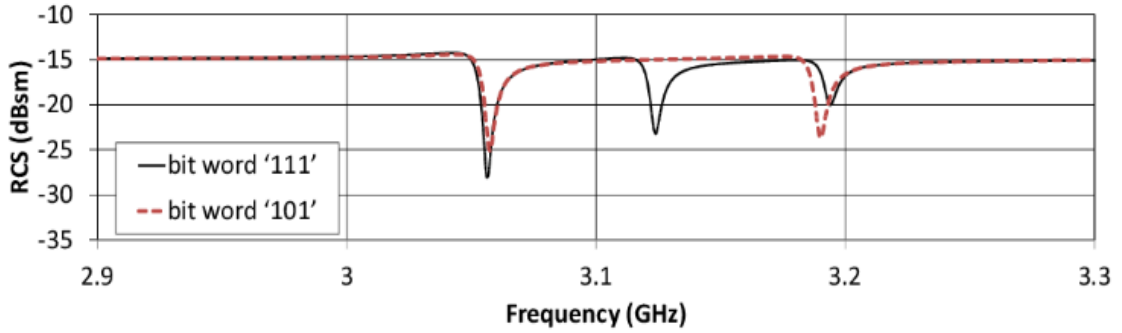

Fig. 6.17: *RCS* response of a dipole closely coupled to a finite-sized metallic plate of size 60×60 mm^2 with substrate relative permittivity ε_r serving as a parameter.

To analyse the stability of the *RCS* response due to topological changes in the arrangement of dipole resonators, a parametric study was conducted of a triplet of detuned half-wavelength dipoles closely coupled to the same metallic plate of 60×60 mm^2; see Fig. 6.18 and Fig. 6.19. The dipole triplet selected as a reference structure operates at the resonance frequencies of 3.05 GHz, 3.12 GHz, and 3.19 GHz.

The length of the dipole strips varies from 46 to 48 mm with a length increment Δl reaching 1 mm. Their width attains 1 mm and their transverse distance g is 1.5 mm (it is referred to as 'base value' in the figures). Similar to the single dipole analysis, the triplet is situated on an air substrate that is 1 mm thick.

As it was already mentioned, the frequency stability of the resonance drop is the key parameter to gauge the reliability of a bit reading of a transponder. If the mutual coupling of each pair of neighbouring dipoles, determined by their separation distance g, is too strong, then a frequency shift of neighbouring drops can be observed provided that the zero bit is coded in the bit word; see Fig. 6.18. The removal of a middle resonator in the case where the gap $g = 0.3$ mm causes a relative frequency shift in the position of the upper resonance drop towards the position of the removed resonator that is approximately equal to 30 %; see Fig. 6.18c. The acceptability of such a shift for successful tag identification is determined by the threshold parameter settings within the reading procedure.
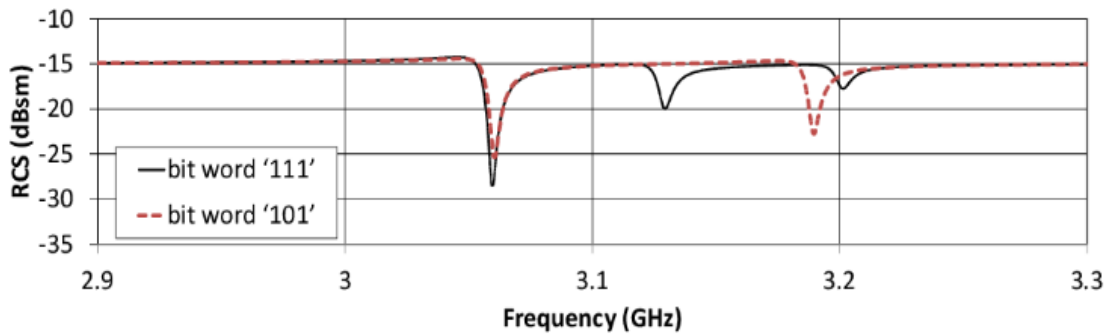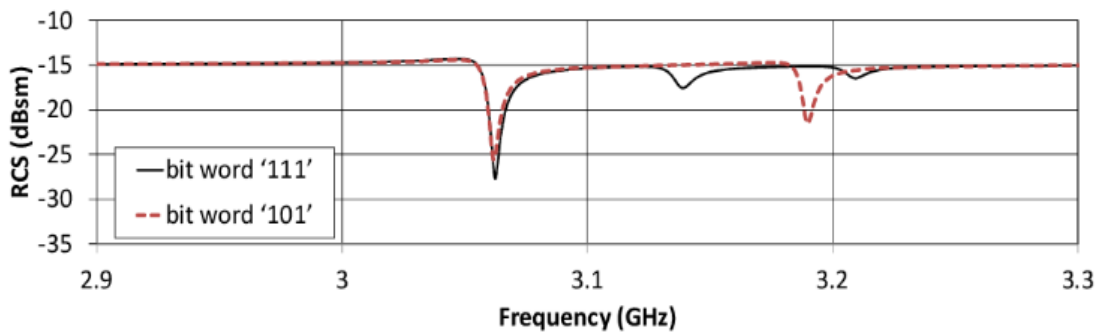
Fig. 6.18: *RCS* response of a triplet of half-wavelength planar dipoles closely coupled to a finite-sized metallic plate with mutual separation distance *g* serving as a parameter. (a) $g = 1.5$ mm (base value), (b) $g = 0.75$ mm, and (c) $g = 0.3$ mm.

A similar effect is caused by a length increment that is too small (*i.e.* a small frequency step). If the middle resonator is removed (in the case where the length increment $\Delta l = 0.2$ mm; see Fig. 6.19c, the frequency shift of the upper resonance decreases to a position somewhere in between the middle and upper resonances. As a result, it becomes impossible to correctly recognize the resonance (bit) that has been removed.
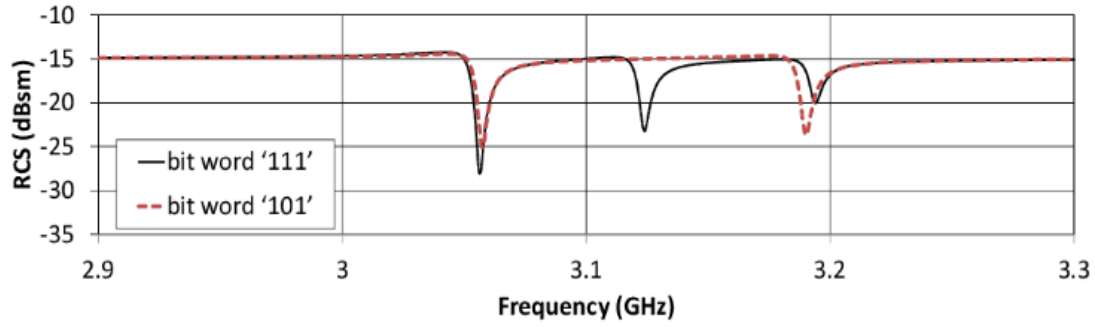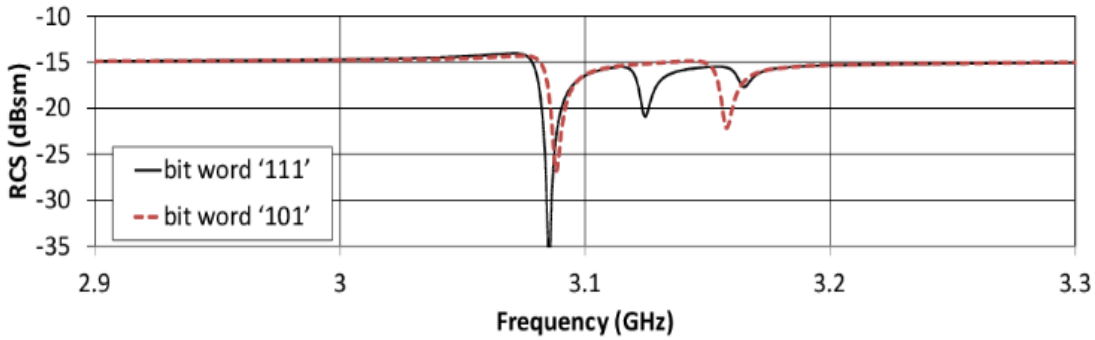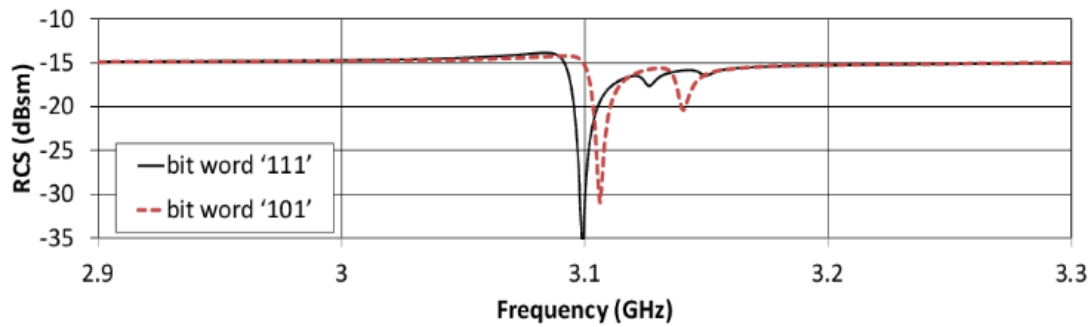
Fig. 6.19: *RCS* response of a triplet of half-wavelength planar dipoles closely coupled to a metallic plate of size of 60 × 60 mm^2 with length increment Δl as a parameter. (a) Δ = 1 mm, (b) Δl = 0.5 mm and (c) Δl = 0.2 mm.

6.2.2 TOPOLOGY, SIMULATION AND MEASUREMENT RESULTS OF THE TAG

The 20-bit chipless RFID tag is composed of an array of detuned planar dipoles closely coupled to a rectangular metallic plate of size 60 × 60 mm^2, operating within the frequency range of 2.2 to 3.5 GHz; see Fig. 6.20. The dipole resonators are located at a distance of approximately 0.01 λ_0 from the metallic plate at the central frequency within the band of interest. Although the respective distance enables sufficient excitation of

98

resonators, the resonators are close enough to increase the quality factor to sufficiently reduce the impedance bandwidth. The length of dipole strips varies froM37 to 56 mm with a length increment of 1 mm. Their width accounts for 1 mm and their transverse distance is 1.5 mm. The substrate thickness between the dipole array and plate is 1.1 mm. The substrate comprises of Rogers RO4350 and a foam layer. The former has a relative permittivity of $\varepsilon_r = 3.66$, a loss tangent of $\tan \delta = 0.003$ and a thickness of 0.1 mm, while the latter has the relative permittivity of $\varepsilon_r \sim 1.3$, a loss tangent of $\tan \delta \sim 0.02$, and a thickness of 1 mm. These properties help to reduce the effective permittivity and thus deepen the corresponding resonant drops; see Fig. 6.17.
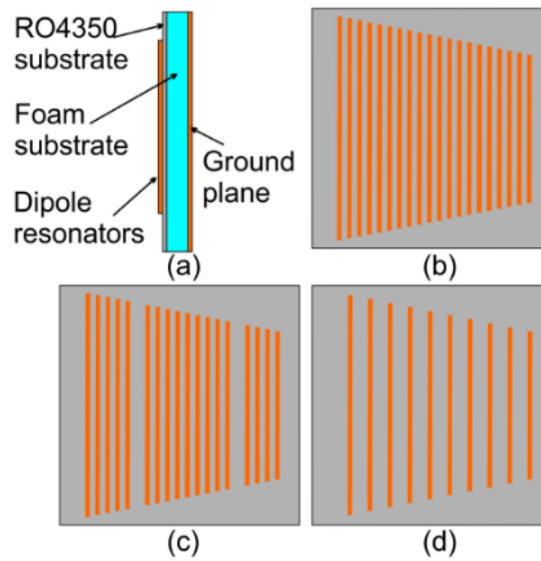
Fig. 6.20: Cross-section (a) and layouts of investigated 20-bit tags constituted by dipoles closely coupled to a rectangular plane with coding information (b) 11111111111111111111, (c) 11111011111111101111 which are missing the 6th and 16th elements, and (d) 01010101010101010101 which are missing every odd element.

The chipless tags were simulated by the MoM software Zeland IE3D, using the infinite dielectric layer implementation with 20 cells per wavelength and narrow edge cells to perform a precise modeling of the current density distribution in a transversal cut of the strip. The frequency verification and amplitude stability of the *RCS* response for the case when the zero bits are coded in the bit word was performed by means of three different 20-bit tags representing the bit words '11111111111111111111', '11111011111111101111' and '01010101010101010101' according to the configurations indicated in Fig. 6.20b - d. The very good robustness of the *RCS* curve was confirmed. For arrays with zero bits we may notice that, due to the removal of the 6th and 16th or alternate scatterers, respectively, the corresponding resonant peaks are missing without any effect on magnitude distortion and frequency interval uniformity of the *RCS* curve; see Fig. 6.21.

Furthermore, the *RCS* level is relatively high (approximately -15 dBsm), whereas the depths of the resonance drops are about 2 - 5 dB. This is due to the losses of the foam substrate whose scale exceeds the values considered in the theoretical analysis. The influence of different objects attached to the lower part of the transponders was verified only by performing measurements, which can be considered as a proven technique; see Fig. 6.25.
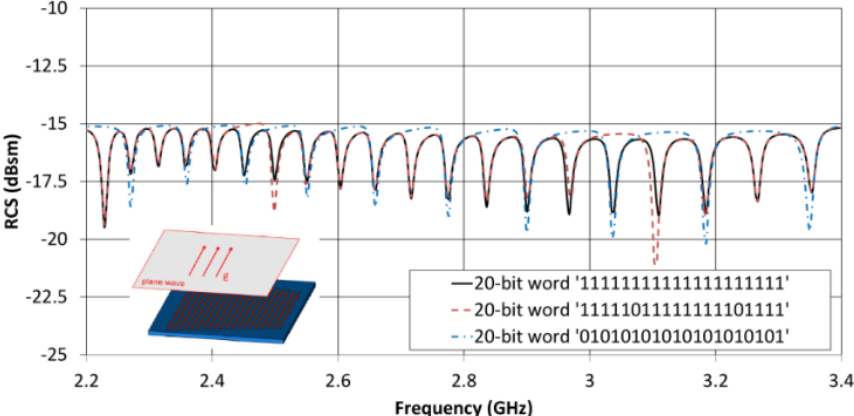
Fig. 6.21: Simulated *RCS* response of bit words '11111111111111111111' in comparison to '11111011111111101111' and '01010101010101010101' in free space.

To predict the degradation of the tag *RCS* response to slant polarization and an obliquely incident electromagnetic wave, a series of simulated parametric studies were performed; see Fig. 6.22, Fig. 6.23 and Fig. 6.24.
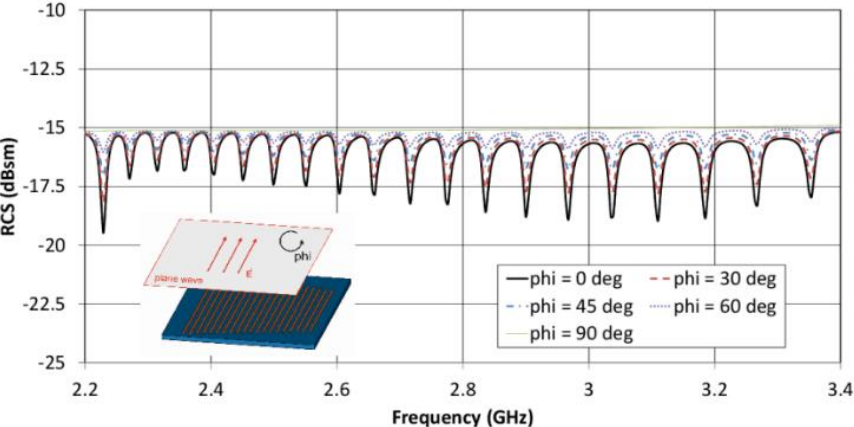
Fig. 6.22: Simulated *RCS* response of a 20-bit tag to a slant polarization of a perpendicular electromagnetic wave in the tag surface plane with the polarization angle serving as a parameter.
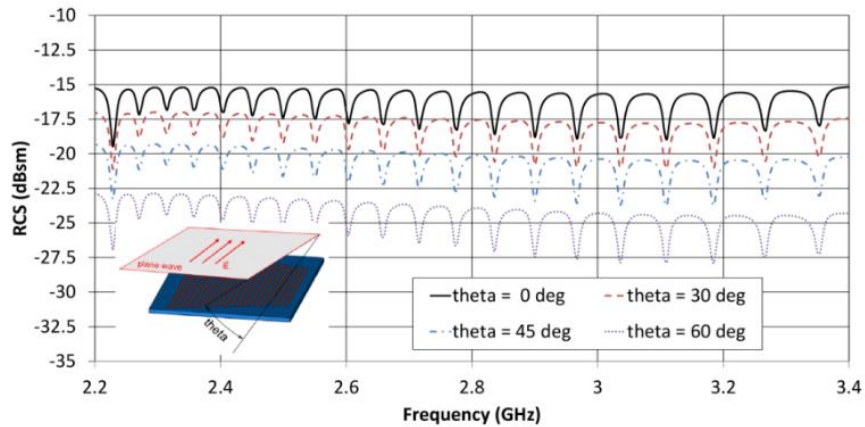
Fig. 6.23: Simulated *RCS* response of a 20-bit tag to an obliquely incident electromagnetic wave in a plane parallel to the dipole axes with the elevation angle serving as a parameter.
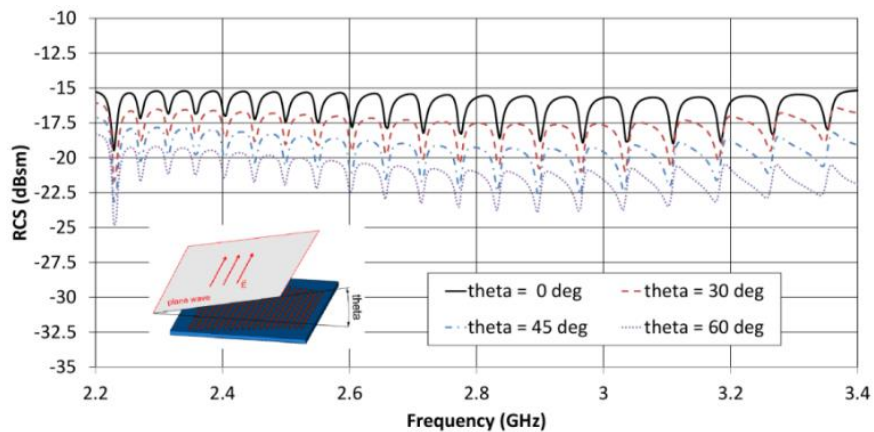
Fig. 6.24: Simulated *RCS* response of a 20-bit tag to an obliquely incident electromagnetic wave in a plane perpendicular to the dipole axes with the elevation angle serving as a parameter.

The polarization slant measured from the dipole axis at the tag surface plane (Fig. 6.22), the elevation tilt in a plane parallel to the dipole axes (Fig. 6.23), and in a plane perpendicular to the dipole axes (Fig. 6.24) were chosen to all be in the range of {0°, 30°, 45°, 60°, 90°}. As expected with linearly polarized scatterers, both the polarization slant and the oblique incidence performance deteriorates the *RCS* performance, but each of them in a different way. In the case of a polarization slant, the depth of the resonance drops decreases with increasing angle and reaches approximately half of the original depth at an angle of 45°. This is due to a shorter projection of the dipole length into the polarization plane when each of the dipoles has an electrically smaller size compared to the metallic plate size. The absolute value of individual drops in the *RCS* curve in the range of 1.5 to 2.0 dB are still present allowing for correct determination of the individual resonances for the angle considered. On the other hand, increasing the

101

elevation tilt either in a plane parallel or perpendicular to the dipole axes causes a complete reduction in the *RCS* level while maintaining almost the same original level of the individual drops. In the case of a tilt in a plane parallel to the dipole axes (Fig. 6.23), the projection of both the dipole lengths and the size of the plate area in the direction of wave arrival are proportionally smaller. In the case of a tilt in a plane perpendicular to the dipole axes (Fig. 6.24), even the shape of the resonance drops deteriorates especially at higher frequencies, as the situation here is more complicated. The projection into the direction of wave arrival causes the dipoles to appear closer together and, consequently, the wave imparts a relatively small phase shift on each element.

The basic set of measurements was performed in an anechoic chamber at a distance of 500 mm from the radiating double ridge horn antenna. Rectangular metal plate of 60×60 mm^2 in size (corresponding to the measured tags) and 0.3 mm in thickness was used as a reference scatterer; see section 4.4 for the description of the measurement method.

In order to guarantee that the transponders were electrically immune to objects situated directly below them, we performed measurements on a rectangular plate of 150×200 mm^2 made of common materials such as cardboard (thickness $t = 6$ mm), wood ($t = 5$ mm), plastic ($t = 1$ mm) and metal ($t = 0.1$ mm). Furthermore, we also employed an agar phantom of $120 \times 80 \times 15$ mm^3 with $\varepsilon_r \sim 55$ and $\tan \delta \sim 0.5$ representing the influence of a human body. Fig. 6.25 contains three curves corresponding to the tag configurations from Fig. 6.20b - d. The solid black line represents the full 20-bit word '11111111111111111111', whereas the dashed red line symbolizes the bit word if two '0' bits are coded, while the dot-and-dashed blue line symbolizes the bit word for the case when every other bit is '0'. If low loss materials such as cardboard, wooden and plastic plates are utilized, the *RCS* response shows a similar character as in the free space measurement; see Fig. 6.25b − d. It should be noted that the bit word recognition can be attained on the basis of the same criteria. A slightly different effect can be observed if a high loss object, such as an agar human body phantom, is measured; see Fig. 6.25e. The employment of a high loss object hinders the resonance drop such that it amounts to 7 - 15 dB, which is advantageous for the measurement and bit word evaluation. In the case where the transponder situated over the metallic plate is measured, a totally different character of *RCS* response can be observed; see Fig. 6.25f. If an additional metallic plate isolated from the tag ground is used, the resonance drops are transformed into resonance peaks. However, owing to appropriate evaluation criteria, it is still possible to determine the bit information. The *RCS* response embodies strong resonance peaks with magnitudes in the range of 5 to 10 dB. Therefore, an in-depth follow-up analysis is indispensable to better

understand this behavior and improve the respective type of tag so that its reliable operation can be eventually attained for cases when it is attached to metallic objects.
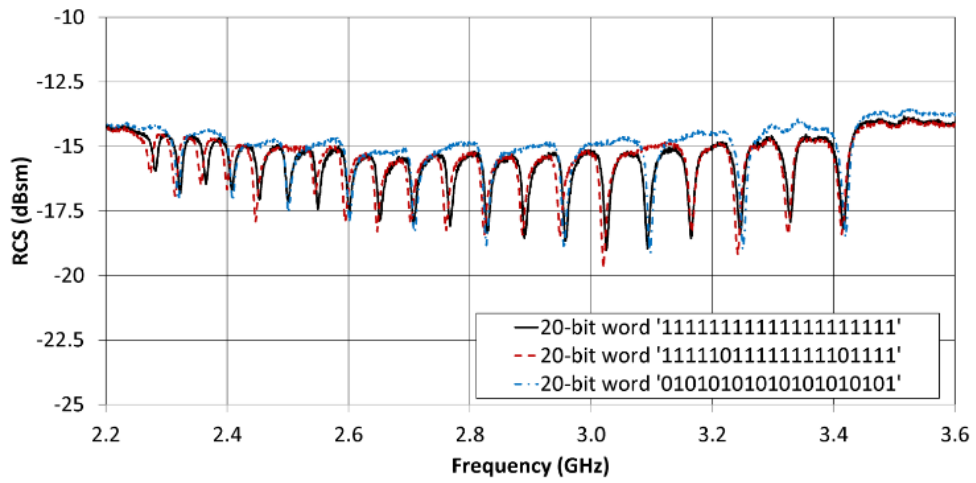
(a)
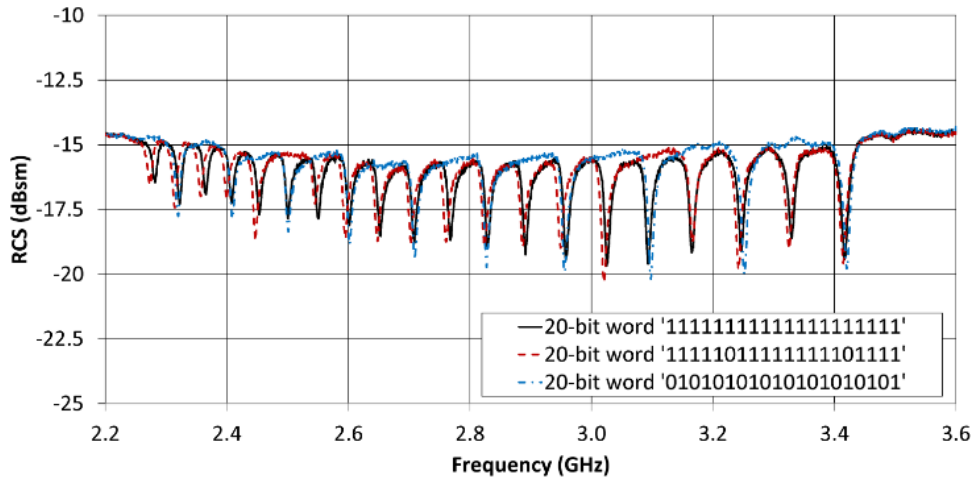
(b)
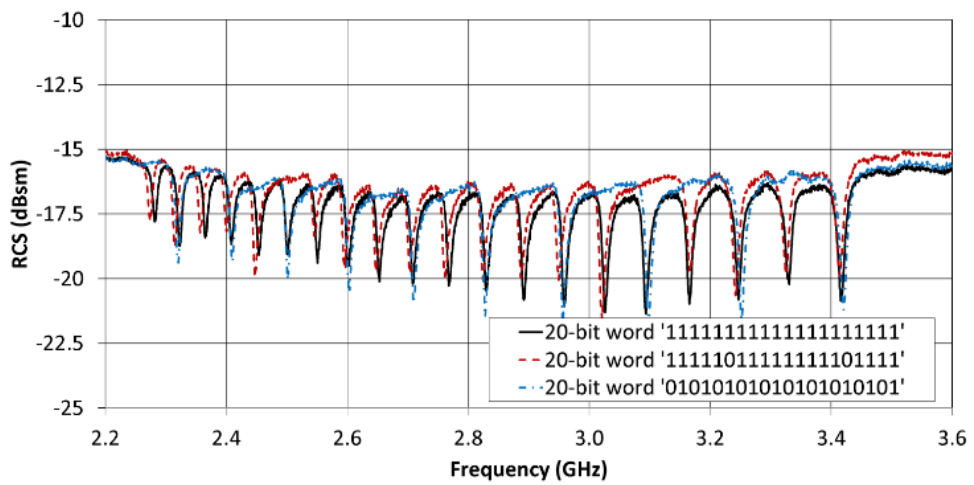
(c)
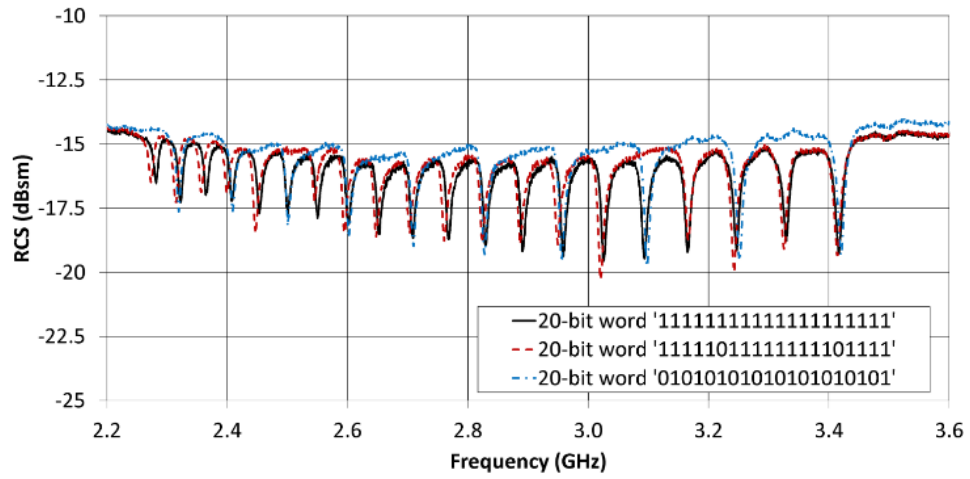
(d)
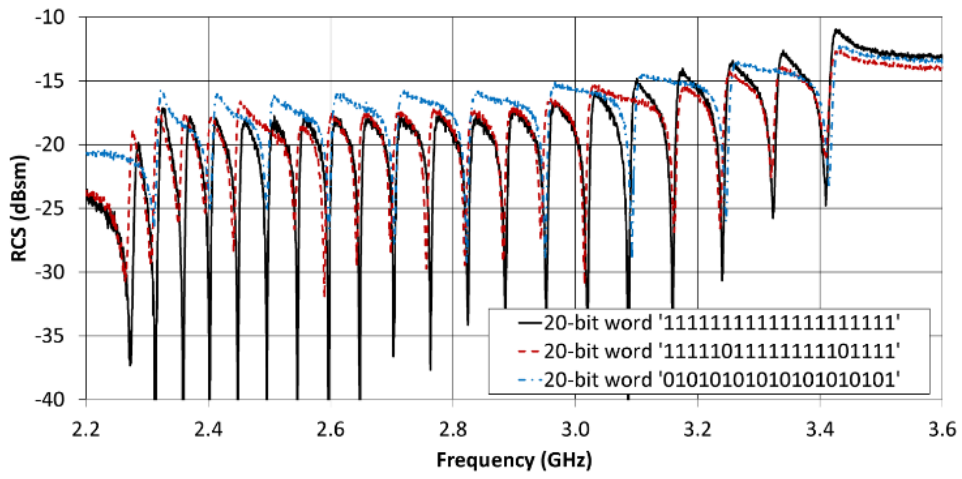
(e)
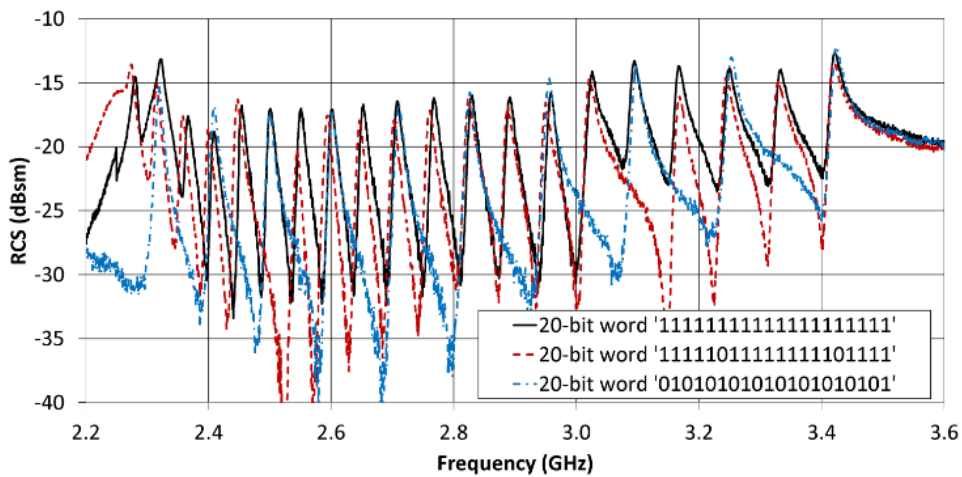
(f)

Fig. 6.25: Measured *RCS* response of bit words '11111111111111111111' in comparison to '11111011111111101111' and '01010101010101010101' in (a) free space, and attached to: (b) a cardboard plate, (c) a wooden plate, (d) a plastic plate, (e) an agar human body phantom, (f) a metallic plate.

To verify the basic capability of transponder operation outside the anechoic chamber under realistic conditions, indoor measurements were taken for two basic cases, namely in free space and on the rectangular wooden plate of size 150×200 mm^2. In order to improve the signal-to-noise ratio, the distance between the transponder and identical radiating double ridge horn antenna was reduced to 250 mm; see Fig. 6.26.

Fig. 6.26: Setup using monostatic configuration for indoor measurement with detail of 20-bit tag constituted by dipoles closely coupled to a rectangular metallic plate attached to a wooden plate.
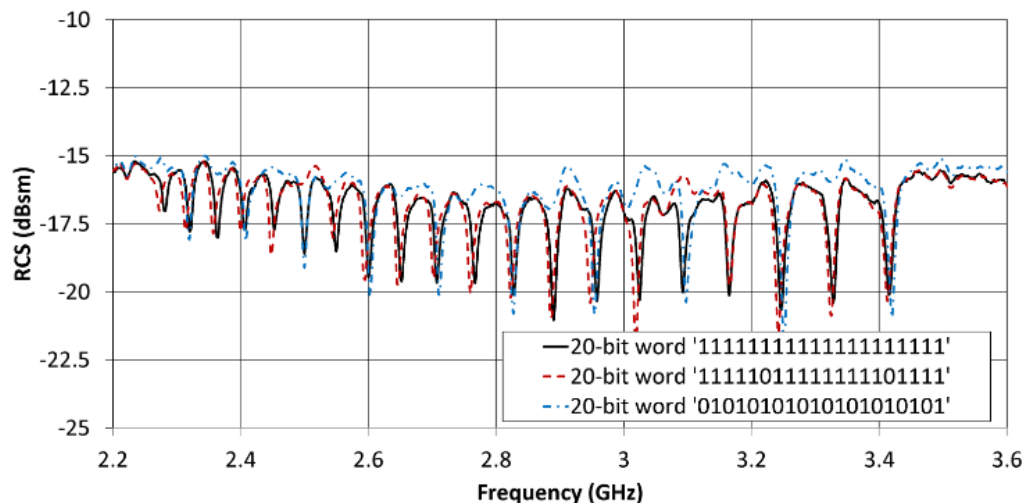
Fig. 6.27: Measured *RCS* response of bit words '11111111111111111111' in comparison to '11111011111111101111' and '01010101010101010101' in free space for the indoor scenario.

In both cases the ripples in the *RCS* response expanded due to the multipath propagation and multiple reflections. Yet given the measuring distance of 250 mm, the depth of the resonance drop was significantly higher than the ripple, so the bit information can be identified; see Fig. 6.27 and Fig. 6.28. Furthermore, the drops in the *RCS* response of a transponder situated over the wooden plate exceed the drops in the free space case. This phenomenon is attributable to the presence of a larger object that, to a certain degree, shadows the multiple reflections from the wall or other objects situated in a straight line behind the measured transponder; see Fig. 6.28.
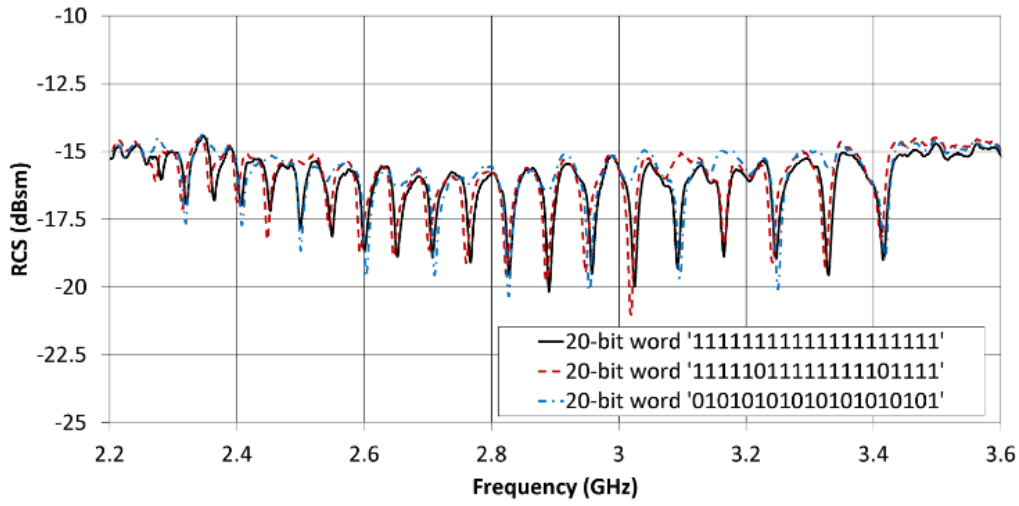
Fig. 6.28: Measured *RCS* response of bit words '11111111111111111111' in comparison to '11111011111111101111' and '01010101010101010101' on a wooden plate for the indoor scenario.

6.3 SUMMARY

The 20-bit chipless RFID tag, which is 52×50 mm^2 in size and based on the slot-in-plate array, has been proposed in section 6.1 [97]. Achieved spatial capacity is 0.8 bit/cm^2, and comprehensive encoding bit capacity is 48.1 bit/λ^2/GHz. This approach is complementary to the chipless tag composed of an array of individual U-dipole scatterers. The overall *RCS* response is significantly improved provided that the interrogating signal reflected from a larger radar target contains band-notched resonators, such as slot-type elements placed in the planar rectangular element. The overall response of the plate-scatterer itself is almost 20 dB higher than the response of the tag composed of an array of U-folded dipoles; see subsection 4.1.1.

A modification of the inter-element arrangement in order to eliminate the detuning effect of the missing slot representing '0' bit information on the resonances of neighbouring slots representing '1' bit information has been proposed and verified.

Frequency stability and consequently reliability of reading were significantly improved. Zero bits can be encoded either by removing a resonator or by shorting it. A significant difference between both methods was not observed.

The concept of a dipole array coupled to a metallic plate proposed in section 6.2 [93] exhibits concurrently: high encoding capacity, platform tolerance of electrical parameters when attached to various dielectric objects, and stability of *RCS* response for reliable reading when individual scatterers are removed in order to encode zero bits.

A platform tolerant 20-bit chipless RFID transponder based on an array of dipoles above a plate was theoretically and numerically investigated for maximization of high encoding capacity and robustness of reading response. Moreover, the resulting design was subsequently manufactured and extensively tested. It exhibited a reliable reading performance in cases when it was attached to various dielectric objects. Only the use of a metallic pad led to a different shape in the *RCS* response. Although all 20 resonant peaks were apparent, the transponder configuration in question might be considered unreliable for reading purposes. In comparison to other known solutions, the proposed concept shows a high encoding capacity exceeding $47.4 \, \mathrm{bit}/\lambda^2/\mathrm{GHz}$ together with a relatively high *RCS* response of approximately -15 dBsm. In addition, the design is shown to exhibit a satisfactory resonance drop depth ranging from 2 to 5 dB and sufficient platform tolerance of electrical parameters when the tag is attached to various dielectric objects and the interrogating signal is incident on the tag in a direction perpendicular to its surface. A very good frequency and amplitude stability in the *RCS* response for the cases when zero bits are coded together with the need for reliable reading suggest that the proposed solution is suitable for employment in many chipless RFID applications. The double layer metallization represents an inherent property of the proposed solution as well as a necessary trade-off for platform tolerance.

7 CONCLUSION AND FUTURE RESEARCH

The thesis covers a branch of chipless RFID transponders relatively widely. Based on challenges mentioned in the state-of-the-art chapter, the thesis is focused mainly on improving spatial bit capacity, spectral bit capacity (in frequency domain only), and comprehensive encoding bit capacity (bit/λ^2/GHz) of treated transponders. The only later one takes into account frequency band used correctly. Further, successful attempts have been made to improve robustness and recognisability of the transponders' *RCS* response and platform tolerance of performance parameters. Detailed descriptions of achieved results are summarized at the end of each chapter. A brief overview of them can be found below:

- Strengthening the reliability of chipless RFID reading by improving amplitude and frequency stability of their *RCS* response by two techniques of rearrangement of the positions of individual resonators in scatterer array of the transponder when zero bits are encoded; see section 4.1 [79, 82].

- Fast predicting of the influence of mutual coupling in scatterer array on its performance parameters, i.e. amplitude level and frequency positions of resonances in *RCS* response, by simplified equivalent circuit modeling, applicable to tapered U-folded dipole scatterer; see section 4.2 [85].

- Improving spatial bit capacity of the frequency domain chipless RFID tags using electrically small scatterers based on arrays of spiral loaded dipoles with spatial capacity 1.77 bit/cm^2, and 120.7 bit/λ^2/GHz, which is the highest value among known frequency domain tags [93]; see section 4.3 [80].

- Improving per-unit-length bit capacity of the time domain chipless RFID tag applying a sequential bit reading technique in near field. A 100-bit tag has been proposed with spatial bit capacity of 4.9 bit/cm^2 and 16.7 bit/cm; see section 5.2 [95].

- Enhancement of spectral bit capacity of chipless RFID tags using dipole array-plate concepts (15.4 bits/GHz) in frequency-domain which the highest encoding capacity (47.4 bit/λ^2/GHz) of all known platform tolerant transponder solutions with contemporary *RCS* response at the level of -15 dBsm [93]. Further theoretical and numerical investigation of this concept, which outperforms other tag competitors in individual and overall parameters (spectral bit capacity, *RCS* level, platform tolerance, robustness and recognisability of *RCS* response); see section 6.2 [93].

Conclusions for further development of science or for industry implementation of chipless RFID transponders to be applicable in practice:

- Further improvement of both spectral and spatial encoding capacity is still required if they should replace optical barcodes at least in specific applications.

- Further improvement of maximal reading distance and reliability of reading.

- Finding an optimal topology arrangement focused either to maximization spectral and spatial encoding capacity or reading distance.

- Fully quantify mutual coupling between scatterers in a tag and find principal limitation of maximal encoding capacity taking mutual coupling into account.

- Finding time-effective and low-cost measurement methods for chipless RFID tags which can be performed without the necessity to use a reference scatterer and/or an anechoic chamber.

- Implementing polarization independent techniques for space localization of chipless RFID tags and anti-collision techniques when multiple tags are read.

- Integration of chipless RFID transponders with third-party sensors for sensing environmental quantities, human health conditions, implementation of sensing ability in general.

- Further development of reliable platform-tolerant and especially wearable chipless RFID tags.

- Finding novel applications for chipless RFID transponders, mainly in the Internet of Things (IoT) concept.

LIST OF CANDIDATE'S PUBLICATIONS RELATED TO THE THESIS

All co-authors contributed equally to the creation of all published papers listed below.

Articles in journals with an impact factor

1. Milan Svanda, Milan Polivka, Jaroslav Havlicek, Jan Machac, and Douglas H. Werner. Platform tolerant, high encoding capacity dipole array-plate chipless RFID tags. *IEEE Access*, 7:138707–138720, 2019. **WoS cit.: 0**

2. Jaroslav Havlicek, Cristian Herrojo, Ferran Paredes, Javier Mata-Contreras, and Ferran Martin. Enhancing the per-unit-length data density in near-field chipless-RFID systems with sequential bit reading. *IEEE Antennas and Wireless Propagation Letters*, 18(1):89–92, Jan 2019. **WoS cit.: 0**

3. Milan Svanda, Jaroslav Havlicek, Jan Machac, and Milan Polivka. Polarisation independent chipless RFID tag based on circular arrangement of dual-spiral capacitively-loaded dipoles with robust RCS response. *IET Microwaves, Antennas & Propagation*, 12(14):2167–2171, Nov 2018. **WoS cit.: 3**

4. Jaroslav Havlicek, Milan Svanda, Milan Polivka, Jan Machac, and Jan Kracek. Chipless RFID tag based on electrically small spiral capacitively loaded dipole. *IEEE Antennas and Wireless Propagation Letters*, 16:3051–3054, 2017. **WoS cit.: 8**

5. Milan Svanda, Milan Polivka, Jaroslav Havlicek, and Jan Machac. Chipless RFID tag with an improved magnitude and robustness of RCS response. *Microwave and Optical Technology Letters*, 59(2):488–492, Dec 2016. **WoS cit.: 2**

6. Jan Machac, Milan Polivka, Milan Svanda, and Jaroslav Havlicek. Reducing mutual coupling in chipless rfid tags composed of u-folded dipole scatterers. *Microwave and Optical Technology Letters*, 58(11):2723–2725, Aug 2016. **WoS cit.: 1**

7. J. Havlicek, M. Svanda, J. Machac, and M. Polivka. Improvement of reading performance of frequency-domain chipless RFID transponders. *Radioengineering*, 25(2):219–229, Apr 2016. **WoS cit.: 4**

8. Milan Polivka, Jaroslav Havlicek, Milan Svanda, and Jan Machac. Improvement in robustness and recognizability of RCS response of u-shaped strip-based chipless RFID tags. *IEEE Antennas and Wireless Propagation Letters*, 15:2000–2003, 2016. **WoS cit.: 20**

Peer-reviewed articles

1. Jan Machac, Amine Boussada, Milan Svanda, Jaroslav Havlicek, and Milan Polivka. Influence of mutual coupling on stability of RCS response in chipless RFID. *Technologies*, 6(3):67, Jul 2018. **WoS cit.: 0**

Other papers in WoS database

2. Jaroslav Havlicek, Cristian Herrojo, Javier Mata-Contreras, Ferran Paredes, and Ferran Martin. Stub-loaded microstrip line loaded with half-wavelength resonators and application to near-field chipless-RFID. In *2018 IEEE MTT-S Latin America Microwave Conference (LAMC 2018)*. IEEE, Dec 2018. **WoS cit.: 0**

3. M. Polivka, M. Svanda, J. Havlicek, and J. Machac. Semi-platform tolerant 20-bit chipless RFID tag composed of dipole array closely coupled to plate. In *12th European Conference on Antennas and Propagation (EuCAP 2018)*. Institution of Engineering and Technology, 2018. **WoS cit.: 0**

4. Jan Machac, Milan Polivka, Milan Svanda, and Jaroslav Havlicek. Frequency-domain chipless RFID transponders: Improvement the reading response. In *2018 22nd International Microwave and Radar Conference (MIKON)*. IEEE, May 2018. **WoS cit.: 0**

5. Boussada, J. Machac, M. Svanda, J. Havlicek, and M. Polivka. Erroneous reading of information in chipless RFID tags. In *2017 Progress In Electromagnetics Research Symposium - Spring (PIERS)*. IEEE, May 2017. **WoS cit.: 1**

6. M. Polivka, M. Svanda, J. Havlicek, and J. Machac. Detuned dipole array backed by rectangular plate applied as chipless RFID tag. In *2017 Progress In Electromagnetics Research Symposium - Spring (PIERS)*. IEEE, May 2017. **WoS cit.: 1**

7. Milan Svanda, Jan Machac, Milan Polivka, and Jaroslav Havlicek. A comparison of two ways to reducing the mutual coupling of chipless RFID tag scatterers. In *2016 21st International Conference on Microwave, Radar and Wireless Communications (MIKON)*. IEEE, May 2016. **WoS cit.: 11**

8. Jaroslav Havlicek, Milan Polivka, Milan Svanda, and Jan Machac. Capacitively loaded dipoles for chipless RFID transponder. In *2016 26th International Conference Radioelektronika (RADIOELEKTRONIKA)*. IEEE, Apr 2016. **WoS cit.: 2**

9. Milan Polivka, Jaroslav Havlicek, Milan Svanda, and Jan Machac. Improvement of RCS response of u-shaped strip-based chipless RFID tags. In *2015 European Microwave Conference (EuMC)*. IEEE, Sep 2015. **WoS cit.: 9**

REFERENCES

[1]   Klaus Finkenzeller. *RFID Handbook: Fundamentals and Applications in Contactless Smart Cards and Identification 2nd Edition*. Wiley, 2003. ISBN 0-470-84402-7.

[2]   Shuvashis Dey, Jhantu Kumar Saha, and Nemai Chandra Karmakar. Smart sensing: Chipless RFID solutions for the internet of everything. *IEEE Microwave Magazine*, 16 (10): 26–39, Nov 2015. doi: 10.1109/mmm.2015.2465711.

[3]   Etienne Perret. *Radio Frequency Identification and Sensors*. ISTE Ltd., 2014. ISBN 1848217668.

[4]   Nemai Chandra Karmakar. *Chipless RFID Sensors*. Wiley-Blackwell, 2016. ISBN 1118936000.

[5]   Stevan Preradovic Nemai Chandra Karmakar. *Multiresonator-Based Chipless RFID*. Springer New York, 2011. ISBN 1461420946.

[6]   Reza Rezaiesarlak and Majid Manteghi. *Chipless RFID*. Springer Nature, 2015. doi: 10.1007/978-3-319-10169-9.

[7]   Stevan Preradovic and Nemai Karmakar. Fully printable chipless RFID tag. In *Advanced Radio Frequency Identification Design and Applications*. InTech, Mar 2011. doi: 10.5772/14555.

[8]   Stevan Preradovic and Nemai Karmakar. Chipless RFID: Bar code of the future. *IEEE Microwave Magazine*, 11 (7): 87–97, Dec 2010. doi: 10.1109/mmm.2010.938571.

[9]   Arnaud Vena, Etienne Perret, Smail Tedjini, Guy Eymin Petot Tourtollet, Anastasia Delattre, Frederic Garet, and Yann Boutant. Design of chipless RFID tags printed on paper by flexography. *IEEE Transactions on Antennas and Propagation*, 61 (12): 5868–5877, Dec 2013. doi: 10.1109/tap.2013.2281742.

[10]   Andrew T. Blischak and Majid Manteghi. Embedded singularity chipless RFID tags. *IEEE Transactions on Antennas and Propagation*, 59 (11): 3961–3968, Nov 2011. doi: 10.1109/tap.2011.2164191.

[11]   V. Plessky and L. Reindl. Review on SAW RFID tags. *IEEE Transactions on Ultrasonics, Ferroelectrics and Frequency Control*, 57 (3): 654–668, Mar 2010. doi: 10.1109/tuffc.2010.1462.

[12]   Kenjiro Fukuda, Yasunori Takeda, Yudai Yoshimura, Rei Shiwaku, Lam Truc Tran, Tomohito Sekine, Makoto Mizukami, Daisuke Kumaki, and Shizuo Tokito. Fully-printed high-performance organic thin-film transistors and

circuitry on one-micron-thick polymer films. *Nature Communications*, 5, Jun 2014. doi: 10.1038/ncomms5147.

[13] Cristian Herrojo, Javier Mata-Contreras, Alba Nunez, Ferran Paredes, Eloi Ramon, and Ferran Martin. Near-field chipless-RFID system with high data capacity for security and authentication applications. *IEEE Transactions on Microwave Theory and Techniques*, 65 (12): 5298–5308, Dec 2017. doi: 10.1109/tmtt.2017.2768029.

[14] Rfid and temperature sensing utilizing saw technology. https://rfsaw.com/. Accessed: 2020-01-10.

[15] K. Myny, S. Steudel, S. Smout, P. Vicca, F. Furthner, B. van der Putten, A.K. Tripathi, G.H. Gelinck, J. Genoe, and W. Dehaene. Organic RFID transponder chip with data rate compatible with electronic product coding. *Organic Electronics*, 11 (7): 1176–1179, Jul 2010. doi: 10.1016/j.orgel.2010.04.013.

[16] Thinfilm products. http://www.thinfilm.no/. Accessed: 2020-01-10.

[17] Angel Ramos, David Girbau, Antonio Lazaro, and Ramon Villarino. Permittivity sensor using chipless time-coded UWB RFID. In *2014 XXXIth URSI General Assembly and Scientific Symposium (URSI GASS)*. Institute of Electrical and Electronics Engineers (IEEE), Aug 2014. doi: 10.1109/ursigass.2014.6929403.

[18] Shulabh Gupta, Babak Nikfal, and Christophe Caloz. Rfid system based on pulse-position modulation using group delay engineered microwave c-sections. In *Proceedings of Asia-Pacifc Microwave Conference*, 2010.

[19] Raji Sasidharan Nair, Etienne Perret, Smail Tedjini, and Thierry Baron. A group-delay-based chipless RFID humidity tag sensor using silicon nanowires. *IEEE Antennas and Wireless Propagation Letters*, 12: 729–732, 2013. doi: 10.1109/lawp.2013.2270929.

[20] Raji Sasidharan Nair and Etienne Perret. Folded multilayer c-sections with large group delay swing for passive chipless RFID applications. *IEEE Transactions on Microwave Theory and Techniques*, 64 (12): 4298–4311, Dec 2016. doi: 10.1109/tmtt.2016.2613049.

[21] Jordi Naqui and Ferran Martin. Application of broadside-coupled split ring resonator (BC-SRR) loaded transmission lines to the design of rotary encoders for space applications. In *2016 IEEE MTT-S International Microwave Symposium (IMS)*. IEEE, May 2016. doi: 10.1109/mwsym.2016.7540017.

[22] Javier Mata-Contreras, Cristian Herrojo, and Ferran Martin. Application of split ring resonator (SRR) loaded transmission lines to the design of angular displacement and velocity sensors for space applications. *IEEE Transactions*

on Microwave Theory and Techniques, 65 (11): 4450–4460, Nov 2017. doi: 10.1109/tmtt.2017.2693981.

[23] Cristian Herrojo, Jordi Naqui, Ferran Paredes, and Ferran Martn. Spectral signature barcodes based on s-shaped split ring resonators (s-SRRs). *ÉPJ Applied Metamaterials*, 3: 1, 2016. doi: 10.1051/epjam/2016002.

[24] Cristian Herrojo, Javier Mata-Contreras, Ferran Paredes, and Ferran Martin. Microwave encoders for chipless RFID and angular velocity sensors based on s-shaped split ring resonators. *IEEE Sensors Journal*, 17 (15): 4805–4813, Aug 2017. doi: 10.1109/jsen.2017.2715982.

[25] Cristian Herrojo, Javier Mata-Contreras, Ferran Paredes, and Ferran Martn. High data density and capacity in chipless radiofrequency identification (chipless-RFID) tags based on double-chains of s-shaped split ring resonators (s-SRRs). *ÉPJ Applied Metamaterials*, 4: 8, 2017. doi: 10.1051/epjam/2017008.

[26] C. Herrojo, J. Mata-Contreras, F. Paredes, A. Núñez, E. Ramon, and F. Martn. Near-field chipless-RFID tags with sequential bit reading implemented in plastic substrates. *Journal of Magnetism and Magnetic Materials*, 459: 322–327, Aug 2018. doi: 10.1016/j.jmmm.2017.10.005.

[27] Cristian Herrojo, Miquel Moras, Ferran Paredes, Alba Núñez, Eloi Ramon, Javier Mata-Contreras, and Ferran Martn. Very low-cost 80-bit chipless-RFID tags inkjet printed on ordinary paper. *Technologies*, 6 (2): 52, May 2018. doi: 10.3390/technologies6020052.

[28] Cristian Herrojo, Javier Mata-Contreras, Ferran Paredes, Alba Nunez, Eloi Ramon, and Ferran Martin. Near-field chipless-RFID system with erasable/programmable 40-bit tags inkjet printed on paper substrates. *IEEE Microwave and Wireless Components Letters*, 28 (3): 272–274, Mar 2018. doi: 10.1109/lmwc.2018.2802718.

[29] Cristian Herrojo, Ferran Paredes, and Ferran Martin. A new paradigm in chipless-RFID: all-dielectric permittivity contrast tags. In *2019 IEEE International Conference on RFID Technology and Applications (RFID-TA)*. IEEE, Sep 2019. doi: 10.1109/rfid-ta.2019.8892121.

[30] I. Jalaly and I. Robertson. RF barcodes using multiple frequency bands. In *IEEE MTT-S International Microwave Symposium Digest, 2005*. Institute of Electrical and Electronics Engineers (IEEE), 2005. doi: 10.1109/mwsym.2005.1516542.

[31] Arnaud Vena, Etienne Perret, and Smail Tedjini. A fully printable chipless RFID tag with detuning correction technique. *IEEE Microwave and Wireless Components Letters*, 22 (4): 209–211, Apr 2012. doi: 10.1109/lmwc.2012.2188785.

[32] M. Sumi, A. Pradeep, B. Paul, and S. Mridula. High security chipless RFID tags using frequency shift coding technique. *Radioengineering*, 26 (3): 765–771, Sep 2017. doi: 10.13164/re.2017.0765.

[33] C. M. Nijas, U. Deepak, P. V. Vinesh, R. Sujith, S. Mridula, K. Vasudevan, and P. Mohanan. Low-cost multiple-bit encoded chipless RFID tag using stepped impedance resonator. *IEEE Transactions on Antennas and Propagation*, 62 (9): 4762–4770, Sep 2014. doi: 10.1109/tap.2014.2330586.

[34] Arnaud Vena, Etienne Perret, and Smail Tedjini. Chipless RFID tag using hybrid coding technique. *IEEE Transactions on Microwave Theory and Techniques*, 59 (12): 3356–3364, Dec 2011. doi: 10.1109/tmtt.2011.2171001.

[35] Cristian Herrojo, Ferran Paredes, Javier Mata-Contreras, Simone Zuffanelli, and Ferran Martin. Multistate multiresonator spectral signature barcodes implemented by means of s-shaped split ring resonators (s-SRRs). *IEEE Transactions on Microwave Theory and Techniques*, 65 (7): 2341–2352, Jul 2017. doi: 10.1109/tmtt.2017.2672547.

[36] Guo Chun Wan, Quan Gu, Xin Rui Zhang, and Mei Song Tong. Frequency-coded chipless RFID tag based on hybrid coding technique. In *2017 IEEE International Symposium on Antennas and Propagation & USNC/URSI National Radio Science Meeting*. IEEE, Jul 2017. doi: 10.1109/apusncursinrsm.2017.8073302.

[37] Olivier Rance, Romain Siragusa, Pierre Lemaitre-Auger, and Etienne Perret. Toward RCS magnitude level coding for chipless RFID. *IEEE Transactions on Microwave Theory and Techniques*, 64 (7): 2315–2325, Jul 2016. doi: 10.1109/tmtt.2016.2562625.

[38] Yi zhan Ni, Xiao dong Huang, Yun peng Lv, and Chong hu Cheng. Hybrid coding chipless tag based on impedance loading. *IET Microwaves, Antennas & Propagation*, 11 (10): 1325–1331, Aug 2017. doi: 10.1049/iet-map.2016.0759.

[39] Bob Violino. Firewall protection for paper documents. http://www.rfidjournal.com/articles/view?790, Feb 2004. Accessed: 2020-01-10.

[40] K Jones. Invisible rfid ink safe for cattle and people, company says. https://www.informationweek.com/invisible-rfid-ink-safe-for-cattle-and-people-company-says/d/d-id/1050602, Oct 2007. Accessed: 2020-01-10.

[41] J. McVay, A. Hoorfar, and N. Engheta. Space-filling curve RFID tags. In *2006 IEEE Radio and Wireless Symposium*. Institute of Electrical and Electronics Engineers (IEEE), 2006. doi: 10.1109/rws.2006.1615129.

[42] Ali Alhaj Abbas, Mohammed El-Absi, Ashraf Abuelhaijay, Klaus Solbach, and Thomas Kaiser. THz passive RFID tag based on dielectric resonator linear

array. In *2019 Second International Workshop on Mobile Terahertz Systems (IWMTS)*. IEEE, Jjul 2019. doi: 10.1109/iwmts.2019.8823734.

[43]   Introducing digital mouseÂ®. https://mysensalab.com/products/digital-mouse/. Accessed: 2020-01-10.

[44]   Alejandro Jimenez-Saez, Peter Schumacher, Kevin Hauser, Martin Schusler, Joachim R. Binder, and Rolf Jakoby. Chipless wireless high temperature sensing based on a multilayer dielectric resonator. In *2019 IEEE SENSORS*. IEEE, Oct 2019. doi: 10.1109/sensors43011.2019.8956863.

[45]   Emran Md Amin and Nemai Karmakar. Partial discharge monitoring of high voltage equipment using chipless rfid sensor. In *Asia-Pacific Microwave Conference 2011*, 2011.

[46]   Yi Feng, Li Xie, Qiang Chen, and Li-Rong Zheng. Low-cost printed chipless RFID humidity sensor tag for intelligent packaging. *IEEE Sensors Journal*, 15 (6): 3201–3208, Jun 2015. doi: 10.1109/jsen.2014.2385154.

[47]   A. Guillet, A. Vena, E. Perret, and S. Tedjini. Design of a chipless RFID sensor for water level detection. In *2012 15 International Symposium on Antenna Technology and Applied Electromagnetics*. Institute of Electrical and Electronics Engineers (IEEE), Jun 2012. doi: 10.1109/antem.2012.6262372.

[48]   I. Jalaly and I.D. Robertson. Capacitively-tuned split microstrip resonators for RFID barcodes. In *2005 European Microwave Conference*. Institute of Electrical and Electronics Engineers (IEEE), 2005. doi: 10.1109/eumc.2005.1610138.

[49]   T. Singh, S. Tedjini, E. Perret, and A. Vena. A frequency signature based method for the RF identification of letters. In *2011 IEEE International Conference on RFID*. Institute of Electrical and Electronics Engineers (IEEE), Apr 2011. doi: 10.1109/rfid.2011.5764628.

[50]   Arnaud Vena, Etienne Perret, and Smail Tedjini. Design of compact and auto-compensated single-layer chipless RFID tag. *IEEE Transactions on Microwave Theory and Techniques*, 60 (9): 2913–2924, Sep 2012. doi: 10.1109/tmtt.2012.2203927.

[51]   Milan Polivka and Jan Machac. Novel size-reduced unit cells for uniplanar chipless RFID tags. In *2013 Asia-Pacific Microwave Conference Proceedings (APMC)*. Institute of Electrical and Electronics Engineers (IEEE), Nov 2013. doi: 10.1109/apmc.2013.6694970.

[52]   Milan Polivka, Milan Svanda, and Jan Machac. Chipless RFID tag with an improved RCS response. In *2014 44th European Microwave Conference*. Institute of Electrical and Electronics Engineers (IEEE), Oct 2014. doi: 10.1109/eumc.2014.6986548.

[53]   Reza Rezaiesarlak and Majid Manteghi. Complex-natural-resonance-based design of chipless RFID tag for high-density data. *IEEE Transactions on Antennas and Propagation*, 62 (2): 898–904, Feb 2014. doi: 10.1109/tap.2013.2290998.

[54]   R. Rezaiesarlak and M. Manteghi. Short-time matrix pencil method for chipless RFID detection applications. *IEEE Transactions on Antennas and Propagation*, 61 (5): 2801–2806, May 2013. doi: 10.1109/tap.2013.2238497.

[55]   R. Rezaiesarlak and M. Manteghi. On the application of short-time matrix pencil method for wideband scattering from resonant structures. *IEEE Transactions on Antennas and Propagation*, 63 (1): 328–335, Jan 2015. doi: 10.1109/tap.2014.2365823.

[56]   Reza Rezaiesarlak and Majid Manteghi. Design of chipless RFID tags based on characteristic mode theory (CMT). *IEEE Transactions on Antennas and Propagation*, 63 (2): 711–718, Feb 2015. doi: 10.1109/tap.2014.2382640.

[57]   Filippo Costa, Simone Genovesi, and Agostino Monorchio. Normalization-free chipless RFIDs by using dual-polarized interrogation. *IEEE Transactions on Microwave Theory and Techniques*, 64 (1): 310–318, Jan 2016. doi: 10.1109/tmtt.2015.2504529.

[58]   Filippo Costa, Simone Genovesi, and Agostino Monorchio. A chipless RFID based on multiresonant high-impedance surfaces. *IEEE Transactions on Microwave Theory and Techniques*, 61 (1): 146–153, Jan 2013. doi: 10.1109/tmtt.2012.2227777.

[59]   Khaled Issa, Yazeed A. Alshoudokhi, Muhammad A. Ashraf, Mohammed R. AlShareef, Hatim M. Behairy, S. Alshebeili, and H. Fathallah. A high-density l-shaped backscattering chipless tag for RFID bistatic systems. *International Journal of Antennas and Propagation*, 2018: 1–10, Aug 2018. doi: 10.1155/2018/1542520.

[60]   Caixia Feng, Wenmei Zhang, Li Li, Liping Han, Xinwei Chen, and Runbo Ma. Angle-based chipless RFID tag with high capacity and insensitivity to polarization. *IEEE Transactions on Antennas and Propagation*, 63 (4): 1789–1797, Apr 2015. doi: 10.1109/tap.2015.2393851.

[61]   S. Gupta, R.C. Roberts, Li Jun Jiang, and Gui Jun Li. Log-periodic dipole array antenna as chipless RFID tag. *Electronics Letters*, 50 (5): 339–341, Feb 2014. doi: 10.1049/el.2013.4253.

[62]   Md. Aminul Islam and Nemai Chandra Karmakar. A novel compact printable dual-polarized chipless RFID system. *IEEE Transactions on Microwave Theory and Techniques*, 60 (7): 2142–2151, Jul 2012. doi: 10.1109/tmtt.2012.2195021.

[63]   Arnaud Vena, Etienne Perret, and Smail Tedjni. A depolarizing chipless RFID tag for robust detection and its FCC compliant UWB reading system. *IEEE Transactions on Microwave Theory and Techniques*, 61 (8): 2982–2994, Aug 2013. doi: 10.1109/tmtt.2013.2267748.

[64]   Arnaud Vena, Etienne Perret, and Smail Tedjini. High-capacity chipless RFID tag insensitive to the polarization. *IEEE Transactions on Antennas and Propagation*, 60 (10): 4509–4515, Oct 2012. doi: 10.1109/tap.2012.2207347.

[65]   Wazie M. Abdulkawi and Abdel-Fattah A. Sheta. K-state resonators for high-coding-capacity chipless RFID applications. *IEEE Access*, 7: 185868–185878, 2019. doi: 10.1109/access.2019.2961565.

[66]   Filippo Costa, Simone Genovesi, Agostino Monorchio, and Giuliano Manara. A robust differential-amplitude codification for chipless RFID. *IEEE Microwave and Wireless Components Letters*, 25 (12): 832–834, Dec 2015. doi: 10.1109/lmwc.2015.2496791.

[67]   Simone Genovesi, Filippo Costa, Agostino Monorchio, and Giuliano Manara. Chipless RFID tag exploiting multifrequency delta-phase quantization encoding. *IEEE Antennas and Wireless Propagation Letters*, 15: 738–741, 2016. doi: 10.1109/lawp.2015.2471101.

[68]   Simone Genovesi, Filippo Costa, Michele Borgese, Alessio Francesco Dicandia, Giuliano Manara, Smail Tedjini, and Etienne Perret. Enhanced chipless RFID tags for sensors design. In *2016 IEEE International Symposium on Antennas and Propagation (APSURSI)*. Institute of Electrical and Electronics Engineers (IEEE), Jun 2016. doi: 10.1109/aps.2016.7696345.

[69]   Li Wang, Chuandeng Hu, Xiaoxiao Wu, Zengzilu Xia, and Weijia Wen. Multi-band metamaterial absorber with arbitrary polarization and wide-incident angle. *Applied Physics A*, 123 (10), Sep 2017. doi: 10.1007/s00339-017-1255-0.

[70]   Nimra Tariq, Muhammad Ali Riaz, Humayun Shahid, Muhammad Jamil Khan, Mansoor Shaukat Khan, Yasar Amin, Jonathan Loo, and Hannu Tenhunen. Orientation independent chipless RFID tag using novel trefoil resonators. *IEEE Access*, 7: 122398–122407, 2019. doi: 10.1109/access.2019.2937131.

[71]   S. Preradovic, I. Balbin, N.C. Karmakar, and G.F. Swiegers. Multiresonator-based chipless RFID system for low-cost item tracking. *IEEE Transactions on Microwave Theory and Techniques*, 57 (5): 1411–1419, May 2009. doi: 10.1109/tmtt.2009.2017323.

[72]   Stevan Preradovic and Nemai Chandra Karmakar. *Multiresonator-Based Chipless RFID*. Springer New York, 2012. doi: 10.1007/978-1-4614-2095-8.

[73] Vijay Sharma and Mohammad Hashmi. Simple chipless RFID tag configurations. In *2018 IEEE Asia-Pacific Conference on Antennas and Propagation (APCAP)*. IEEE, Aug 2018. doi: 10.1109/apcap.2018.8538137.

[74] Jordi Naqui, Gerard Zamora, Ferran Paredes, Jordi Bonache, and Ferran Martin. Metamaterial transmission lines for wireless communications, sensing and RFID. In *Proceedings of 2014 Mediterranean Microwave Symposium (MMS2014)*. IEEE, Dec 2014. doi: 10.1109/mms.2014.7088938.

[75] Dong Huu Nguyen, Mohammad Zomorrodi, and Nemai Chandra Karmakar. Spatial-based chipless RFID system. *IEEE Journal of Radio Frequency Identification*, 3 (1): 46–55, Mar 2019. doi: 10.1109/jrfid.2018.2887162.

[76] Jaroslav Havlicek, Milan Polivka, Milan Svanda, and Jan Machac. Capacitively loaded dipoles for chipless RFID transponder. In *2016 26th International Conference Radioelektronika (RADIOELEKTRONIKA)*. Institute of Electrical and Electronics Engineers (IEEE), Apr 2016. doi: 10.1109/radioelek.2016.7477349.

[77] J. Havlicek, M. Svanda, J. Machac, and M. Polivka. Improvement of reading performance of frequency-domain chipless RFID transponders. *Radioengineering*, 25 (2): 219–229, Apr 2016. doi: 10.13164/re.2016.0219.

[78] Jan Machac, Milan Polivka, Milan Svanda, and Jaroslav Havlicek. Reducing mutual coupling in chipless rfid tags composed of u-folded dipole scatterers. *Microwave and Optical Technology Letters*, 58 (11): 2723–2725, Aug 2016. doi: 10.1002/mop.30138.

[79] Milan Svanda, Jaroslav Havlicek, Jan Machac, and Milan Polivka. Polarisation independent chipless RFID tag based on circular arrangement of dual-spiral capacitively-loaded dipoles with robust RCS response. *IET Microwaves, Antennas & Propagation*, 12 (14): 2167–2171, Nov 2018. doi: 10.1049/iet-map.2018.5434.

[80] Jaroslav Havlicek, Milan Svanda, Milan Polivka, Jan Machac, and Jan Kracek. Chipless RFID tag based on electrically small spiral capacitively loaded dipole. *IEEE Antennas and Wireless Propagation Letters*, 16: 3051–3054, 2017. doi: 10.1109/lawp.2017.2760059.

[81] S.R. Best and J.D. Morrow. On the significance of current vector alignment in establishing the resonant frequency of small space-filling wire antennas. *IEEE Antennas and Wireless Propagation Letters*, 2 (1): 201–204, 2003. doi: 10.1109/lawp.2003.819686.

[82] Milan Polivka, Jaroslav Havlicek, Milan Svanda, and Jan Machac. Improvement in robustness and recognizability of RCS response of u-shaped strip-based chipless RFID tags. *IEEE Antennas and Wireless Propagation Letters*, 15: 2000–2003, 2016. doi: 10.1109/lawp.2016.2549638.

[83]   Milan Polivka, Jaroslav Havlicek, Milan Svanda, and Jan Machac. Improvement of RCS response of u-shaped strip-based chipless RFID tags. In *2015 European Microwave Conference (EuMC)*. IEEE, Sep 2015. doi: 10.1109/eumc.2015.7345711.

[84]   A. Boussada, J. Machac, M. Svanda, J. Havlicek, and M. Polivka. Erroneous reading of information in chipless RFID tags. In *2017 Progress In Electromagnetics Research Symposium - Spring (PIERS)*. IEEE, May 2017. doi: 10.1109/piers.2017.8262326.

[85]   Jan Machac, Amine Boussada, Milan Svanda, Jaroslav Havlicek, and Milan Polivka. Influence of mutual coupling on stability of RCS response in chipless RFID. *Technologies*, 6 (3): 67, Jul 2018. doi: 10.3390/technologies6030067.

[86]   Model drh20 - double ridge waveguide horn. rfspin s.r.o. https://www.rfspin.cz/en/antennas/measurement-antennas/drh20.   Accessed: 2020-01-10.

[87]   Model qrh20 - quad ridge waveguide horn. rfspin s. r. o. http://www.rfspin.cz/en/antennas/dual-polarized-antennas/. Accessed: 2020-01-10.

[88]   Milan Polivka and Jan Machac. Improvement of backscatter properties of c-shaped dipole scatterer for chipless rfid. In *2014 Asia-Pacific Microwave Conference Proceedings*, 2014.

[89]   Jan Machac and Milan Polivka. Influence of mutual coupling on performance of small scatterers for chipless RFID tags. In *2014 24th International Conference Radioelektronika*. IEEE, Apr 2014. doi: 10.1109/radioelek.2014.6828412.

[90]   Lukas Jelinek and Jan Machac. A polarizability measurement method for electrically small particles. *IEEE Antennas and Wireless Propagation Letters*, 13: 1051–1053, 2014. doi: 10.1109/lawp.2014.2327152.

[91]   John David Jackson. *Classical Electrodynamics*. John Wiley & Sons Inc, 1998. ISBN 047130932X.

[92]   Jean Richard Huynen. *Phenomenological Theory of Radar Targets*. New York Academic Press, 1978.

[93]   Milan Svanda, Milan Polivka, Jaroslav Havlicek, Jan Machac, and Douglas H. Werner. Platform tolerant, high encoding capacity dipole array-plate chipless RFID tags. *IEEE Access*, 7: 138707–138720, 2019. doi: 10.1109/access.2019.2935258.

[94]   Constantine A. Balanis. *Antenna Theory*. Wiley John & Sons, 2016. ISBN 1118642066.

[95] Jaroslav Havlicek, Cristian Herrojo, Ferran Paredes, Javier Mata-Contreras, and Ferran Martin. Enhancing the per-unit-length data density in near-field chipless-RFID systems with sequential bit reading. *IEEE Antennas and Wireless Propagation Letters*, 18 (1): 89–92, Jan 2019. doi: 10.1109/lawp.2018.2881356.

[96] Jaroslav Havlicek, Cristian Herrojo, Javier Mata-Contreras, Ferran Paredes, and Ferran Martin. Stub-loaded microstrip line loaded with half-wavelength resonators and application to near-field chipless-RFID. In *2018 IEEE MTT-S Latin America Microwave Conference (LAMC 2018)*. IEEE, Dec 2018. doi: 10.1109/lamc.2018.8699074.

[97] Milan Svanda, Milan Polivka, Jaroslav Havlicek, and Jan Machac. Chipless RFID tag with an improved magnitude and robustness of RCS response. *Microwave and Optical Technology Letters*, 59 (2): 488–492, Dec 2016. doi: 10.1002/mop.30321.

[98] M. Polivka, M. Svanda, J. Havlicek, and J. Machac. Detuned dipole array backed by rectangular plate applied as chipless RFID tag. In *2017 Progress In Electromagnetics Research Symposium - Spring (PIERS)*. IEEE, May 2017. doi: 10.1109/piers.2017.8262328.

[99] Hermann A. Haus. *Waves and Fields in Optoelectronics (Prentice-Hall series in solid state physical electronics)*. Prentice Hall, 1983. ISBN 978-0139460531.

[100] Kalyan K. Karnati, Yazid Yusuf, Siamak Ebadi, and Xun Gong. Theoretical analysis on reflection properties of reflectarray unit cells using quality factors. *IEEE Transactions on Antennas and Propagation*, 61 (1): 201–210, Jan 2013. doi: 10.1109/tap.2012.2214753.

[101] J.C.-E. Sten, A. Hujanen, and P.K. Koivisto. Quality factor of an electrically small antenna radiating close to a conducting plane. *IEEE Transactions on Antennas and Propagation*, 49 (5): 829–837, May 2001. doi: 10.1109/8.929637.

[102] Best. Improving the performance properties of a dipole element closely spaced to a PEC ground plane. *IEEE Antennas and Wireless Propagation Letters*, 3: 359–363, 2004. doi: 10.1109/lawp.2004.840722.

[103] Hsieh-Chi Chang, Yong Heui Cho, and Do-Hoon Kwon. Radiation q bounds for small electric dipoles over a conducting ground plane. *IEEE Transactions on Antennas and Propagation*, 62 (4): 2031–2040, Apr 2014. doi: 10.1109/tap.2013.2297162.

[104] Pavel Hazdra, Miloslav Capek, Jan Eichler, and Milos Mazanek. The radiation q-factor of a horizontal lambda/2 dipole above ground plane. *IEEE Antennas*

and Wireless Propagation Letters, 13: 1073–1075, 2014. doi: 10.1109/lawp.2014.2329421.

[105] John Volakis. *Antenna Engineering Handbook*. McGraw-Hill Education Ltd, 2018. ISBN 1259644693.

[106] N. Engheta. Thin absorbing screens using metamaterial surfaces. *IEEE Antennas and Propagation Society International Symposium (IEEE Cat. No.02CH37313)*, 2002, pp. 392-395 vol.2. doi: 10.1109/APS.2002.1016106